

NAVAL POSTGRADUATE SCHOOL

MONTEREY, CALIFORNIA

THESIS

EXPERIMENTAL AND COMPUTATIONAL ANALYSIS OF ADVANCED CASING TREATMENTS IN A TRANSONIC COMPRESSOR

by

Matthew B. Jones

June 2022

Thesis Advisor: Anthony J. Gannon
Co-Advisor: Walter C. Smith

Approved for public release. Distribution is unlimited.

THIS PAGE INTENTIONALLY LEFT BLANK

REPORT DOCUMENTATION PAGE			*Form Approved OMB No. 0704-0188*

Public reporting burden for this collection of information is estimated to average 1 hour per response, including the time for reviewing instruction, searching existing data sources, gathering and maintaining the data needed, and completing and reviewing the collection of information. Send comments regarding this burden estimate or any other aspect of this collection of information, including suggestions for reducing this burden, to Washington headquarters Services, Directorate for Information Operations and Reports, 1215 Jefferson Davis Highway, Suite 1204, Arlington, VA 22202-4302, and to the Office of Management and Budget, Paperwork Reduction Project (0704-0188) Washington, DC, 20503.

1. AGENCY USE ONLY *(Leave blank)*	**2. REPORT DATE** June 2022	**3. REPORT TYPE AND DATES COVERED** Master's thesis

4. TITLE AND SUBTITLE EXPERIMENTAL AND COMPUTATIONAL ANALYSIS OF ADVANCED CASING TREATMENTS IN A TRANSONIC COMPRESSOR	**5. FUNDING NUMBERS** RMKW1
6. AUTHOR(S) Matthew B. Jones	
7. PERFORMING ORGANIZATION NAME(S) AND ADDRESS(ES) Naval Postgraduate School Monterey, CA 93943-5000	**8. PERFORMING ORGANIZATION REPORT NUMBER**
9. SPONSORING / MONITORING AGENCY NAME(S) AND ADDRESS(ES) Office of Naval Research, Arlington, VA, 22217	**10. SPONSORING / MONITORING AGENCY REPORT NUMBER**

11. SUPPLEMENTARY NOTES The views expressed in this thesis are those of the author and do not reflect the official policy or position of the Department of Defense or the U.S. Government.

12a. DISTRIBUTION / AVAILABILITY STATEMENT Approved for public release. Distribution is unlimited.	**12b. DISTRIBUTION CODE** A

13. ABSTRACT (maximum 200 words)

Turbo-fan engines seek to achieve the highest compression ratios possible with the minimum number of parts by driving compressor stages to the extremes of their operating limits, which can risk compressor stall. This study expands on previous work by combining experimental and computational methods to evaluate the effectiveness of advanced transonic compressor casing treatments at increasing stall margin while minimizing losses. The NPS Turbopropulsion Lab Transonic Compressor Rig was used to characterize the performance of an advanced transonic compressor in the stage and stage-and-a-half configurations; additionally, inlet guide vanes were installed and evaluated. After characterization of the base performance, s-shaped axial endwall grooves were added to improve stall margin of the compressor stage. Experimental results proved the casing treatments were successful only in the subsonic regime. Stall margin increases of at least 286% were seen in low speed tests with 117% observed in high speed operation. Computational analysis simulated advanced casing treatments and effects of inlet whirl and was correlated to experimental data to shed light on the recirculation mechanisms active in casing treatments. The simulations provided insight for further development of novel self-recirculating endwall treatments and associated technologies.

14. SUBJECT TERMS compressor, casing, stall margin, CFD, CFX	**15. NUMBER OF PAGES** 151
	16. PRICE CODE

17. SECURITY CLASSIFICATION OF REPORT	**18. SECURITY CLASSIFICATION OF THIS PAGE**	**19. SECURITY CLASSIFICATION OF ABSTRACT**	**20. LIMITATION OF ABSTRACT**
Unclassified	Unclassified	Unclassified	UU

NSN 7540-01-280-5500

Standard Form 298 (Rev. 2-89)
Prescribed by ANSI Std. 239-18

THIS PAGE INTENTIONALLY LEFT BLANK

Approved for public release. Distribution is unlimited.

EXPERIMENTAL AND COMPUTATIONAL ANALYSIS OF ADVANCED CASING TREATMENTS IN A TRANSONIC COMPRESSOR

Matthew B. Jones
Ensign, United States Navy
BS, United States Naval Academy, 2021

Submitted in partial fulfillment of the
requirements for the degree of

MASTER OF SCIENCE IN AEROSPACE ENGINEERING

from the

NAVAL POSTGRADUATE SCHOOL
June 2022

Approved by: Anthony J. Gannon
Advisor

Walter C. Smith
Co-Advisor

Garth V. Hobson
Chair, Department of Mechanical and Aerospace Engineering

THIS PAGE INTENTIONALLY LEFT BLANK

ABSTRACT

Turbo-fan engines seek to achieve the highest compression ratios possible with the minimum number of parts by driving compressor stages to the extremes of their operating limits, which can risk compressor stall. This study expands on previous work by combining experimental and computational methods to evaluate the effectiveness of advanced transonic compressor casing treatments at increasing stall margin while minimizing losses. The NPS Turbopropulsion Lab Transonic Compressor Rig was used to characterize the performance of an advanced transonic compressor in the stage and stage-and-a-half configurations; additionally, inlet guide vanes were installed and evaluated. After characterization of the base performance, s-shaped axial endwall grooves were added to improve stall margin of the compressor stage. Experimental results proved the casing treatments were successful only in the subsonic regime. Stall margin increases of at least 286% were seen in low speed tests with 117% observed in high speed operation. Computational analysis simulated advanced casing treatments and effects of inlet whirl and was correlated to experimental data to shed light on the recirculation mechanisms active in casing treatments. The simulations provided insight for further development of novel self-recirculating endwall treatments and associated technologies.

THIS PAGE INTENTIONALLY LEFT BLANK

Table of Contents

1 Introduction **1**
1.1 Motivation 1
1.2 Literature Review 1
1.3 Current Study. 11

2 Experimental Facilities and Setup **13**
2.1 Transonic Compressor 13
2.2 Inlet Guide Vanes 14
2.3 Test Conditions 19
2.4 Procedures 22

3 Computational Setup **23**
3.1 Geometry 23
3.2 Modeling 29

4 Mesh Sensitivity Study **35**
4.1 Objectives 35
4.2 Approach 35
4.3 Results 37

5 Results **45**
5.1 Experimental 45
5.2 Computational 59
5.3 Comparison 93

6 Conclusions and Recommendations **95**

Appendix A Inlet Guide Vane Jigs **97**

Appendix B Mesh Reports **103**
B.1 S-Shaped Axial Grooves 103
B.2 Internal Passages 110
B.3 Refined Standard Passage 116

Appendix C CFX on NPS Hamming HPC **125**

List of References **129**

Initial Distribution List **131**

List of Figures

Figure 1.1 Qualitative demonstration of flow recirculation in a transonic axial compressor. Source: Hembera et al. [5]. 3

Figure 1.2 Use of sliding layers in CFD analysis of casing treatments. Source: Zhu et al. [6]. 4

Figure 1.3 Schematic of self-recirculating bridge casing treatment. Source: Hathaway [2]. 5

Figure 1.4 CSIR self-recirculating casing treatment design. Source: Kumar et al. [8]. 6

Figure 1.5 NPSMF Blisk before installation in the TCR. Source: McNab [3]. 6

Figure 1.6 Meshing priorities. Source: Meinster [11]. 7

Figure 1.7 The smooth 3D printed endwall as viewed from the inlet. Source: DeSousa [12]. 8

Figure 1.8 Overview of casing treatments for this study. Source: Green [1]. . 10

Figure 2.1 A section view of the TCR in the IRS configuration. 13

Figure 2.2 Reduction of compressor blade angle-of-attack due to inlet guide vane whirl. 15

Figure 2.3 Using a Vernier depth micrometer to measure depth of trailing edge to a thousandth of an inch. 16

Figure 2.4 The horizontal tangency line and the probe offset used to calculate angular deviation. 17

Figure 2.5 The plane (in blue) is perpendicular to the blade end and allows the distance between the axis of rotation and the probe contact point. 17

Figure 2.6 The angular deviation measured in the IGV rig. 18

Figure 2.7 Comparison of the error found with the three-bladed (left) and complete IGV jigs (right). 19

Figure 2.8 Rotor-stator speed triangle interactions. 20

Figure 3.1 The final s-shaped axial groove casing treatment mounted to the single blade gas passage. 23

Figure 3.2 Cross-sections of the sliding layers used for the axial grooves and recirculating casing treatments. 25

Figure 3.3 The full s-shaped axial groove casing treatment domain. 26

Figure 3.4 The slicing method used to make periodic boundaries. 27

Figure 3.5 The final s-shaped axial groove casing treatment domain demonstrating the periodic cuts. 27

Figure 3.6 The final internal passage casing treatment domain demonstrating the periodic cuts. 28

Figure 3.7 The final internal passage casing treatment mounted to the single blade gas passage. The aft cut in the gas passage is visible. 28

Figure 3.8 The final mesh for the s-shaped axial groove geometry. 29

Figure 3.9 Inlet boundary condition demonstrating steady-step method and pseudo-steady method. 33

Figure 4.1 Efficiency maps from smooth casing mesh analysis. Adapted from Meinster [11]. 38

Figure 4.2 RMS Residuals for a speed line evaluation. 39

Figure 4.3 Mass Flow for a steady speed line evaluation. 40

Figure 4.4 Inflation controls used to resolve boundary layers. 41

Figure 4.5 Comparison of a coarse and a refined blade tip mesh. 42

Figure 4.6 Comparison of pressure transfer for a coarse and a refined blade tip mesh. 42

Figure 4.7 The final mesh for the s-shaped axial groove case. 44

Figure 4.8 The final mesh for the internal passages casing treatment. 44

Figure 5.1 The performance curves for all configurations and speed lines tested with the TCR. 46

Figure 5.2 The efficiency curves for all configurations and speed lines tested with the TCR. 46

Figure 5.3 Comparison of rotor and rotor-stator configuration performance curves for all speed lines. 47

Figure 5.4 Comparison of rotor and rotor-stator efficiency curves for all speed lines. 48

Figure 5.5 Comparison of TCR performance in the rotor, full stage, and IRS configurations. 50

Figure 5.6 Comparison of rotor-stator and IRS performance curves for all speed lines and all IGV angles. 51

Figure 5.7 Comparison of TCR performance in the rotor, full stage, and IRS configurations. 52

Figure 5.8 Comparison of rotor-stator and IRS efficiency curves for all speed lines and all IGV angles. 53

Figure 5.9 Performance of smooth endwall and s-shaped axial grooves for all IGV angles and power lines. 54

Figure 5.10 Smooth endwall and s-shaped axial grooves with IGV set IAWS. . 55

Figure 5.11 Smooth endwall and s-shaped axial grooves with IGV set at 70% scheduling. 56

Figure 5.12 Efficiency for smooth endwalls and s-shaped axial grooves for all IGV angles and power lines. 57

Figure 5.13 Mass flow error in the pseudo-steady simulation. 59

Figure 5.14 Velocity streamlines of a simulation in a deep stall at 90% power in the IR configuration with s-groove casing treatment. 60

Figure 5.15 Comparison of steady and pseudo-steady data at 90% speed. . . . 61

Figure 5.16 90% CFD power line validation. 61

Figure 5.17 Raw CFX efficiency curves for smooth casing treatment model. . 63

Figure 5.18 Truncated CFX efficiency curves for smooth casing treatment model. 63

Figure 5.19 Numerical S-Groove performance curves without inlet whirl. . . 65

Figure 5.20 Numerical S-Groove efficiency curves without inlet whirl. 66

Figure 5.21 Axial velocity in the compressor near peak efficiency. 66

Figure 5.22 Blade-to-blade view displaying Mach number at 95% blade chord for the 70% power setting. 67

Figure 5.23 Recirculation development in the compressor at 70% power with no inlet whirl. 68

Figure 5.24 Recirculation development in the compressor at 70% power with no inlet whirl viewed from the LE. 69

Figure 5.25 Shock visualization in the compressor at 90% speed with no inlet whirl. 70

Figure 5.26 Recirculation development in the compressor with s-groove treatment at 90% power with no inlet whirl. 71

Figure 5.27 Recirculation development in the compressor at 90% power with no inlet whirl viewed from the LE. 72

Figure 5.28 Numerical S-Groove performance curves with inlet whirl. 74

Figure 5.29 Unique behavior observed with the compressor at 90% speed and the IGV set for 60% speed. 74

Figure 5.30 Numerical S-Groove efficiency curves with inlet whirl. 75

Figure 5.31 Blade-to-blade view displaying Mach number at 95% blade chord for the 70% power setting after inlet whirl has been added. 76

Figure 5.32 Recirculation development in the compressor with s-groove treatment at 70% power and 70% IGV schedule. 77

Figure 5.33 Recirculation development in the compressor at 70% power and 70% IGV schedule viewed from the LE. 78

Figure 5.34 Blade-to-blade view displaying Mach number at 95% blade chord for the 90% power setting and 70% IGV schedule. 79

Figure 5.35 Recirculation development in the compressor with s-groove treatment at 90% power and 70% IGV schedule. 80

Figure 5.36 Recirculation development in the compressor with s-groove treatment at 90% power and 70% IGV schedule viewed from the LE. 81

Figure 5.37 Numerical internal passage performance curves without inlet whirl. 83

Figure 5.38 Numerical internal passage efficiency curves without inlet whirl. . 84

Figure 5.39 Numerical internal passage performance curves with inlet whirl. . 85

Figure 5.40 Numerical internal passage efficiency curves with inlet whirl. . . 85

Figure 5.41 Mass flow ratio of flow through the internal passages against mass flow through the compressor. 86

Figure 5.42 Detailed view of compressor operation with internal passage recirculation. 87

Figure 5.43 Flow development for the compressor with internal recirculation passages at 90% speed with no inlet whirl. 88

Figure 5.44 Flow development detailing passage operation for the compressor at 90% speed and no inlet whirl with internal passages installed. . . 89

Figure 5.45 Flow development for the compressor with internal recirculation passages at 90% speed and 70% IGV schedule. 91

Figure 5.46 Flow development detailing passage operation for the compressor at 90% speed and 70% IGV schedule with internal passages installed. 92

Figure 5.47 Comparison of numerical performance results. 93

Figure 5.48 Comparison of numerical efficiency results. 94

Figure A.1 Definition and setting of inlet guide vane flap angle with a side view of the IGV rig model. 98

Figure A.2 The solid ring showing placement in the IGV with the endwall removed. 98

Figure A.3 The ring after the Boolean subtraction with blade cavities shown in blue. 99

Figure A.4 The IGV test sections and a completed ring. 100
Figure A.5 The prototype IGV angle jig with the jacking bolts installed. . . . 101
Figure A.6 Demonstration of the technique for automatic IGV jig generation. 101

List of Tables

Table 2.1 The IGV conditions tested in the TCR. 21

Table 4.1 Mesh features used to develop the final meshes. 36

Table 4.2 Mesh refinement of standard rotor-only gas passage. Adapted from Meinster [11]. 37

Table 4.3 Overview of meshes used for sensitivity study. 41

Table 4.4 Overview of meshes used for experimentation. 43

Table 5.1 Total pressure losses and mass flow range increase from the stator. 47

Table 5.2 Efficiency losses and stall margin decreases from the stator 49

Table 5.3 Mass flow rate [kg/s] at stall for half-stage, full-stage, and IRS IAWS configurations. 49

Table 5.4 Percent reduction in mass flow and pressure ratio with IGV IAWS. 50

Table 5.5 Comparison of efficiency, mass flow at peak efficiency [kg/s], and stall margin for the full-stage and IRS set IAWS. 52

Table 5.6 Efficiency and mass flow of TCR at 90% speed and varying IGV angles. 53

Table 5.7 Summary of stall margin change with s-shaped axial grooves installed. 54

Table 5.8 Summary of stall margin and peak pressure ratio change with s-shaped axial grooves installed with IGV set IAWS. 55

Table 5.9 Summary of stall margin and peak pressure ratio change with s-shaped axial grooves installed with IGV set at 70% scheduling. 57

Table 5.10 Summary of efficiency changes with s-shaped axial grooves installed. 58

Table 5.11 CFX test conditions for s-shaped axial grooves. 64

Table 5.12 Summary of numerical s-shaped axial grooves performance without IGV. 65

Table 5.13 Summary of numerical s-shaped axial grooves performance with IGV model. 75

Table 5.14 CFX test conditions for novel internal passages. 82

Table 5.15 Summary of numerical internal self-recirculating performance without IGVs. 83

Table 5.16 Summary of numerical internal self-recirculating performance with IGVs. 84

Table 5.17 Summary of numeric stall margin predictions 93

List of Acronyms and Abbreviations

AR Aspect Ratio

CFD Computational Fluid Dynamics

IAWS In Accordance with Schedule

IGV Inlet Guide Vane

IRS IGV-Rotor-Stator

LE Leading Edge

NPS Naval Postgraduate School

NPSMF Naval Postgraduate School Military Fan

TCR Transonic Compressor Rig

TE Trailing Edge

TPL Turbopropulsion Lab

THIS PAGE INTENTIONALLY LEFT BLANK

CHAPTER 1:
Introduction

1.1 Motivation

The Transonic Compressor Rig (TCR) is a flexible first stage axial compressor test facility at the Naval Postgraduate School Turbopropulsion Laboratory. It has been used to study the performance of various transonic compressors and seek improvements to current designs. Currently, research is focused on the improvement of stall margin for the Naval Postgraduate School Military Fan (NPSMF) through compressor casing treatments. Approaches were developed to allow the rapid prototyping of casing treatments for the NPSMF to allow designs to be manufactured more quickly and with more flexibility than traditional machining. The energy, cost, and man hours required still limits the amount of experimentation which can be carried out though. Computational Fluid Dynamics (CFD) provides a cost-effective means for quickly analyzing the performance of casing treatment designs. This has the potential to narrow the field of interest for treatment designs and focus the experimental effort into designs which are more likely to succeed. While CFD is able to test various configurations more efficiently than the TCR, experimentation is still necessary to validate the findings.

Previous work has sought to develop effective models of the NPSMF and study the stall mechanisms present in the flow. Analysis of stall mechanisms led to two primary designs for stall margin improvement in the NPSMF. Green [1] identified and designed techniques to build a more traditional S-shaped axial groove treatment and a novel self-recirculating internal passage design. The goal of this study is the development of techniques to study transonic casing treatments and test Green's designs to allow further refinement for future casing treatment designs.

1.2 Literature Review

Much experimental and computational effort has been put into improving the stall margin of axial compressors; Hathaway [2] presents a brief history of many devices created to improve compressor stall margin. As the performance and efficiency of turbines has been

pushed further, pressure ratios across the compressor have increased significantly. Equation 1.1 from McNab [3] shows the relationship between pressure ratio and stage efficiency. T_t and P_t are total temperature and pressure respectively with station ∞ representing the free stream conditions prior to entering the compressor and station 3 representing the conditions after the stage. The constant γ is the gas constant for the fluid.

$$\eta_c = \frac{T_{t,\infty}}{T_{t,3} - T_{t,\infty}} \left[\left(\frac{P_{t,3}}{P_{t,\infty}} \right)^{\frac{\gamma}{\gamma-1}} - 1 \right] \tag{1.1}$$

To get the efficiencies desired, compressors are run as close to the stall margin as possible. However, perturbations in the flow caused by maneuvering or high angle-of-attack flight during takeoffs and landings can cause rotor stall and subsequent power loss. Increasing the stall margin of existing compressors allows them to be operated at higher pressure ratios and allows for greater flexibility when maneuvering and accelerating the turbine. Recent effort has pushed the increased use of computational methods as compressor experimentation is costly and the machining processes for endwall treatments is often exceedingly complex — especially for novel prototypes.

1.2.1 External

Previous work has highlighted three feasible compressor endwall treatments for the improvement of stall margin with minimal efficiency loss: circumferential grooves or slots, axial grooves, and various forms of internal flow recirculation. The latter two devices will be the focus of this study. As an example, Chen et al. [4] demonstrated stall margin improvements of 36% - 60% with less than 2% efficiency loss using curved axial grooves in a low speed compressor which serve as the basis for the s-shaped groove designed by Green [1].

The introduction of shocks in transonic compressors reduces the efficiency of endwall treatments, but Hembera et al. [5] demonstrated flow recirculation in a simulation of axial casing treatments as the shocked passed. The same paper demonstrated a 9% stall margin improvement without optimizing the axial slot. Figure 1.1 shows the flow phenomenon reported by Hembera et al. [5]. These results were captured using an unsteady rotor-stator interface in the NUMECA solver passing information into the axial grooves via a circumferential socket (stationary slice taken from rotating compressor geometry) in the

stage geometry [5]. A similar approach was taken by Zhu et al. [6] in their computational setup of their casing treatment optimization. Two extremely thin (< 1% tip clearance) sliding layers were placed atop of the blade and the casing treatment was affixed to this layer [6]. Figure 1.2 presents their approach. A stall margin increase of 23.6% was computationally demonstrated by Zhu et al. [6] using axial and circumferential casing treatments on a NASA Rotor 67 transonic compressor.

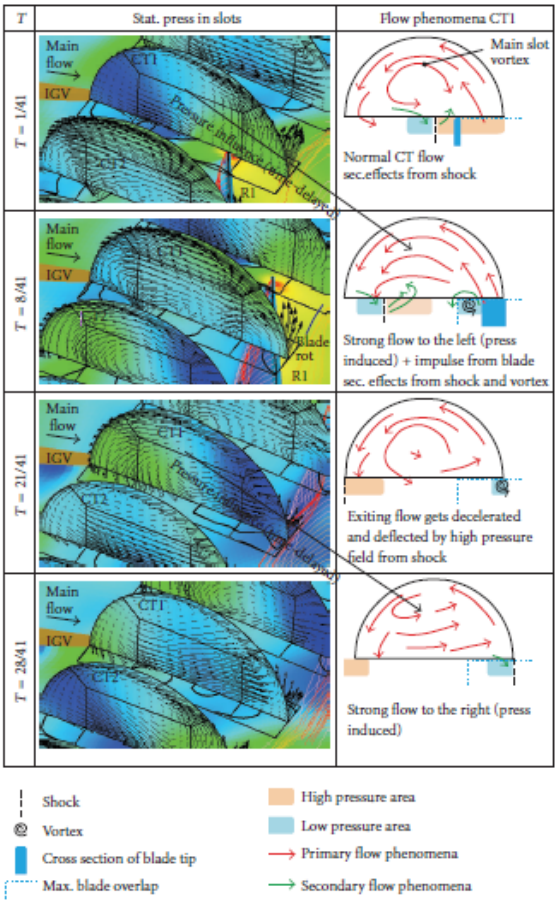


Figure 1.1. Qualitative demonstration of flow recirculation in a transonic axial compressor. Source: Hembera et al. [5].

A steady-state simulation using mixing planes was conducted and verified experimentally by Rolfes et al. [7] on a compressor stage with circumferential grooves. The tip gap in their model was resolved by approximately 17 cells per 1% clearance; it is noted this is above recommended values and greatly increased computational time required [7].

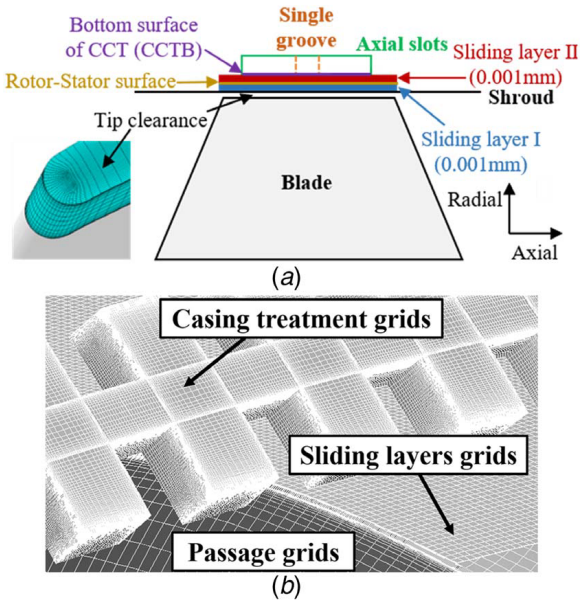


Figure 1.2. Use of sliding layers in CFD analysis of casing treatments.
Source: Zhu et al. [6].

The concepts of recirculating axial casing treatments to improve stall margin and small tip gaps to improve efficiency are nearly antithetical. Hathaway [2] discussed the various methods of improving stall margin with casing treatments with the latest idea being bleed and injection ports connected with self-recirculating passages. The most effective, but complicated solution presented, is a device which bleeds high pressure air off of later stages of the compressor and feeds it to the first stage. This method is bulky and expensive, so self-contained systems within a stage are proposed. Such systems bleed 3-5% of mass flow from the first stage and recirculate it to improve stall margin in a much smaller package than a high pressure, controlled system. Figure 1.3 shows a self-recirculating bridge design added over a stage.

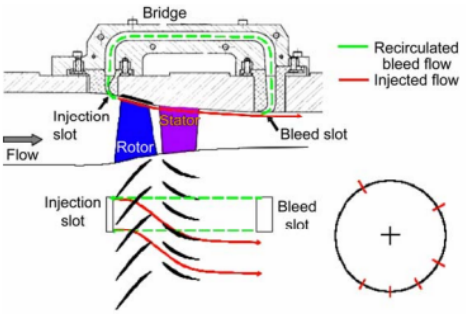


Figure 1.3. Schematic of self-recirculating bridge casing treatment. Source: Hathaway [2].

The National Aerospace Laboratories of India designed and experimented with a self-recirculating passage for transonic axial compressors. Their design features a rectangular cross-section and attempts to inject the recirculated gas as axially as possible which is depicted in Figure 1.4 [8]. A CFD analysis was done on a complete stage using ANSYS CFX. Two casing treatments are modeled and kept in a stationary domain while the compressor stage is rotating. A "general connection interface" is used with the mixing plane option selected [8]. Another numerical study on the NASA Stage 67 transonic compressor followed a similar approach. A stationary inflow domain was used for the casing treatments with a RANS Harmonic approach taken to observe the unsteady effects of the recirculation [9]. The mesh used focused on orthogonality around the injection point and was expanded to 148 million cells per passage [9]. Shock waves were able to be resolved despite the injection flow forward of the rotor. This study is likely beyond the scope of this project, but validation is provided for recirculating casing treatments and computational approaches [9].

1.2.2 Internal

The NPS Turbopropulsion Lab (TPL) received an advanced transonic compressor known as the NPS Military Fan (NPSMF) in 2010 and has been conducting research on it since then. Figure 1.5 shows the compressor blade-disk part ("blisk") prior to installation [3].

Initial work focused on characterizing the compressor performance [3] and characterizing instabilities which could lead to stall [10]. McNab [3] developed the first CFD model of a single passage of the NPSMF which was used until 2021 when Meinster [11] updated the model to better match the compressor geometry and increase the mesh fidelity. He performed

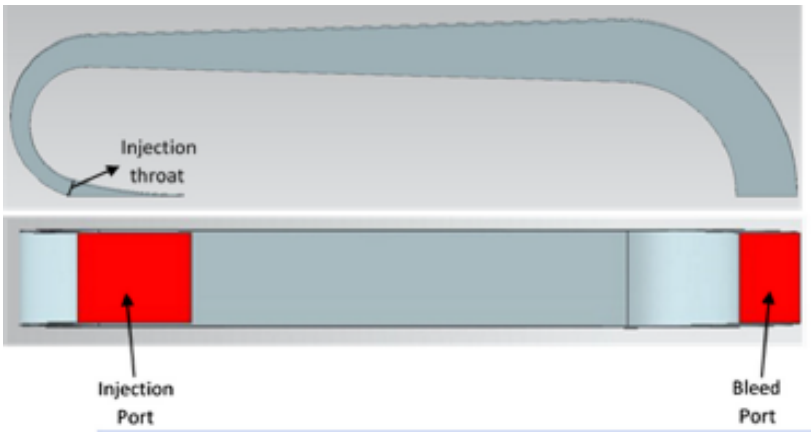


Figure 1.4. CSIR self-recirculating casing treatment design. Source: Kumar et al. [8].



Figure 1.5. NPSMF Blisk before installation in the TCR. Source: McNab [3].

a validation study and used experimental data to validate the computational results for both performance and efficiency. Both showed good agreement. In his study it was found that y^+ and inflation uniformity around the blisk were critical in resolving the flow. This resulted in a large, unstructured mesh of 23 million elements [11]. The bulk flow used tetrahedrons while surfaces used higher order prismatic elements generated using inflation layers. Extensive use of inflation layer controls along with sizing controls to maintain a reasonable aspect ratio were required. In regions of close tolerances – namely the blade tip clearance – further

sizing was conducted to allow resolution of the blade tip gap. The nominal CFD case had a tip gap of 0.015" which is on the scale of the blade boundary layer leading to high shear between the blade and the endwall. It was found that CFD does not adequately capture the stalled state when modeled as a steady condition, but he was able to identify the modes and states immediately prior to stall and approximate the stall mass flow [11].

Location(s)	Mesh Feature	Effect(s)	Relative Importance Low (1)-->High (5)
N/A	Bulk mesh size	Mesher/Solver time	3
		Overall flow resolution	4
		Shock resolution	5
		Solver stability	2
Blade surface	Inflation Settings*	Blade Yplus	5
Blade LE/TE		Shock resolution	2
Hub surface		Mesher/Solver time	4
Casing wall		Inflation uniformity	5
Inner wall		Meshing Success**	4
Blade surface	Face Sizing	LE/TE faceting	5
Blade LE/TE		Inflation aspect ratio	4
Hub Surface		Mesher/Solver time	5
		Overall flow resolution	3
		Inflation uniformity	4
		Overall mesh quality**	3
Periodic surfaces	Match Control	Overall flow resolution	3
		Shock resolution	2
		Solver time	4
N/A	Global mesh quality & sizing settings***	Overall mesh quality**	2
Small faces/edges	Pinch Controls	Overall mesh quality**	1
		Inflation layer uniformity	1
N/A	Virtual Topology (Automatic)	Overall mesh quality**	1
Small faces/edges	Virtual Topology (Manual)	Overall mesh quality**	1
* Refers to Inflation first layer thickness, selection of surfaces to inflate, maximum number of inflation layers, inflation growth rate, and inflation algorithm			
** Refers to the ability of Ansys meshing module to successfully generate a mesh using the given settings			
*** Includes automatic mesh defeaturing, curvature capture, proximity capture, target metrics (skewness, orthoganality, aspect ratio, etc.)			

Figure 1.6. Meshing priorities. Source: Meinster [11].

With the fan characterized by Londono [10] and McNab [3], research began on advanced casing treatments to improve the stall margin at high pressure ratios. The primary challenge faced by previous research is the manufacture of unique casing treatments. Traditionally,

axial and circumferential casing treatments require a lengthy machining processes to meet the tolerance requirements inside the compressor, and traditional machining process do not easily allow the manufacture of self-recirculating passages contained in the casing. This has led to complex apparatus such as the one used by NASA which use controlled high-pressure bleeding of the compressor [2]. In 2018, DeSousa [12] experimented with the possibility of using epoxy and additive manufacturing to allow the rapid prototyping of casing treatments. His studies concluded that epoxy can be used as the compressor endwall in place of aluminum; however, additively manufactured plastics cannot withstand use in the compressor and have fidelity limitations [12]. Using epoxy in the endwall allows casing treatments to be machined much more quickly using the same infrastructure as an aluminum endwall. This does also imposes traditional machining limits on the casing treatments. Additive manufacturing is promising, but in its current state, the plastic prints are relatively rough and shrink and distort at the scale needed for this application. DeSousa's [12] study did not go beyond the validation of 3D printed plastics as a possibility for casing treatments. The incorporation of 3D printing opens the door to more advanced and creative devices as they are not limited by traditional machining constraints.

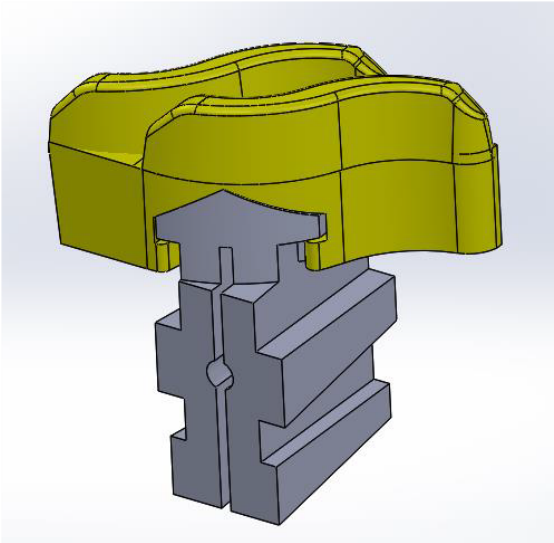


Figure 1.7. The smooth 3D printed endwall as viewed from the inlet.
Source: DeSousa [12].

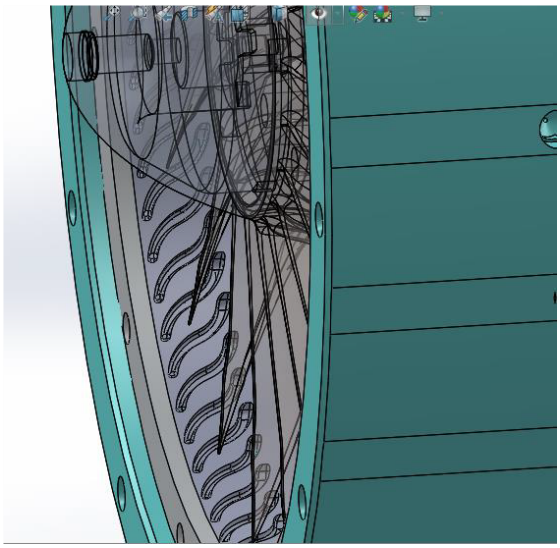
In 2021, Green sought to combine the techniques developed by DeSousa [12] and created a method for combining additively manufactured designs with epoxy layup techniques. Green developed a technique to use additively manufactured plastic molds to create epoxy

endwalls with built in casing treatments [1]. This development gave the benefits of epoxy endwalls (strength, ability to be machined post-layup, ease of machining) with the flexibility of 3D printed casing treatment designs. Two of his designs were put into production. A more traditional s-shaped groove variant of an axial endwall treatment and a novel self-recirculating internal passage, as seen in Figure 1.8.

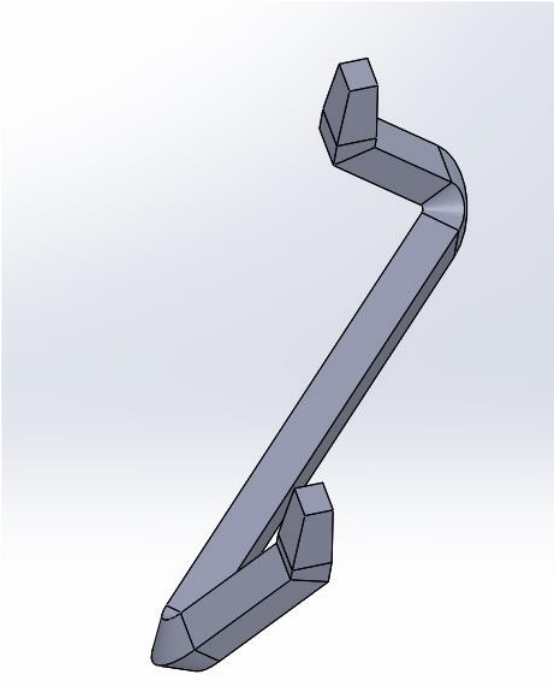
These treatments are designed to increase the stall margin by allowing minor flow recirculation at the blade tip delaying the onset of stall. Previous studies in low-speed axial compressors demonstrated a 36% stall margin improvement with no efficiency loss using the s-shaped grooves [4]. Work done by Hathaway using bleed air to recirculate flow demonstrated a 225% increase in stall margin and a 5% loss in adiabatic efficiency in an axial compressor [2]. This system was more complex and was able to vary mass flow recirculation, so the large stall margin increase is not to be expected but it is thought a similar result may be achieved at significantly less cost. This study seeks to validate the designs presented and validate CFD techniques to aide in further design work.



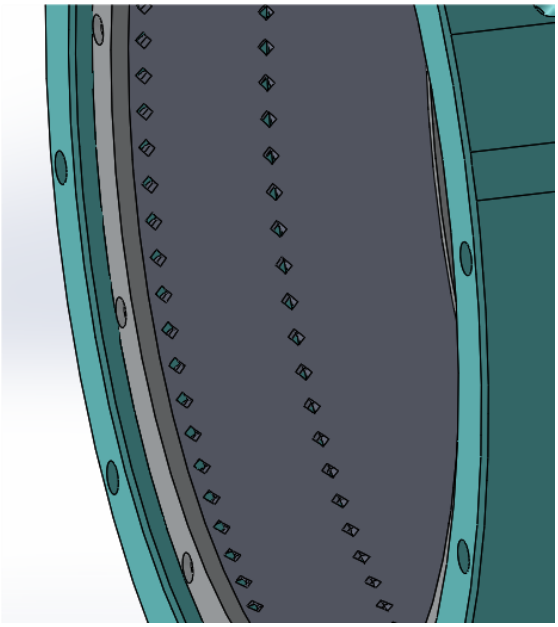
(a) Mold for s-shaped axial grooves



(b) SolidWorks rendering of s-groove casing treatment.



(c) Mold for internal passage.



(d) SolidWorks rendering of internal passage casing treatment.

Figure 1.8. Overview of casing treatments for this study. Source: Green [1].

1.3 Current Study

The NPSMF has been the attention of much research in the past decade due to its advanced design and potential application. Stall margin improvement of first stage compressors has many applications. Gas turbine power generators can use first-stage stall mitigation devices to allow a more efficient idle power operation. In aircraft, gas turbine propulsor operations at high angles-of-attack and rapid accelerations of the turbine are much safer with a larger stall margin.

This study aims to unite the computational and experimental methods developed by Meinster [11] and McNab [3] with the work of Green [1] to develop techniques for the evaluation of casing treatments in transonic axial compressors. Work outside of NPS has shown the viability of modeling stationary components around the rotor using various techniques built into ANSYS CFX. These techniques will need to be adapted to fit into the framework developed by Meinster [11] and model the geometries proposed by Green [1]. Additionally, the results of the numerical study will deepen the understanding of the experimental results and aide in future endwall devices. Computational analysis can serve to fill in the blanks left by the TCR and deepen the physical understanding of the interactions occurring at the compressor casing to guide future TCR experimentation. Once matured, these techniques will allow for the rapid testing and evaluation of further advanced transonic casing treatments and reduce the cost in verifying their effectiveness.

THIS PAGE INTENTIONALLY LEFT BLANK

CHAPTER 2:
Experimental Facilities and Setup

2.1 Transonic Compressor

The Transonic Compressor Rig (TCR) is designed to allow rapid configuration changes to enable the testing of various layouts and operating conditions. Previous work has focused on evaluating the rotor only (or half-stage) configuration [3], [11]. Experimentation involved the exploration of the effect of tip-gap and the evaluation of stall modes. Current studies aim to evaluate the effects of advanced casing treatments for the improvement of stall margin and the effects these features have on the stall modes. As these casing treatments are intended for operational use, the TCR was configured to mimic an operational configuration. A full compressor stage was used (rotor and stator) and inlet guide vanes (IGVs) were introduced. Initial testing involved the evaluation of the full stage with a previously established smooth casing treatment and evaluation of the effect of whirl introduced by the inlet guide vanes. Final testing was conducted using the IGV-Rotor-Stator (IRS) configuration with the casing treatments installed. Figure 2.1 shows a cross-sectional drawing of the TCR in the IRS configuration.

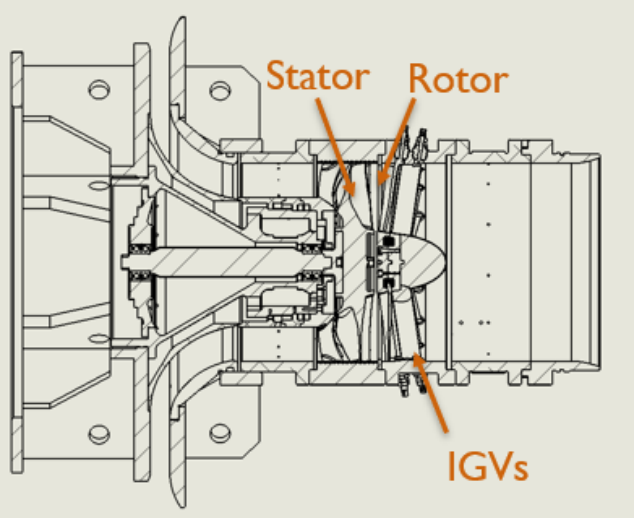


Figure 2.1. A section view of the TCR in the IRS configuration.

The TCR operation is described in detail by McNab [3], but the principles of operation are described here for completeness. A 12-stage axial compressor powered by an electric motor provides high-pressure air to the TCR drive turbines. Excess air from the compressor also provides back pressure for the compressor test section. An atmosphere bleed valve allows the TCR static back pressure to be controlled independent of the pressure supplied. Air is ingested by the compressor through a bellmouth mass flow meter and flow straightener before being taken through a straight inlet conduit. A throttle assembly is built into the flow straightener to allow regulation of the mass flow into the compressor. This set up allows for control of the inlet stagnation pressure and the outlet static pressure.

Steady-state pressures and temperatures were measured inside the TCR. Data was time averaged at each test point to ensure steady-state conditions, limiting analysis of transient behaviors. The total pressure ratio, isentropic efficiency, and mass flow rate were the key parameters looked at in this study. Equations presented by Descovich [13] were used and include corrections for ambient temperature, pressure, and relative humidity.

2.2 Inlet Guide Vanes

Inlet Guide Vanes are a key part of the experimental set up. The guide vanes introduce whirl in the flow before it enters the compressor reducing the load put on the rotor. The velocity triangle diagram shown in Figure 2.2 demonstrates the reduction in angle-of-attack which the IGVs generate. This reduction in work in the first stage is necessary for high-performance compressors. Without the IGVs, many modern compressors would face compressor stall in the first stage while the aft stages are choked and cannot handle the flow ingested. The IGVs reduce the mass flow entering the compressor to prevent the later compressor stages from chocking and reduce the work done by the first stage to prevent compressor stall. For fielded systems, the IGV flap angle is actively controlled to keep the compressor within its operating specifications, but in the experimental rig flap angles are set prior to each test condition. Appendix A details the method used to set the flap angle. The IGVs used during the experiments have a complex geometry which reduces the amount of whirl toward the hub serving to increase the load on the blade root while unloading the blade tip in their design condition.

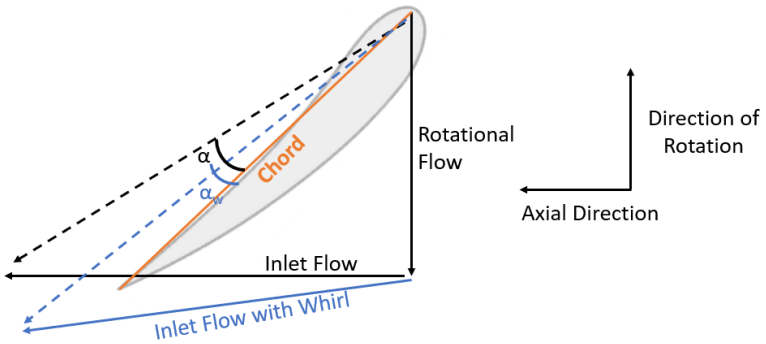


Figure 2.2. Reduction of compressor blade angle-of-attack due to inlet guide vane whirl.

2.2.1 Inlet Guide Vane Uncertainty

After the IGV blade angles were set using the 3D printed jig, the blade angles were measured to verify the product and get an uncertainty value for the blade angles. Due to the geometry of the blade, the angle could not be measured directly, so instead a depth micrometer was used to measure the distance from the back of the IGV rig to the trailing edge of the blade, as shown in Figure 2.3.

This was done for all 17 blades and compared to the same measurement in the SolidWorks model for the set angle. In order to get the actual angle deviation from the depth measurement, the blade length was measured in order to create a closed geometric problem. The measured error is the difference between the SolidWorks value for the trailing edge to the rear of the IGV rig and the depth micrometer measurement.

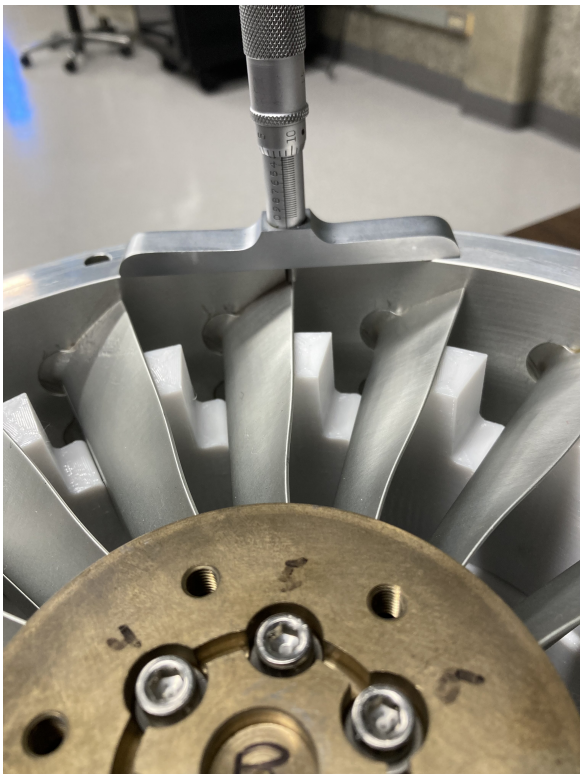


Figure 2.3. Using a Vernier depth micrometer to measure depth of trailing edge to a thousandth of an inch.

Finally, the blade twist and the diameter of the depth probe had to be accounted for. Because the depth micrometer is not measuring at the true tip of the blade but rather the highest point on the trailing edge within one probe diameter from the wall and the blade twists rapidly, an angular bias is introduced. To account for this, SolidWorks was used to model the bias. A horizontal tangency line was placed on the trailing edge of the blade as shown in Figure 2.4.

From here, a line was drawn along the trailing edge which is the same length as the depth micrometer's diameter and is coincident with the tangency line; this is the point where the depth micrometer actually contacted the IGV blade. With this point marked, a plane was made flush to the IGV end cap where the angle is actually set. The contact point of the depth micrometer was then projected out onto this plane. A line connecting the rotation axis of the blade and the projected point was constructed. This line is shown in Figure 2.5.

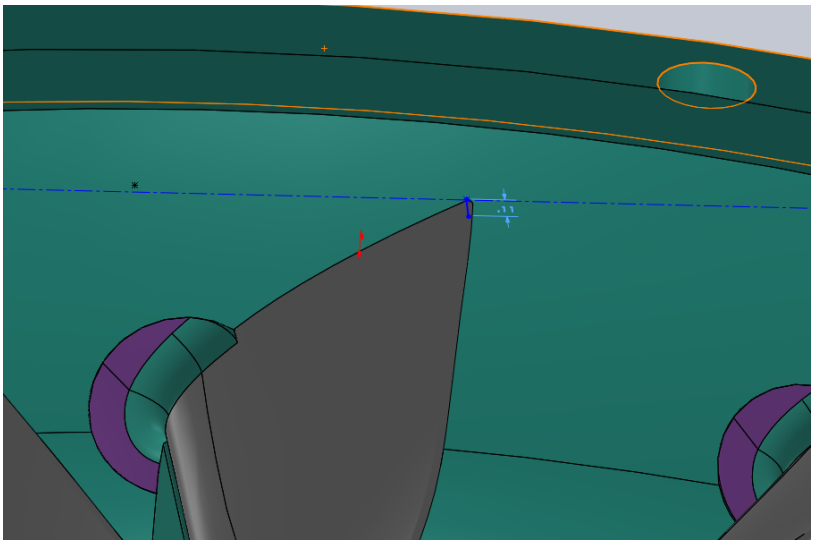


Figure 2.4. The horizontal tangency line and the probe offset used to calculate angular deviation.

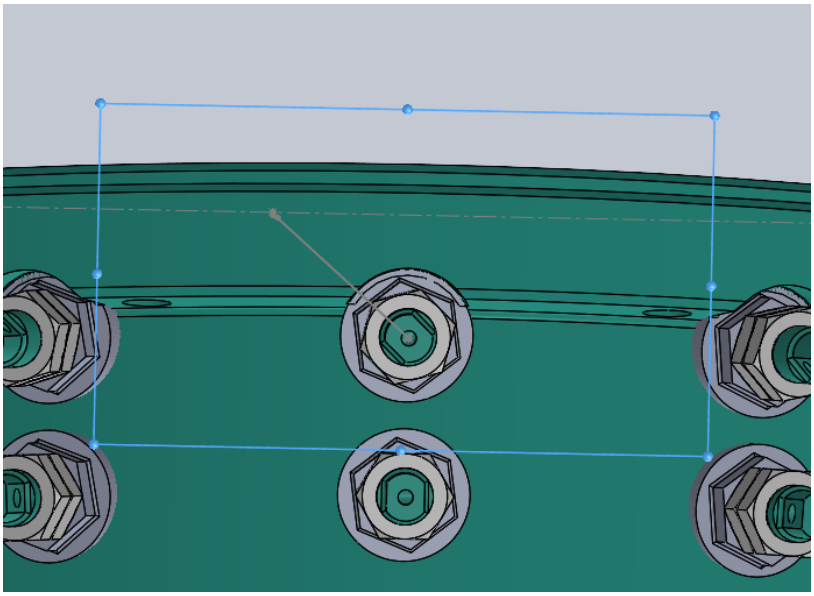


Figure 2.5. The plane (in blue) is perpendicular to the blade end and allows the distance between the axis of rotation and the probe contact point.

This method allows the bias to be read at different set angles without any need to redefine the contact point. The bias at the first test condition was 2.91° more closed and 3.17° more closed at the second test condition. The variance is presented below in Figure 2.6 for the three bladed jig and the revised full ring jig. Figure 2.7 compares the error distribution for the full ring and the three bladed jig.

As can be seen from Figures 2.6 and 2.7, the 3D printed jigs tend to push the blades more open than intended resulting in less whirl than expected. For both jig methods, the error generally is less than 1.5°, but the three-bladed technique is less consistent. This is apparent from the red and blue data points in Figure 2.6. Both used three-bladed jigs and yet they follow different error trends with the 80% line showing one blade which is 3° off of the mean error (blade 15). Blade angle error is still present when using the full ring, but it is more consistent. A normal distribution of error can be seen in the histogram of blade error for the full ring seen in Figure 2.7 whereas the three-bladed jig demonstrates an abnormal, binodal distribution. These findings will be accounted for in the experimental error distribution and jigs for future experimentation can account for the 0.75° average error when using the ring method.

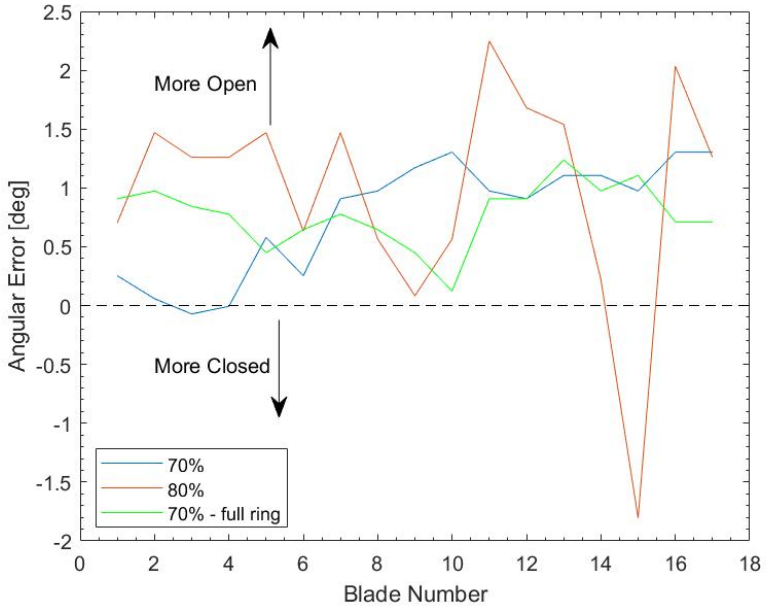


Figure 2.6. The angular deviation measured in the IGV rig.

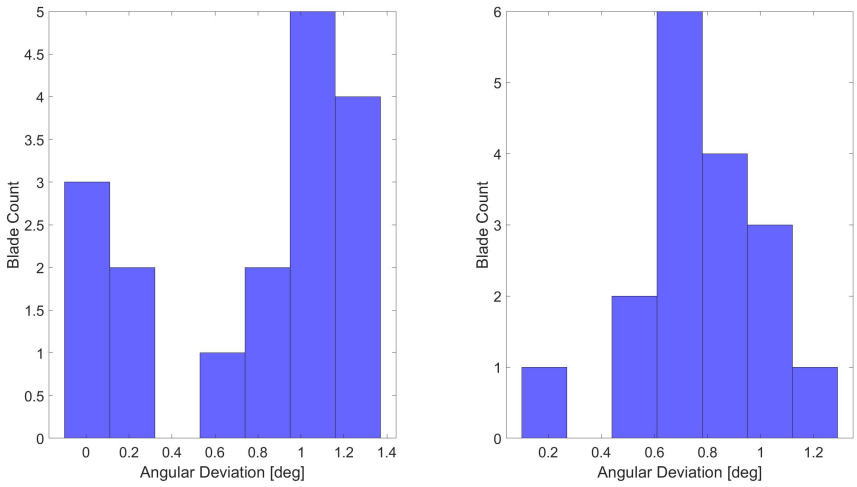


Figure 2.7. Comparison of the error found with the three-bladed (left) and complete IGV jigs (right).

2.3 Test Conditions

The TCR was tested in three separate configurations over the course of this study. Full-stage testing with the NPSMF and stator was conducted to characterize stage performance, testing in the IRS configuration was conducted with a smooth endwall to characterize the IGV contribution, and finally testing was conducted in the IRS configuration with the s-shaped axial groove casing treatment installed. Unfortunately, testing was delayed for the internal passage design as the delivered product was not deemed suitable for the TCR environment. Testing with the rotor only and instrument layout can be found in the work of McNab [3] and Meinster [11], but is presented in this report in part for accurate comparison of the casing treatment performance. Figure 2.1 shows the layout of the TCR in its current configuration.

While the NPSMF is designed for 30,000 rpm, the TCR is power limited, so testing was limited to 90% of designed operating conditions. Additional data was taken at the 70%, 80%, and 85% power settings to fully characterize the TCR.

2.3.1 NPSMF Stator

The stator is a stationary set of blades which sits directly behind the NPSMF as can be seen in Figure 2.1. Stators serve two purposes in compressors. First, stators serve as nozzles

behind the compressor to further boost the static pressure by converting the kinetic energy from the rotor. While the blades are stationary, a relative whirl velocity is generated by the compressor blades and acts on the stator blades. This leads to the second purpose of the stators, flow straightening. By applying a counter-whirl to the flow, the flow is returned to an axial direction. In a multistage compressor, this straightening of the flow provides the next stage with a more axial inlet flow and prevents the air in the compressor from just spiraling around the central hub. Figure 2.8 demonstrates the flow correction generated by the stators. Calculations used in data processing of the rotor only configuration accounted for the whirl present in the flow downstream of the rotor; these compensations were removed when the full stage was tested.

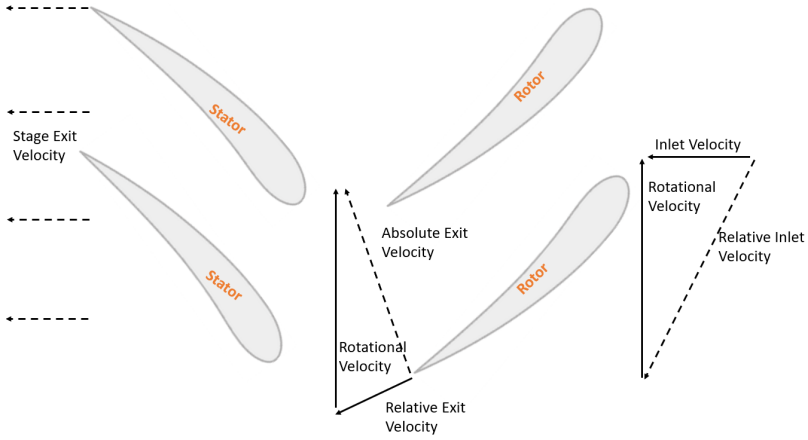


Figure 2.8. Rotor-stator speed triangle interactions.

2.3.2 Inlet Guide Vanes

IGV operation and theory is discussed above in Section 2.2. The IGVs were set based off of a predetermined schedule of angles. Each operating condition had its own prescribed flap angle which are labeled as the operation power percentage or as in accordance with schedule (IAWS) when used at the designed condition. At lower power settings, the IGV flap angle is set to introduce more whirl into the flow which is denoted as a larger flap angle. Testing was conducted for each power setting with the IGVs set IAWS but several tests were conducted off of the determined schedule. These off design tests used the flap angle from other power settings. Early results pointed toward the benefit of additional whirl, so tests were conducted with more whirl than is prescribed by the schedule. Table 2.1 presents

the IGV settings used for each test condition. For each of the test condition and flap angle combinations shown below, the smooth casing end and s-shaped groove casing treatment were tested.

Table 2.1. The IGV conditions tested in the TCR.

Tested Condition	**IGV Angles Set**
70%	70%
80%	70% 80% 85%
85%	70% 80% 85%
90%	70% 90%

2.3.3 Smooth Endwall

The baseline TCR performance was evaluated using a smooth epoxy endwall as presented in DeSousa [12]. This endwall configuration is less robust than a traditional metal endwall and allows for slight abrasion from the rotor blade tips as the rotor grows under load. The cold-blade clearance used for this experiment was 0.015 in or 0.42% mean blade height, but this gap decreases as rotor RPM increases due to centrifugal acceleration on the blade. This is the same tip-gap used in previous rotor only experiments.

2.3.4 S-Shaped Axial Casing Treatment

Green [1] developed a technique to combine epoxy lay ups with the 3D printing techniques of DeSousa [12] to enable experimentation with transonic endwalls. The s-groove casing treatment displayed previously in Figure 1.8 was developed from subsonic casing treatments and are designed to eliminate blockage from tip-leakage vortices [1]. The s-grooves were designed and placed such that the inlet and outlet corresponds with the high and low pressures measured by Londono [10]. The nominal tip-gap between the treatments is kept at 0.015 in and the treatment tested has 76 individual grooves.

2.4 Procedures

The TCR was operated in accordance with previously established guidelines McNab [3] and is only summarized here. As previously discussed the TCR is throttled via the inlet mass flow while the discharge back pressure is maintained at a relatively constant pressure as it discharges to atmospheric conditions. After configurations were set for the desired operating point, the rotor was accelerated to the desired rpm by increasing the pressure fed to the drive turbines.

To advance the TCR along the speed line, the throttle valve was incrementally closed. Previous operating lines were used to move the throttle in safe and reasonable increments. Two means were used to set throttle position. Position can be visually set by observing a manual gauge on the throttle assembly in the test cell. This method was used for points within the normal operating region where the compressor was not at risk of stall. A secondary method involving timed relay control was used near the expected stall point as minor throttle movements (less than 0.5% of throttle range) could be made and allowed the compressor to be rapidly brought out of stall once a stall was detected. Throttle positions were recorded for the benefit of future experiments but were not used in the data interrogation. As such, the precise the throttle position achieved by the timed relay control was not crucial to the test. Use of the relay control allowed for the stall point to be more precisely established.

At each new throttle position, the back pressure and drive turbine feed pressures were adjusted to maintain the rotor rpm then it was allowed to stabilize before data collection began. A running average of data samples over a one minute period was used for the steady-state values.

A jog method was used to establish the compressor stall point. As the rig approached the historic stall point, the throttle was moved to a slightly more closed position then allowed to stabilize. Signs of stall were carefully monitored as the throttle was adjusted. This process was repeated until stall was detected as evidenced by a sudden reduction in mass flow rate, pressure ratio, efficiency, and typically accompanied by significantly increased sound and vibrations. At the first sign of stall, the throttle was opened to allow the compressor to unstall and stabilize. The goal was to find the minimum throttle position required to stall the rotor and allow data acquisition up until stall occurred.

CHAPTER 3:
Computational Setup

3.1 Geometry

The casing treatment was modeled as a separate domain in ANSYS CFX. This allowed the casing treatment to be held stationary while the compressor blade gas passage is revolved underneath it. SolidWorks was used to model the treatment and attach it to the compressor gas passage developed by Meinster [11] described earlier; the gas passage with s-shaped grooves is demonstrated in Figure 3.1.

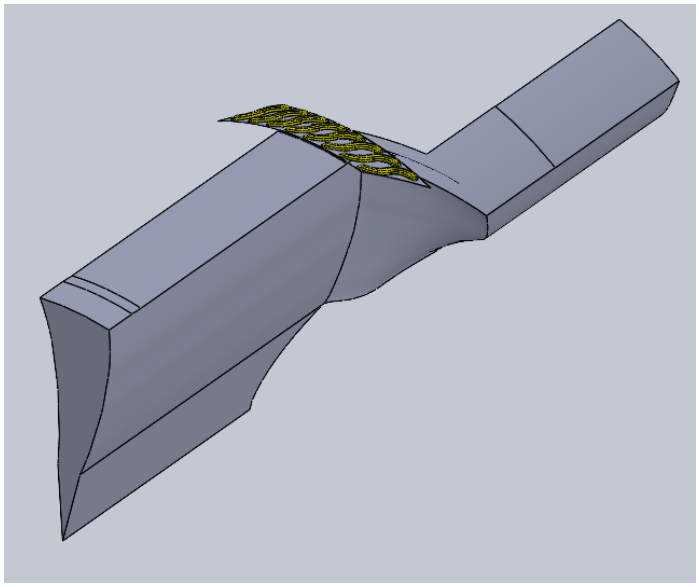


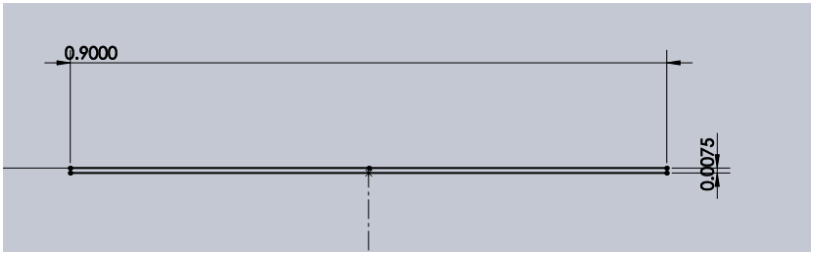
Figure 3.1. The final s-shaped axial groove casing treatment mounted to the single blade gas passage.

Two distinct parts compose the treatment domain. A thin annulus provides the interface surface to connect the treatment with the gas passage, and s-shaped grooves and internal passages designed by Green [1] are connected with this annulus. The annulus serves as a sliding layer which transfers information between the rotating gas passage and the casing treatment. Modeling the casing treatments directly with the gas passage was considered, but it limits the flexibility of the tool. Traditionally, the compressor endwall is modeled as part of

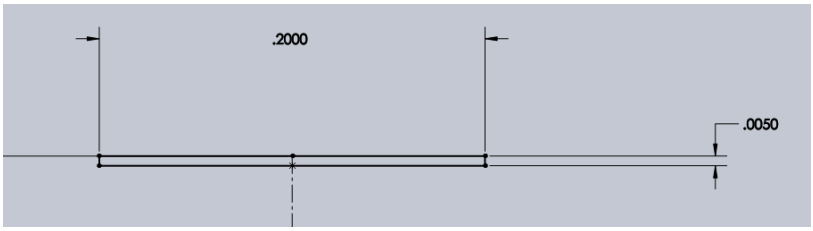
the rotating domain. In the physics editor, the walls are set as walls with velocity. A counter-rotating boundary condition is applied which approximates the rotational component of the skin friction on the inner and outer walls which is necessary for good boundary layer development. If the casing treatment was modeled as this counter-rotating wall, the slots would be limited to a fixed position in relation to the blade. The frozen rotor interface is similar to this set up, but there is functionality within the frozen rotor interface to allow angular adjustments to be made between the stationary and rotating domains. Other physics models such as mixing planes and Fourier transforms were not considered in this study as they are not suitable for a single passage analysis.

A sliding layer was developed for connecting the treatments with the gas passage. A thin, rectangular section was used as a sliding layer; the s-grooves were placed on top of this layer to make the treatment domain model. A thickness of slightly less than 50% blade tip clearance was used vice the thin layers of Chen et al. [4]. The larger layer allows for similar size meshes on either size of the interface with adequate boundary layer resolution, without the need for the extraordinarily high mesh element count found in Rolfes et al. [7]. Sizing the passages so there is not unnecessary overlap with the blade reduces the cell count necessary to resolve the blade tip clearance. The sliding layer is designed to be flexible in use. As it was modeled as separate part from the treatment or gas passage, its radius, depth, and axial length can be adjusted to fit any casing treatment on models with varying tip gap thickness.

The internal passages used a similar sliding layer as the s-grooves; however, the internal passages used two sliding layers: one behind the blade at the passage inlet and one in front of the blade at the passage outlet. Aspect ratio of the passage was not found to be of critical importance, so a similar depth was used, but the axial length of the passage was smaller. Additionally, these sliding layers did not lay over the blade tip allowing for easier meshing. Figure 3.2 shows the profiles of the sliding layers for both treatments with the sizing measurements visible.



(a) For Axial Grooves



(b) For Recirculating Passages

Figure 3.2. Cross-sections of the sliding layers used for the axial grooves and recirculating casing treatments.

Based on Green's specifications for the s-grooves, 76 grooves were evenly spaced around the casing which is 3.8 grooves per passage. The domain as described is shown in Figure 3.3 The s-shaped grooves modeled by Green [1] are designed to be used in the manufacturing process of the casing and is sized for the jig apparatus and had to be adapted for the CFD model. Placement in the CFD model was based on the designed depth as specified by Green [1]. One s-shaped groove was placed in an assembly with the domain interface annulus. With the groove placed the correct distance from the rotation axis, the "cavity" tool was used to remove the intersecting lower part of the groove. This leaves just the actual groove perfectly flush with the upper surface of the domain interface and saves the process of matching curved faces. This technique allows for rapid changes to be made in the model radius for tip gap adjustments and to allow new casing treatments to be rapidly modeled. A circular pattern was created to model the 76 evenly spaced grooves around the domain. Once the full treatment was modeled, the assembly was saved as a single part file. This converts all of the individual parts into imported bodies in the part. Using the "combine" tool, the 77 individual bodies were combined into one body. This helps with the set up in CFX as it leaves only two bodies in the finished assembly (the treatment and the gas passage).

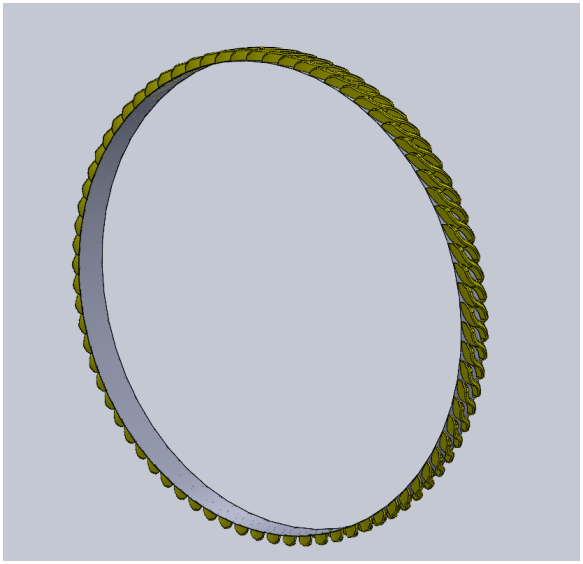


Figure 3.3. The full s-shaped axial groove casing treatment domain.

Only a section of s-grooves long enough to cover a single passage was modeled. This is still physically realistic if axi-symmetric flow is assumed in each blade passage. Like the gas passage, the treatment domain was cut to provide a periodic boundary. Due to the complex nature of the groove shape, axial cuts would not provide the periodic conditions necessary. A helix was approximated in order to generate two symmetrical cuts between the grooves. To approximate the helix necessary, two wedges were drawn on the leading and trailing edges of the treatment domain as seen in Figure 3.4.

These wedges were based at the origin and share the same angle. The wedges were then given an angular offset to account for the angle formed by the casing treatment. Two planes were then drawn using the origin and the two upper points of the wedges on the left and right respectively. Extruded cuts were then made from these planes leaving only the casing treatment found in the wedge. Cutting in this manner ensures the boundary condition will be periodic. Several grooves were left atop of the single blade passage so that multiple channels of the casing treatment can be observed at once without a need to offset the blade. In this configuration, multiple passages are in front, behind, and on top of the blade providing a full picture of the process of moving the blade pass the treatments. The final design is shown below in Figure 3.5 and is shown with the gas passage in Figure 3.1 previously.

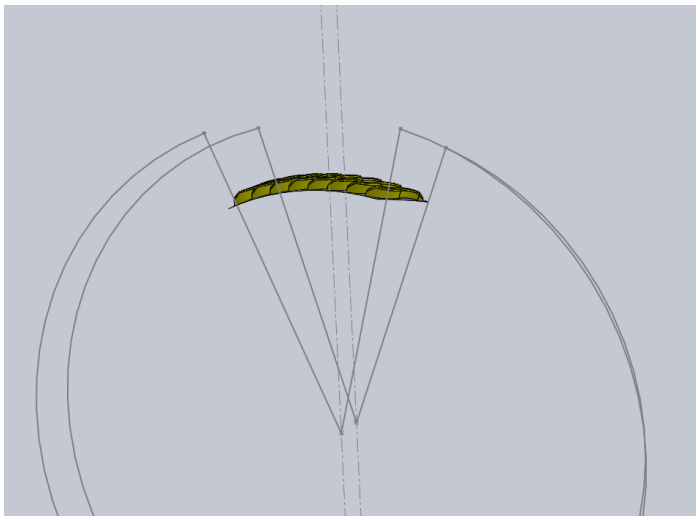


Figure 3.4. The slicing method used to make periodic boundaries.

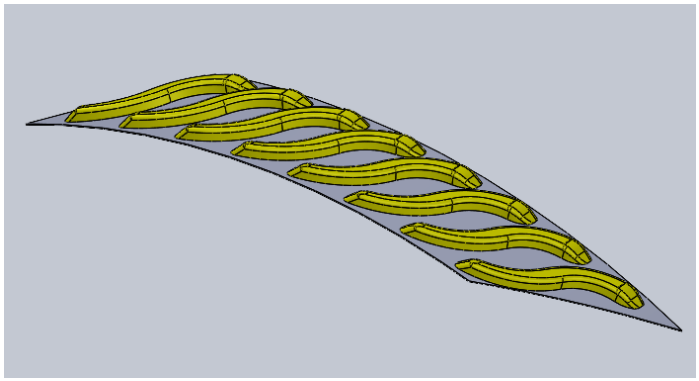


Figure 3.5. The final s-shaped axial groove casing treatment domain demonstrating the periodic cuts.

A similar process was used to make the internal passage domain. Due to the narrow nature of the design, significantly more passages were able to be used and can be varied to get the mass flow desired. The primary specification is a prime number to avoid any unnecessary excitation of the blade. This is of particular importance with the internal passages due to the discrete nature of the injection ports. Passages were placed at the correct axial distance then the two sliding layers were added centered to the passage bleed and injection ports. The cavity command and circular pattern were used like the s-shaped grooves discussed previously. Periodic cuts were made in the domain and individual bodies were combined to make one part out of the domain. Figure 3.6 depicts the cut domain for the internal passages

with Figure 3.7 showing the passages mounted to the domain.

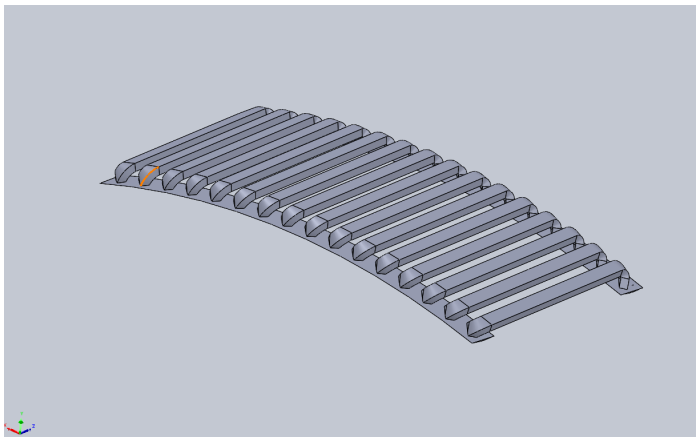


Figure 3.6. The final internal passage casing treatment domain demonstrating the periodic cuts.

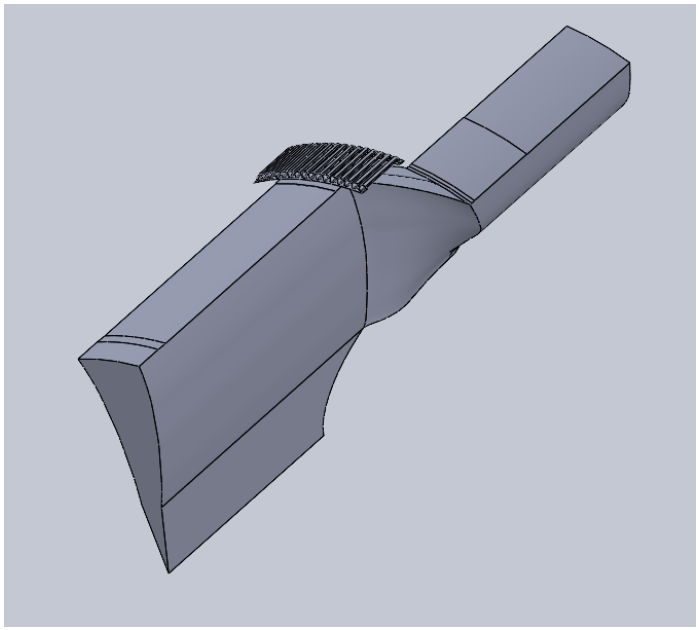


Figure 3.7. The final internal passage casing treatment mounted to the single blade gas passage. The aft cut in the gas passage is visible.

3.2 Modeling

3.2.1 Mesh

The mesh was generated using the built in CFX meshing program found in the commercial program Ansys Workbench. A patch conforming tetrahedron method was used in the main gas passage and a proximity capture method was used in the casing treatment domain. Selections of face sizings and inflation layer controls were used to create the refined mesh around the compressor blade while the inlet and exit passages were left relatively coarse to aide computational speed. Match controls were used on all periodic boundaries in the gas passage and casing treatment to improve the computational speed of the model and limit periodic interfacial averaging. Inside the casing treatment the mesh blends from structured near the interface into an unstructured mesh similar to the inlet section. The final meshes used between 25 million and 35 million elements. An example mesh on the s-shaped groove model is shown in Figure 3.8 Further details of the mesh and methodology can be found in Chapter 4.

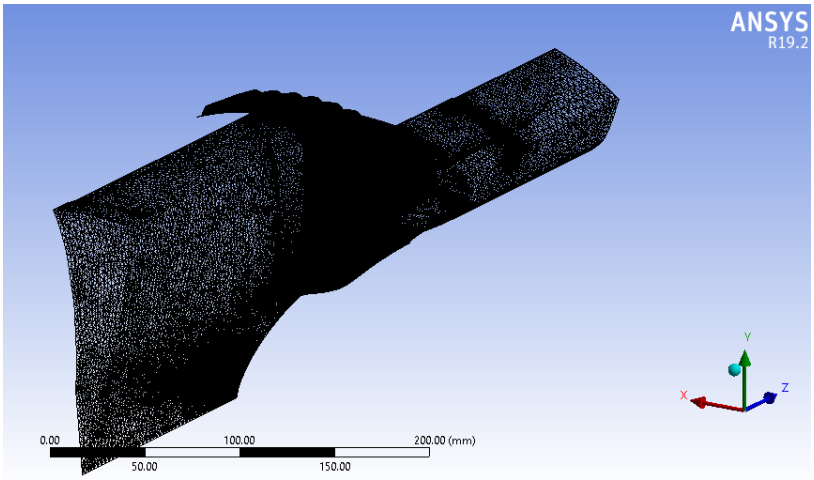


Figure 3.8. The final mesh for the s-shaped axial groove geometry.

3.2.2 Physics

Flow through the TCR was modeled using ANSYS CFX R19.2. Rotational periodicity was used for both the blade gas passage and the casing treatments examined. Two domains were used to model the casing treatment-rotor interaction. A stationary domain was used

for the casing treatment while the rotor was set to rotate. Multiple channels of the casing treatment were used to allow for examination of the treatment at multiple relations to the blade. Steady-state flow was simulated with the Shear Stress Transport (SST) model and the gamma-theta laminar-to-turbulent boundary layer transition model.

Inlet and outlet boundary condition pressures were used to drive the compressor performance lines. Similar to the TCR and previous studies, the relative static back pressure boundary condition was held constant while the inlet relative stagnation pressure was depressed to drive up the pressure ratio across the compressor. The inlet stagnation pressure was driven down in increments until numerical stall was observed or convergence could not be reached.

3.2.3 Test Conditions

Two configurations of the TCR were modeled using CFD. Initially, rotor only tests were conducted with casing treatments installed and compared to previously taken rotor only data. No casing treatment data was collected on the TCR in the rotor only configuration, rather it was taken in the IGV-Rotor-Stator (IRS) configuration. Modeling of the stator was not conducted in ANSYS as it would greatly increase the computational power required and does not directly affect the performance of the casing treatments. A swirling inlet flow was applied to simulate the unloading effect of the IGVs to reduce the computational expense. The swirl angle was modeled using a linear interpolation of the hub and casing flap angles measured from the IGV and applied in the cylindrical coordinate frame across the compressor inlet. This allowed analysis of the IGV affect on the performance of the casing treatments tested and better comparison to experimental results. A user-defined function was created to create the linear approximation based off of the flap angle schedule described earlier.

3.2.4 Boundary Conditions

A new method of driving the compressor speed line was developed for analyzing numerical compressor critical points. The inlet stagnation pressure was reduced while the static back pressure of the compressor was held constant in order to increase the work done by the compressor and reduce the mass flow through the model. Both the inlet and outlet of the blade gas passage were held stationary and pressure boundary conditions were applied to each. The more traditional method of driving the speed line is to reduce the inlet pressure

in discrete increments then allow the simulation to stabilize. This ensures a steady-state performance result similar to the data recorded from the TCR. For the models used, a converged solution was achieved within 300 - 400 iterations (around 700 CPU hours). At each new inlet pressure, performance data and visuals were recorded and examined to ensure the simulation had not stalled. Once the model did stall (defined as a sudden drop in mass flow, flow separation, and recirculation in the passage), the inlet pressure was set at 50% of the pressure drop which caused the model to stall. Stall conditions were then examined at the new, higher inlet pressure. If stall was still detected, the inlet pressure was again raised by 50% of the previous drop. This process was iterated until the model was barely in the stalled condition. This method was used by Meinster [11] and is further analyzed in his work.

Discrete pressure drops are similar to the method used in the TCR, but they are costly in the CFD simulation. The user must at all times monitor the simulation and make manual adjustments for each new test point. This reduces the number of points which can feasibly be taken. In the near stall region, hysteresis can take hold. Once stalled, the simulation cannot always be brought out of stall to match the pre-stalled conditions. In these scenarios data points must be deleted and the simulation restarted with a better approximation of the target stall location. Thus the stall point is dependent on the patience and skill of the user. Over a total pressure drop of 23,000 Pa from wide open throttle to stall, increments of 100 Pa were found to be the best resolution achievable.

A pseudo-steady approach was also used in this study to reduce computational time and increase the resolution of the stall point. This approached used a user-defined function for the inlet pressure to steadily decrease the inlet pressure in small increments between iterations. By reducing the inlet pressure in extremely small increments, the simulation can be assumed steady with good accuracy while keeping residuals low and eliminating hysteresis around stall. This approach also allowed a steady-simulation to approximate performance in unsteady-regimes found when using casing treatments. An expression was established to hold the inlet pressure steady for the first data point for the first few hundred iterations to allow the model to reach an initial convergence. The model then automatically began incrementally reducing the inlet pressure between iterations. Equation 3.1 presents the pseudo-code representation of the function used to drive the pressure.

$$
\begin{aligned}
&\text{if (current iteration} < \text{\# of steady iterations)} \\
&\quad P_{in} = \text{initial pressure} \\
&\text{else} \\
&\quad P_{in} = \text{initial pressure} + \frac{\text{current iteration}}{\text{final iteration}}(\text{final pressure - initial pressure}) \\
&\text{end}
\end{aligned}
\tag{3.1}
$$

The initial pressure was set at a slightly positive value to capture flow choke through the compressor and the final value was set at 10% - 15% below the critical point found using the true steady method. As depicted in Equation 3.1, the pressure drop is sized by a function of the total iteration count. The total number of iterations is defined by Equation 3.2.

$$
\text{final iteration} = \text{steady iterations} + \frac{\text{final pressure - initial pressure}}{10\ [Pa]} \tag{3.2}
$$

The steady-state portion of the simulation was set based on previous experience with the steady-state approach to numerical compressor performance. For very stable cases (wide-open throttle, low RPM, etc), as few as 300 iterations were used to achieve initial convergence, but for more complex simulations, 500 iterations was chosen as the standard value. The pseudo-steady iteration count was sized such that a 10 Pa pressure drop (0.00145 psi or 0.01% of standard atmosphere) was achieved between iterations. Monitor points were set in the simulation to record the desired data resulting in continuous streams of data vice the 6-7 discrete points generated in the prior method. Back up files were saved on predetermined intervals to allow visualization along the power curve. Figure 3.9 depicts the inlet pressure drop for the steady and pseudo-steady solutions throughout the simulation. The steady method only records data at the vertices, but the pseudo-steady generates continuous data.

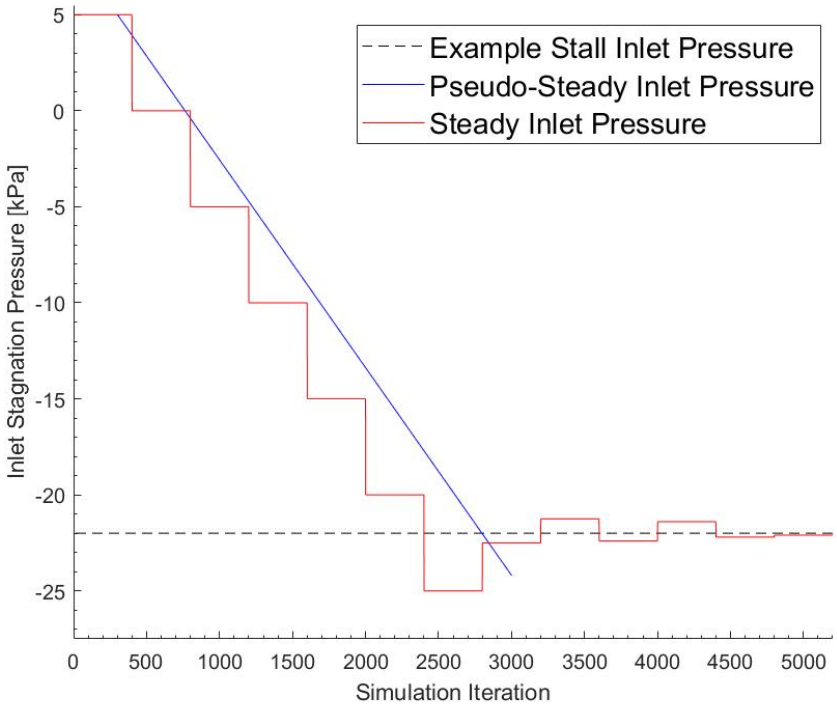


Figure 3.9. Inlet boundary condition demonstrating steady-step method and pseudo-steady method.

THIS PAGE INTENTIONALLY LEFT BLANK

CHAPTER 4:
Mesh Sensitivity Study

4.1 Objectives

The objective of the mesh sensitivity study was to reach mesh convergence at a specified test condition to validate the mesh settings before evaluation of compressor performance across the speed line. Testing of mesh convergence was conducted at the zero-back pressure case on the 70% speed line as this is the most stable condition and should provide the quickest convergence. Meshing in the gas passage was largely based on the criteria provided by Meinster [11] with modifications implemented to accommodate the addition of the casing treatment in a stationary domain. Figure 1.6 presents the mesh criteria developed by Meinster [11]. Validation of the smooth casing model was conducted to ensure a good starting position for the combined geometry.

4.2 Approach

The key features of the flow which need to be observed and resolved are the casing treatment recirculation and the blade shocks. Formation of shocks occurs primarily ahead of the blade leading edge outside of the boundary layers and in between the blades, so shock resolution is primarily influenced by the bulk mesh sizing. Bulk mesh sizing also plays a critical roll on the solver run time as it dictates the largest mesh cell size generated. Inevitably, the bulk mesh sizing is a compromise between flow resolution and the computational power available. Sizing controls were implemented to decrease cell size around the blade while the mesh size could remain coarse near the inlet and exit where flow is less critical to the study.

More challenging was the refinement of the boundary layer and the transportation of data across the domain interface into the casing treatment. The boundary layer on the blade and outer-wall were refined in accordance with the parameters defined by [11]. These settings were modified to include face sizing on the outer wall around the blade tip to improve the aspect ratio of the mesh cells. A goal of 100 was set for the cell maximum aspect ratio.

Additionally, an inflation layer was added to the domain interface to improve the transport of information from one domain to the next. To prevent a mismatch of cell sizing on either side of the domain interface, a matching face sizing was applied to the lower surface of the treatment domain. Unfortunately, ANSYS does not support a mesh matching between different domains, so the faces had to be manually matched.

Inside of the of the treatment, proximity controls were used to resolve boundary layers and refine the mesh. The use of inflation layers inside of the treatment proved to be impractical due to the complex shapes and tight geometries. Often when attempting to run models with inflation controls inside of the treatment the solver would generate negative mesh volumes terminating the run. The bulk mesh setting "points across a gap" was used which places cells strategically whenever a constraint is detected in the model. This created a fine mesh in the domain interface region which gradually grew as the treatment opened up into the passages. Several meshes were made sequentially adding in flow features during each iteration. Table 4.1 lists the controls used and is in the order which they were added to the model.

Table 4.1. Mesh features used to develop the final meshes.

Mesh Feature	**Location(s)**	**Purpose(s)**
Bulk Mesh Sizing	Gas Passage Domain Treatment Domain	Shock Resolution General Flow Resolution
Match Control	Gas Passage Periodic Boundaries Treatment Periodic Boundaries	Computational Efficiency
Points Across a Gap	Treatment Domain	Tip Gap Resolution
Curvature Control	Treatment Domain	Capture of Boundaries
Face Sizing	Blade Faces Blade LE/TE Blade Tip Hub Domain Interfaces Select Periodic Faces	Flow Resolution Aspect Ratio Control Boundary Layer Resolution Tip Gap Resolution Mesh Convergence
Inflation Control	Blade Outer Wall Domain Interfaces	Boundary Layer Resolution Boundary Layer Resolution

4.3 Results

To validate the mesh developed by Meinster [11], two further iterations of his mesh sensitivity study were conducted by refining his parameters. Table 4.2 shows the meshes presented by Meinster [11] with the final two entries being the refinement carried out here. Efficiency is much more sensitive to mesh features, so it was used as the bench mark for mesh comparison. The refinement was found to not alter the peak efficiency for either refined meshes. However, the chocked flow condition varied by less than 0.3% for mesh #7. Mesh #8 achieved convergence at the choked condition, but this regime is not of importance to the study so mesh #6 was taken as converged and used as the base line of this study.

Figure 4.1 is taken from Meinster [11] and includes the meshes analyzed here as well. Refining the mesh further than Meinster [11] caused the choked efficiency to rise, but did not effect the peak efficiency which is of more significance. The final mesh was run through a pseudo-steady simulation and intersected the choked efficiency of mesh #7 and and peak efficiency of the two prior meshes. Simulation times drastically increased for the refined meshes, so mesh #6 was used as the baseline mesh since the peak efficiency aligned with the refined meshes.

Table 4.2. Mesh refinement of standard rotor-only gas passage. Adapted from Meinster [11].

Mesh	Nodes	Elements	Blade Average y^+
1	1,173,670	3,595,317	208.40
2	3,977,379	10,113,366	4,975
3	3,735,985	8,299,061	8.374
4	3,800,067	8,618,960	2.891
5	6,785,278	16,529,255	0.0515
6	10,079,681	23,079,899	0.772
7	**11,895,234**	**31,478,693**	**0.874**
8	**13,857,291**	**33,370,058**	**5.554**

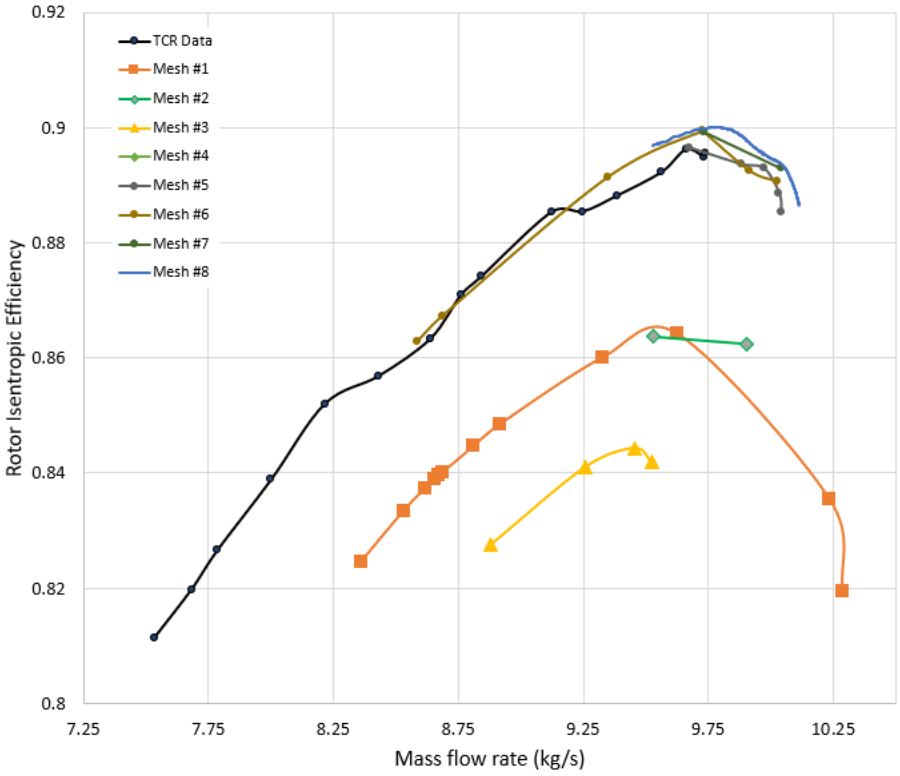


Figure 4.1. Efficiency maps from smooth casing mesh analysis. Adapted from Meinster [11].

After confirming the settings and results of the mesh sensitivity study done by Meinster [11], fewer iterations were necessary in the mesh sensitivity study for the casing treatment models. With the established mesh settings for the gas passage, the casing treatments were added and mesh per the priorities listed in Table 4.1. Four meshes were generated and run to convergence at 70% speed at zero relative inlet-stagnation pressure.

Mesh convergence was determined from two separate convergence histories. The typical momentum and continuity residuals output by the solver were the first metric of convergence. Root mean square (RMS) was chosen as the preferable error measurement as the simulation was observed to display some variance as convergence was reached; a goal of reaching an error of 10^{-5} was set. As the residuals in such a complex flow field tend to not be a clean signal, a second metric was used to confirm solution convergence. Monitor points were placed on the inlet and outlet of the gas passage to measure the mass flow. These results were plotted continuously throughout the simulation. Once inlet and outlet mass flows reached a

steady-state and were equal, the solution was determined to be converged. This technique was especially useful in near-stall conditions. As the flow approaches an unsteady-state, the RMS residuals tend to not converge nearly as well, but the solution can be said to have converged if the mass flows are equal and steady. Simulations were allowed to run until both metrics were met or convergence of mass occurred and the RMS residuals reach an approximately steady-state. Figures 4.2 and 4.3 demonstrate this approach on a full speed line conducted later in the study. The figures depict the RMS continuity residuals and mass flows as the inlet pressure is steadily depressed. A spike in the RMS residuals and a sudden drop in mass flow can be seen where the inlet pressure was depressed. As the pressure was depressed, the flow became more difficult to resolve, resulting in the poorer RMS residuals observed on the right; the scaling is also compressed to show multiple iterations resulting in more dense noise signals. This approach had the added benefit of providing better starting conditions for the higher performance data points.

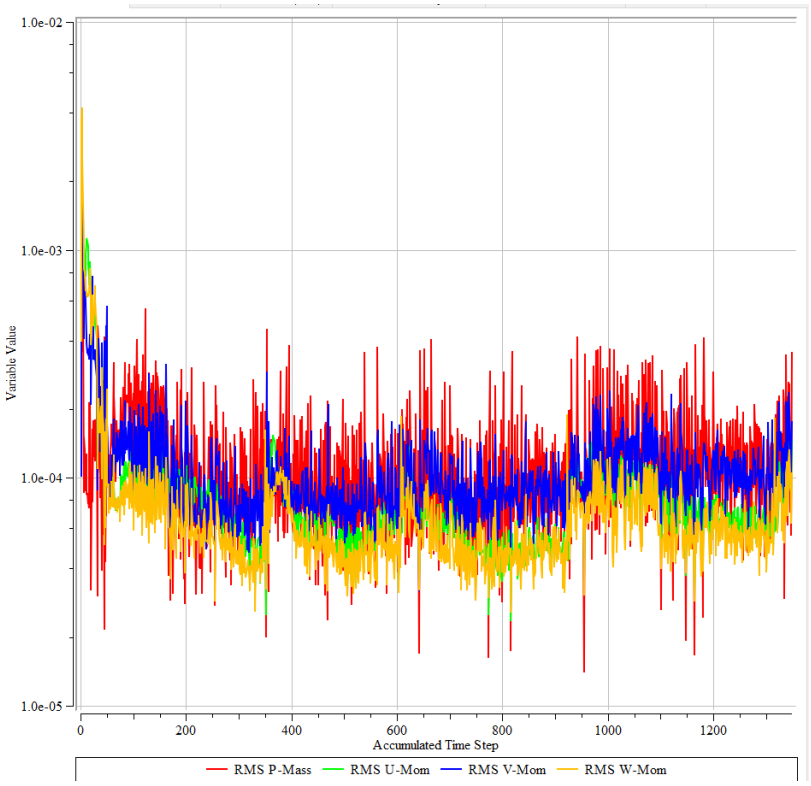


Figure 4.2. RMS Residuals for a speed line evaluation.

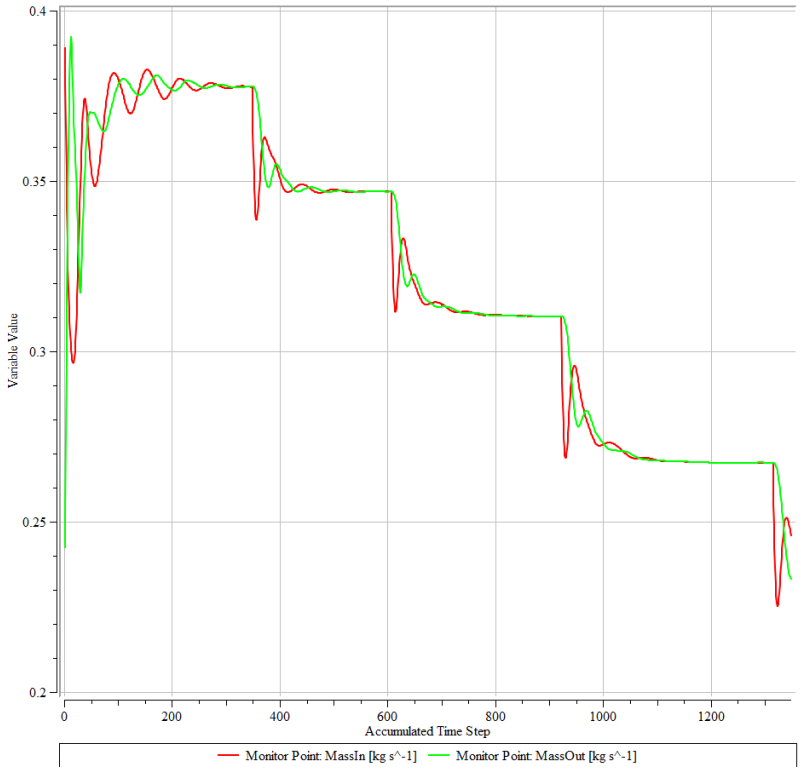


Figure 4.3. Mass Flow for a steady speed line evaluation.

The results of the evaluated meshes are displayed in Table 4.3. Each solution was run until a steady-state RMS value was achieved and the mass flows agreed. Mass flow and pressure ratios were used as the initial means of simulation convergence. As can be seen from Table 4.3, mass flow rate and pressure ratios did not vary much between mesh #2 and #3. However, the blade y^+ value explains why the further refinement was necessary. In mesh #2 the bulk sizing, capture curvature, points across a mesh, and many of the face sizing had been applied. This greatly increased the cell count from mesh #1 and caused a significantly better general mesh which accounts for the 2 kg/s change in mass flow rate, but it does not include any inflation layer controls. The lack of boundary layer controls can be seen in the average aspect ratio. Without the incredibly fine cells introduced by the inflation layers, the bulk mesh controls and face sizings ensure a fairly uniform mesh at the expense of a high y^+ value. In order to refine the boundary layer on the outer wall, the domain interface, and the blade, inflation controls were added. Figure 4.4 shows the inflation controls used in mesh #3. Adding these inflation layer controls added nearly 10 million elements to the mesh. This

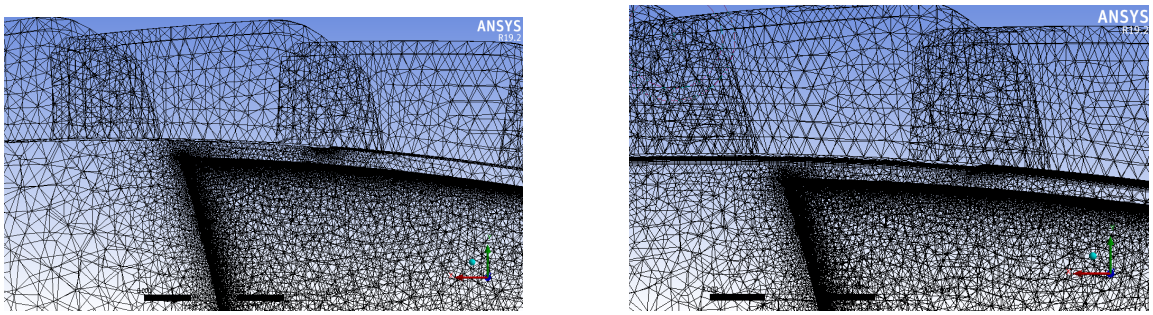
did not dramatically change the macroscopic results seen in Table 4.3, but it will play a massive part in the exploration of casing treatment interactions with the blade tip. Figure 4.5 displays the mesh before and after refinement of the blade tip.

Table 4.3. Overview of meshes used for sensitivity study.

Mesh	**Nodes**	**Elements**	**Residual**	**Blade y^+**	**AR**	**Mass Flow** $[\frac{kg}{s}]$	π_t
1	2,738,922	7,840,323	1E-3	61.63	49.48	9.634	1.360
2	3,093,823	16,809,739	1E-7	22.23	1.86	7.494	1.219
3	11,180,465	28,340,490	1E-5	0.88	27.13	7.553	1.223
4	11,994,940	29,074,381	1E-4	0.79	28.35	7.541	1.225

Details of "Inflation" - Inflation	
Scope	
Scoping Method	Geometry Selection
Geometry	1 Body
Definition	
Suppressed	No
Boundary Scoping Method	Named Selections
Boundary	Multiple Entities
Inflation Option	First Layer Thickness
First Layer Height	1.e-003 mm
Maximum Layers	23
Growth Rate	1.2
Inflation Algorithm	Pre

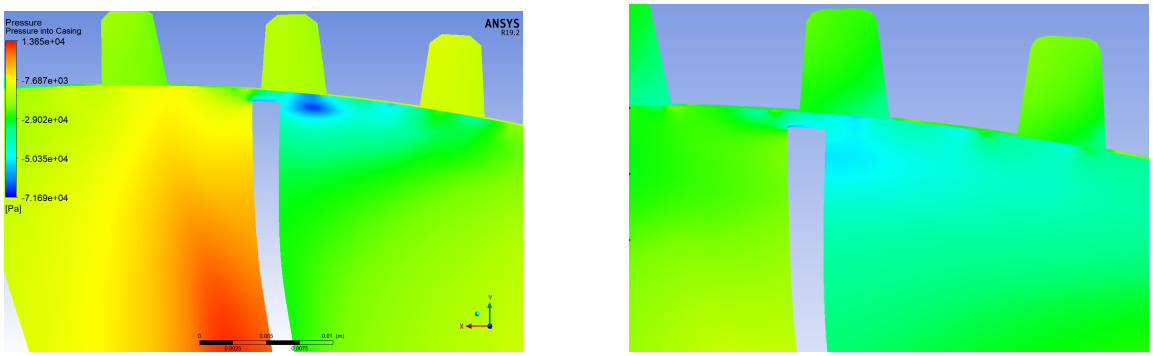
Figure 4.4. Inflation controls used to resolve boundary layers.



(a) Coarse blade tip mesh (b) Refined blade tip mesh

Figure 4.5. Comparison of a coarse and a refined blade tip mesh.

To evaluate the effectiveness of the mesh refinement around the blade tip and into the treatment domain, the pressure gradient from into the treatment was evaluated. While the pressure will change as it approaches the wall and interacts with the treatments, the change should follow a relatively smooth transition. Any pressure discontinuities into the treatment domain would indicate an inefficient transfer of information from the primary domain into the treatment. A plane which displays local pressure was place at the midpoint of the casing treatment domain. Figure 4.6a shows the pressure in the medium mesh and Figure 4.6b shows the pressure in the fine mesh. In the medium mesh, it is apparent where the casing treatment domain begins. Data is transferred into the casing treatment, but in such a poor manner that a discontinuity in the solution occurs. Pressure transfer into the domain of the final mesh displayed a much smoother transition validating the results in the tip gap region.



(a) Pressure Transfer for Coarse Mesh (b) Pressure Transfer for Refined Mesh

Figure 4.6. Comparison of pressure transfer for a coarse and a refined blade tip mesh.

The final mesh settings yielded a hybrid mesh composed of over 28 million elements. Blade y^+ values and aspect ratios were within the accepted limits and the flow demonstrated good resolution around the blade tip. Even in the final mesh, compromises were made. Convergence in the mid-grade mesh reached better RMS continuity convergence, but did not have the detail required for this study. Table 4.4 presents the statistics of the the meshes generated for both casing treatments and Figures 4.7 and 4.8 show the final meshes. Details of both meshes can be found in Appendix B.1 and B.2.

Table 4.4. Overview of meshes used for experimentation.

Mesh	**Nodes**	**Elements**	**Blade y^+**	**Aspect Ratio**	**Orthogonality**
S-Shaped Grooves	11,180,465	28,340,490	0.88	27.13	0.74654
Internal Passages	10,167,000	34,482,633	0.64	57.99	0.76282

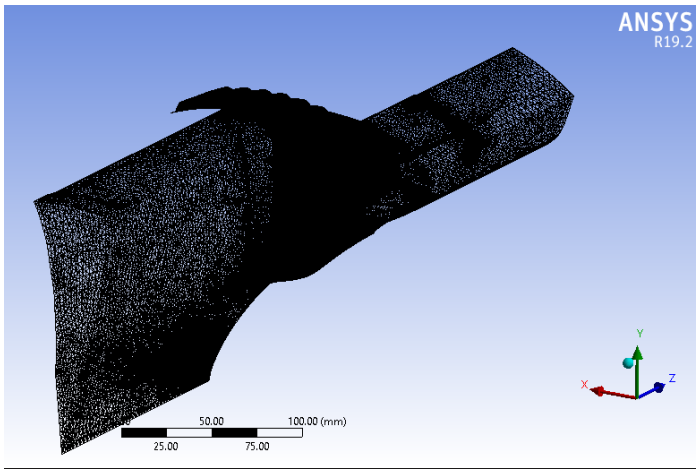


Figure 4.7. The final mesh for the s-shaped axial groove case.

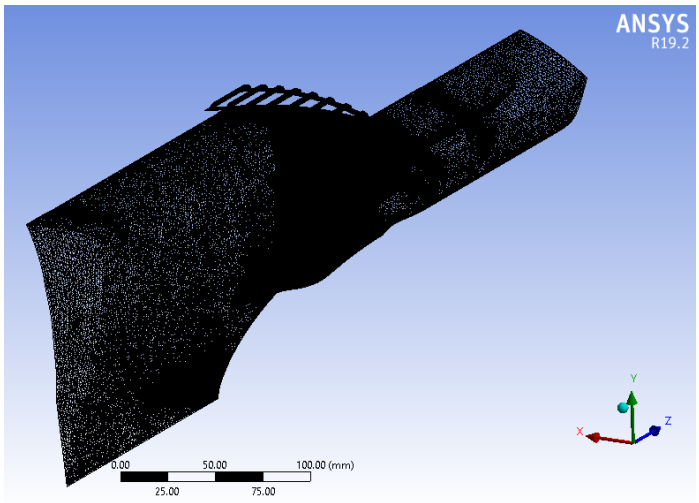


Figure 4.8. The final mesh for the internal passages casing treatment.

CHAPTER 5:
Results

5.1 Experimental

The NPSMF was tested alone in the TCR as part of the work by Meinster [11]; this study sought to expand that work to include the full compressor stage with IGVs and advanced casing treatment. As part of the work up to the final series of tests, the TCR was tested in the rotor-stator configuration (RS or full stage), the IGV-rotor-stator (IRS) configuration with smooth endwall, and finally in the IRS configuration with s-shaped axial grooves installed. Results from each of these tests are presented in order to give a complete picture of the final performance.

Tests in all configurations were conducted at 70%, 80%, 85%, and 90% of the designed operating speed of 30,000 rpm. The TCR is power limited and unable to reach 100% design speed. Comparison of the operating configurations was done with total-to-total pressure ratios (referred to as pressure ratio), mass-averaged efficiency, and stall margin as defined in the work of McNab [3]. Figure 5.1 provides an overview of the performance curves for all configurations and speeds tested, and Figure 5.2 displays all the efficiency curves measured. The following sections further interrogates this data.

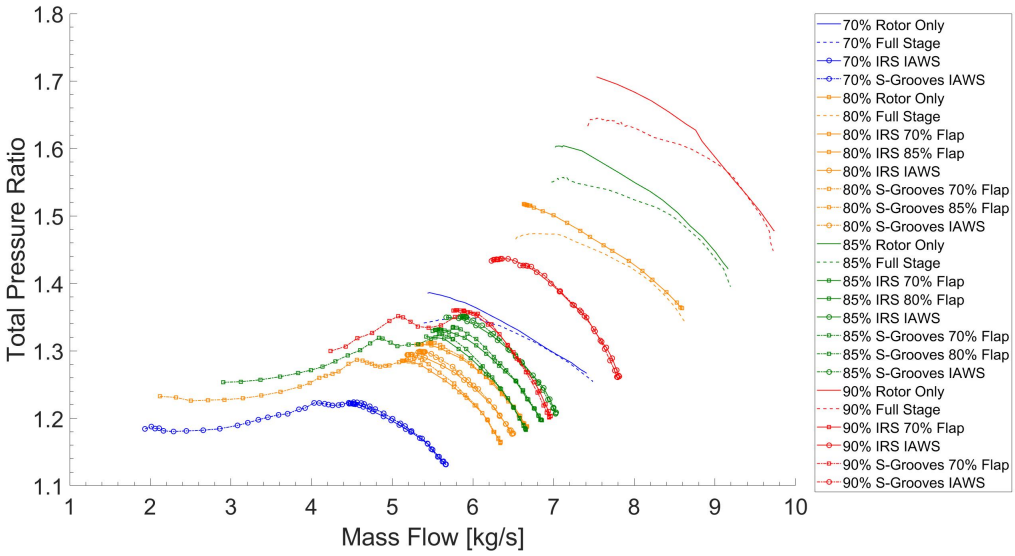


Figure 5.1. The performance curves for all configurations and speed lines tested with the TCR.

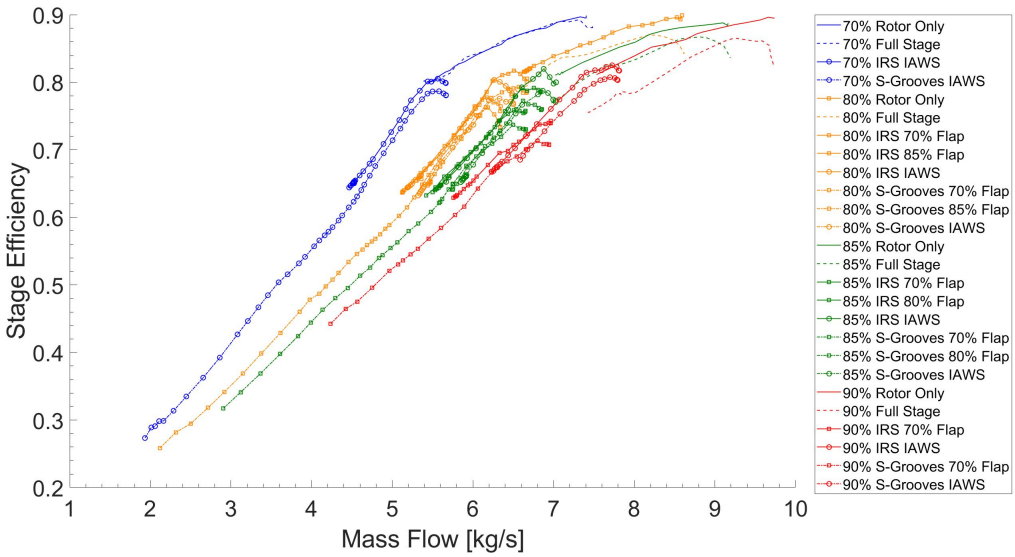


Figure 5.2. The efficiency curves for all configurations and speed lines tested with the TCR.

5.1.1 Full Stage Configuration

The total pressure ratio for the four speed lines in the full and half stage configurations is seen in Figure 5.3. Stator performance at the open throttle position is similar to the rotor only performance. Similar mass flow rates and total pressure ratios are generated. As the pressure ratio is increased via throttling, the total pressure losses from the stator increase resulting in lower total pressure ratios in the full stage. The mass flow operating range increases slightly with the addition of the stator. Table 5.1 presents the total pressure losses and the operating range increase.

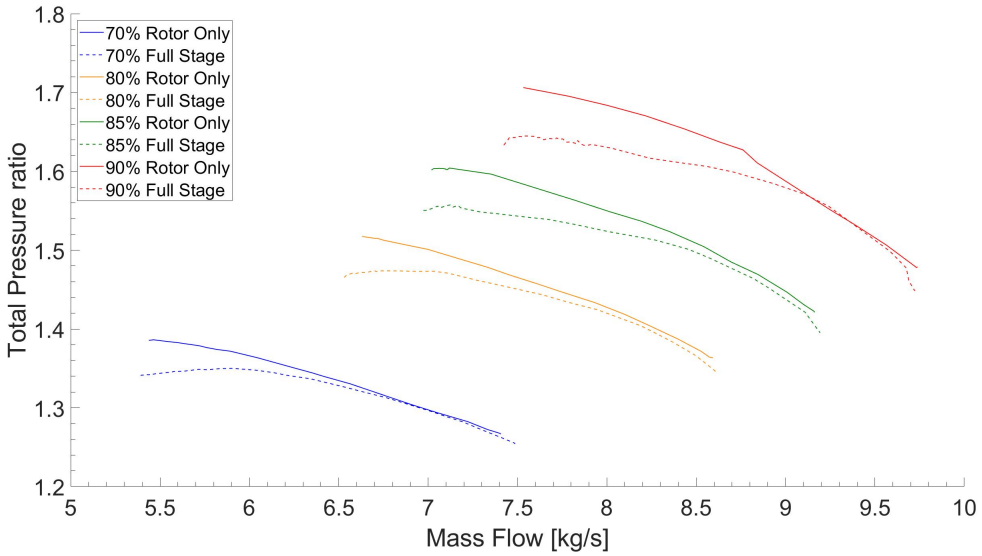


Figure 5.3. Comparison of rotor and rotor-stator configuration performance curves for all speed lines.

Table 5.1. Total pressure losses and mass flow range increase from the stator.

Speed	Peak Total Pressure Losses [%]	Mass Flow Range Increase [%]
70%	2.618	6.386
80%	2.8733	6.408
85%	2.9236	3.549
90%	3.5984	4.371

Figure 5.4 presents the stage efficiency against the rotor only configuration. The stator impacts the efficiency the most at the higher operating conditions. At the 70% operating condition, the efficiency loss is minimal and the peak efficiency point remains nearly constant. However, as the rotor goes transonic, the effects of the stator can be seen. In the rotor only configuration, the peak efficiency occurs in the open throttle or max mass flow condition. However, the stator drives the peak efficiency down the performance curve as the rotor-stator configuration reaches a chocked condition with the throttle fully opened. Driving the peak efficiency to a lower mass flow rate decreases the stall margin in the rotor-stator configuration. Additionally, the efficiency across the operating range is reduced. Table 5.2 summarizes the efficiency losses and the subsequent decrease in the stall margin for the stator. This feeds into the purpose of the stator. The stator is able to reduce the mass flow rate of the stage at peak efficiency. Reduction in mass flow rate and the flow straightening will decrease the axial velocity in later stages of the production compressor helping to keep both the compressor and the later stages within their respective operating ranges.

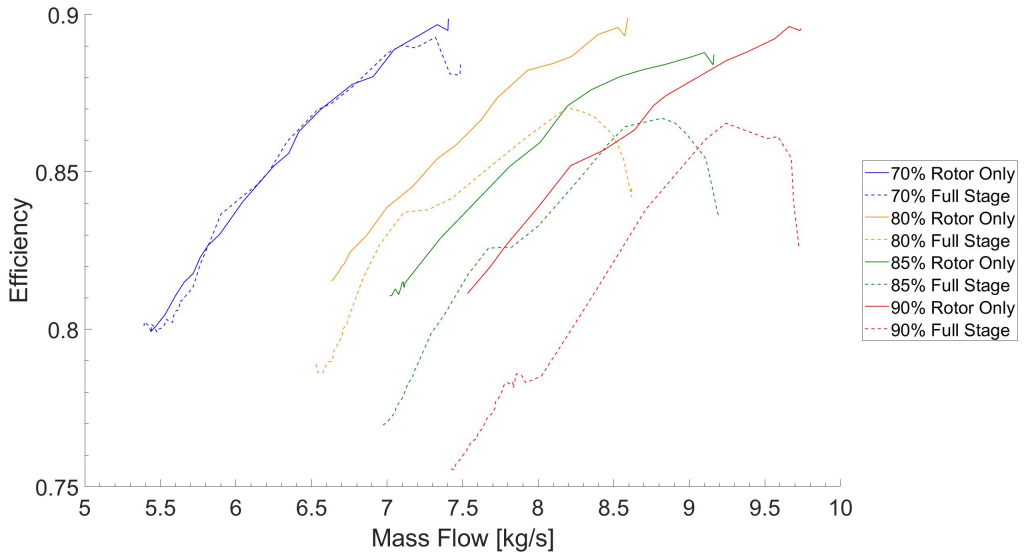


Figure 5.4. Comparison of rotor and rotor-stator efficiency curves for all speed lines.

Table 5.2. Efficiency losses and stall margin decreases from the stator

Speed	Percent Efficiency Loss	Percent Stall Margin Decrease
70%	0.585	0.916
80%	2.849	11.24
85%	2.086	8.495
90%	3.074	10.63

5.1.2 Full Stage with Inlet Guide Vanes

After characterization of the TCR with the rotor and stator installed, the inlet guide vanes (IGVs) were installed and tested. Figure 5.5 presents a comparison of all three smooth endwall configurations. As would be expected, the mass flow rates and pressure ratios are reduced with the addition of the IGVs. This reduction of mass flow serves to reduce the velocity through the entire compressor keeping the aft compressor stages within their operating range while preventing the first stage from stalling. Table 5.3 demonstrates the reduction in the mass flow at stall across the three standard configurations. As the IGVs are designed to reduce mass flow, their effect is significantly larger than the effect of the stator. A comparison of the pressure ratio and mass flow rate at stall for the IGVs against the stator only is compiled in Table 5.4. The IGVs lower both the pressure ratio and the mass flow rate, but have a greater effect on the mass flow into the compressor. Using a percent difference comparison shows the mass flow rate is reduced scaled to the power line via the schedule used.

Table 5.3. Mass flow rate [kg/s] at stall for half-stage, full-stage, and IRS IAWS configurations.

Speed	Half-Stage	Full-Stage	IRS IAWS
70%	5.43	5.39	4.47
80%	6.63	6.53	5.19
85%	7.02	6.97	5.67
90%	7.53	7.42	6.23

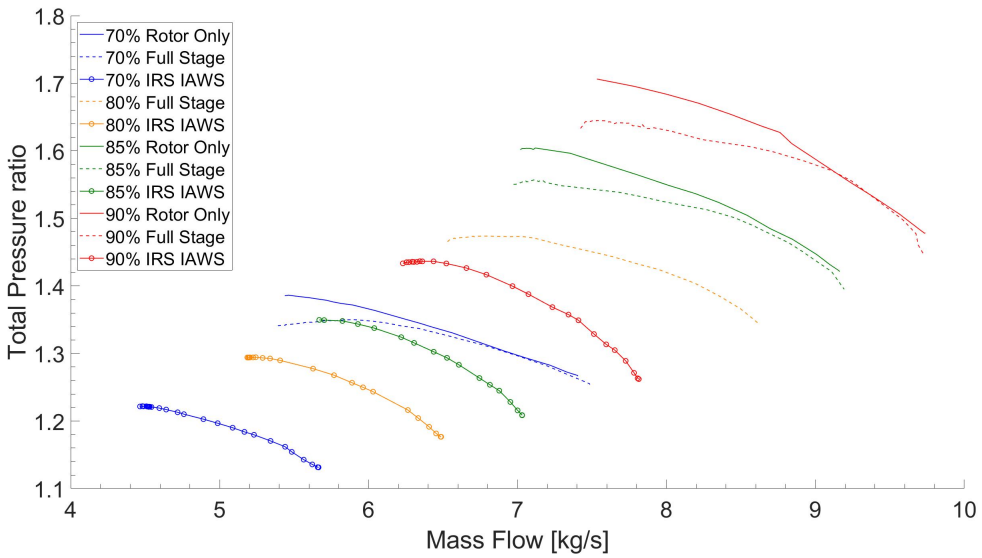


Figure 5.5. Comparison of TCR performance in the rotor, full stage, and IRS configurations.

Table 5.4. Percent reduction in mass flow and pressure ratio with IGV IAWS.

Speed	$\Delta\pi_{tot}$ [%]	ΔSM [%]
70%	12.23	17.68
80%	14.84	21.72
85%	15.64	19.23
90%	15.99	17.26

The IGVs were added and tested with the full stage and smooth endwall in accordance with the provided schedule, but after collecting preliminary results the TCR was tested with different flap angles to test sensitivity to the flap angle. Figure 5.6 presents a comparison of the IRS and full stage data for all the flap angles tested. Not all flap angles were tested in every configuration. It was found that an increased flap angle (ie setting for lower power line) reduced the performance of the stage while simultaneously reducing the mass flow through the stage. At the 80% speed line, a shallower angle was applied (the 85% flap angle) in order to confirm sensitivity to the flap angle. Between the 80% and 85% speed lines the performance reduction was slight with the increased flap angle, but the 90% line

was extremely sensitive to the flap angle adjustment.

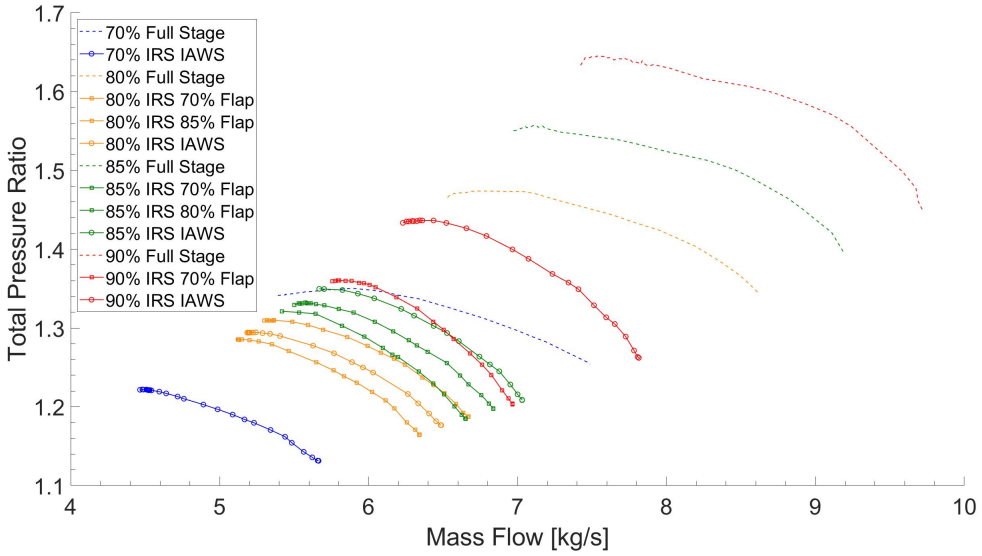


Figure 5.6. Comparison of rotor-stator and IRS performance curves for all speed lines and all IGV angles.

In Figure 5.7 the efficiency curves for the rotor, full-stage, and IRS set IAWS are shown. Results are as expected from the performance curve. The stator does reduce efficiency (especially at higher power lines) but the IGV reduces the efficiency and the peak efficiency mass flow greatly. Table 5.5 presents the peak efficiency and the associated mass flow rate for the IRS IAWS and the full-stage for each power line. At the 90% speed line, the efficiency of the stage is reduced by 4.1% due to the IGVs while the mass flow is reduced by 1.523 kg/s (16.5%). The stall margin is reduced by 0.32% by the addition of the IGVs. At the peak performance line, the IGVs reduce the mass flow significantly.

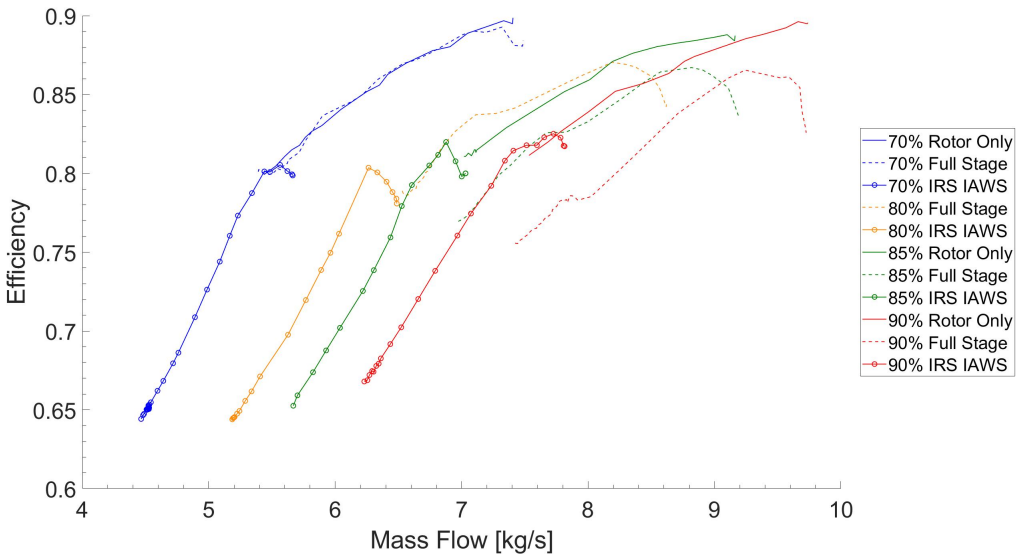


Figure 5.7. Comparison of TCR performance in the rotor, full stage, and IRS configurations.

Table 5.5. Comparison of efficiency, mass flow at peak efficiency [kg/s], and stall margin for the full-stage and IRS set IAWS.

Speed	$\eta_{max,stage}$	$\eta_{max,IRS}$	$\dot{m}_{stage}$	$\dot{m}_{IRS}$	SM_{stage}	SM_{IRS}
70%	0.893	0.805	7.320	5.564	26.34	19.75
80%	0.870	0.804	8.191	6.264	20.28	17.21
85%	0.867	0.820	8.819	6.877	20.93	17.57
90%	0.866	0.825	9.251	7.7264	19.69	19.37

At the max operating power, the IGV set angle plays a significant role on the efficiency of the stage. Figure 5.8 presents the efficiencies of each IGV set angle used with the full stage for comparison. The IGV set angle does not effect the slope of the efficiency mass curve, but it effects the max efficiency reached. Less whirl allows the compressor to operate at a higher efficiency (with the extreme case being no whirl – the full stage configuration). This is best seen in the 80% data in orange. For the 80% case, the IGV angles were set greater to, less than, and equal with the schedule value. Setting less than schedule (the 85% power angle) allowed a higher efficiency while the greater whirl reduced the efficiency. In the 90% case, the 70% power line flap angle greatly reduced the efficiency and the mass flow at the

peak efficiency point. Table 5.6 presents the mass flows and efficiency at the peak efficiency operating point for the 90% speed line. The sudden drop in efficiency is directly linked to the significant decrease in relative tip velocity caused by the increased whirl.

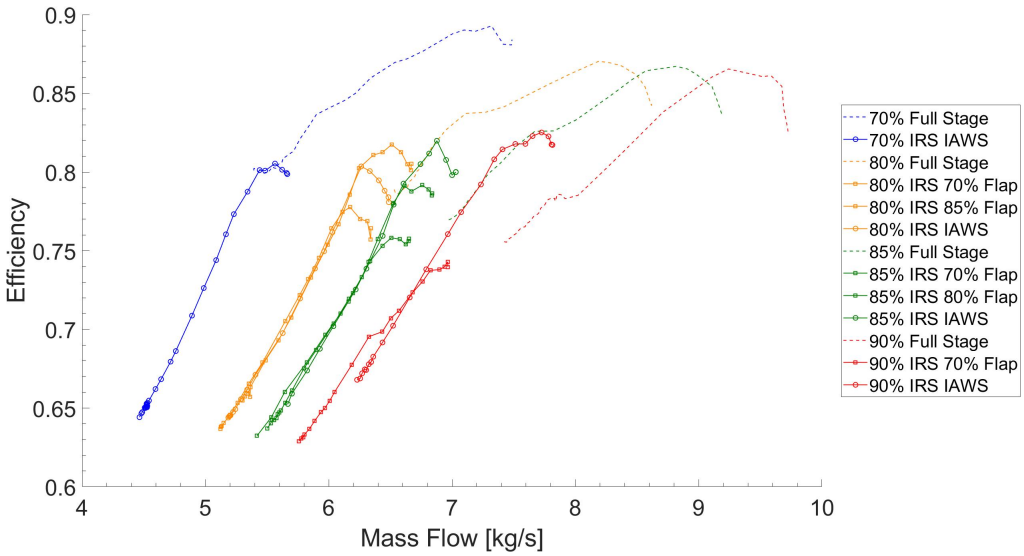


Figure 5.8. Comparison of rotor-stator and IRS efficiency curves for all speed lines and all IGV angles.

Table 5.6. Efficiency and mass flow of TCR at 90% speed and varying IGV angles.

Configuration	Peak Efficiency	Mass Flow Rate [kg/s]
Stage Only	0.866	9.243
IGV IAWS	0.825	7.726
IGV 70% sched	0.743	5.757

5.1.3 S-Shaped Axial Groove Casing Treatments

The s-shaped axial grooves (s-grooves) were tested in only the IRS configuration across all IGV blade angle set points. The grooves were highly successful at extending the stall margin of the compressor stage but are highly dependent on the IGV blade angle. Figure 5.9 shows the performance curves for all the tests conducted with the IGV's comparing the smooth endwall with the s-grooves. Only four data points exhibit the increased stall margin;

at 70% schedule flap angle all four test conditions demonstrated increased stall margin. At the other flap angles tested, the s-grooves actually decreased the stall margin. Table 5.7 lists the results of the stall margin changes.

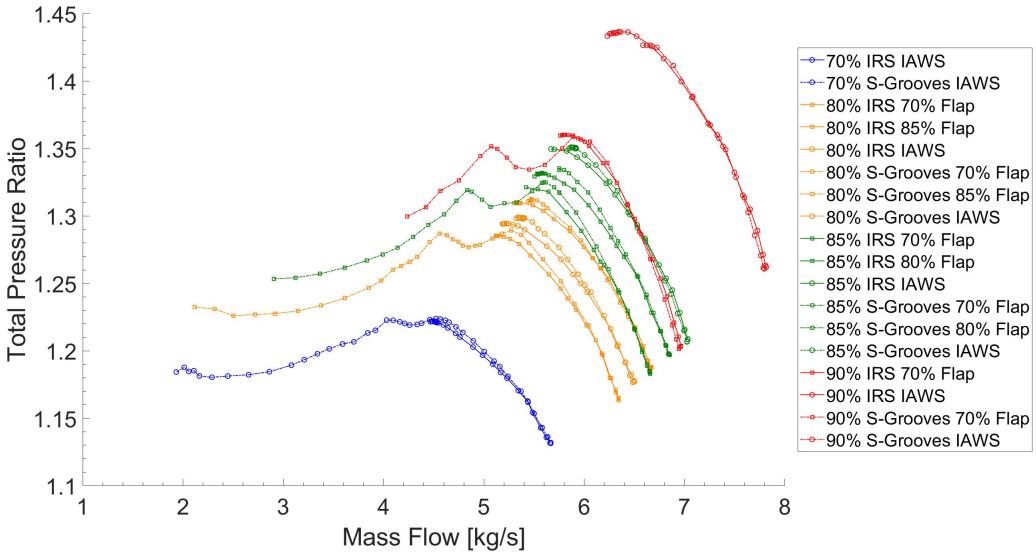


Figure 5.9. Performance of smooth endwall and s-shaped axial grooves for all IGV angles and power lines.

Table 5.7. Summary of stall margin change with s-shaped axial grooves installed.

Power	Flap Setting	ΔSM [%]
70%	70%	230.88
80%	70%	286.03
	80%	-7.795
	85%	-7.471
85%	70%	230.33
	80%	-29.189
	85%	-15.742
90%	70%	117.57
	90%	-25.250

Using the provided IGV blade set angle, the s-grooves did not improve the stage stall margin, except at the 70% power line. Figure 5.10 shows the performance curves with the IGV set IAWS. The s-grooves did actually improve the pressure ratio seen except at the 90% line. Theses pressure ratio increases were generally minor, but at the 90% IAWS test point, the peak pressure ratio dropped by 0.7%. Table 5.8 presents the pressure ratio changes as well as the stall margin changes.

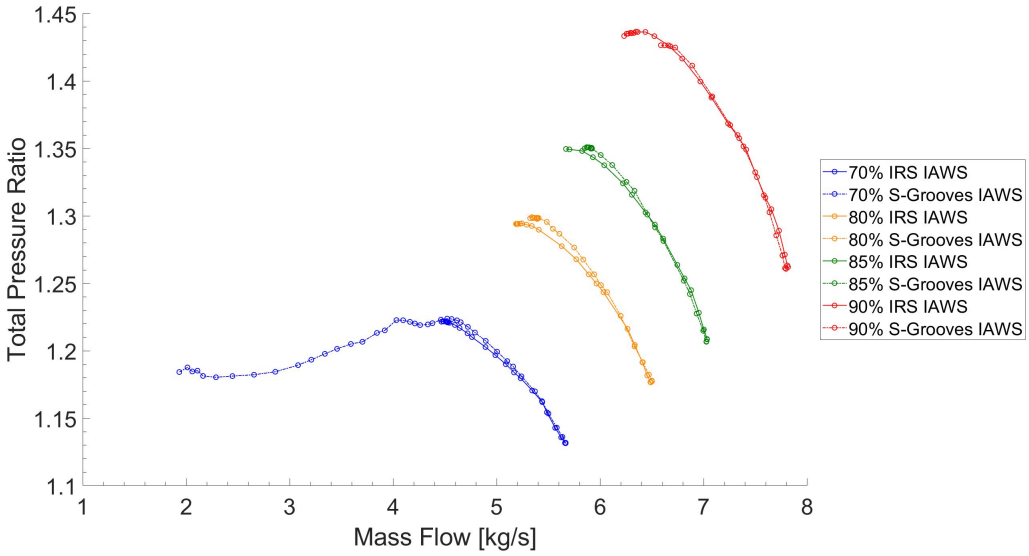


Figure 5.10. Smooth endwall and s-shaped axial grooves with IGV set IAWS.

Table 5.8. Summary of stall margin and peak pressure ratio change with s-shaped axial grooves installed with IGV set IAWS.

Power	$\Delta\pi_{tot}$ [%]	ΔSM [%]
70%	0.155	230.88
80%	0.355	-7.471
85%	0.096	-15.742
90%	-0.6961	-25.25

Due to the lack of performance at the scheduled angles, multiple other IGV angles were tested for the 80%, 85%, and 90% performance lines. It was found the 70% flap angle was the only angle which improved the stall margin. Figure 5.11 displays the performance curves

with the IGV set at the 70% configuration. The performance curves presented diverge from expected transonic compressor curves and take the form of subsonic compressor curves. This shows the power of the IGVs to reduce mass flow and confirms the subsonic origins of this endwall treatment. None of these cases were able to be driven to a traditional stall. All cases with extended stall margin were terminated due to TCR operating limitations. The inlet bellmouth is not calibrated for the low mass flow rates seen (as they were not anticipated for the current compressor operation) and the length of the tests caused increased heating in the endwall. These cases displayed an audibly unsteady behavior, but did not show any hysteresis. All four test speeds displayed massive increases in the stall margin. Table 5.9 lists the pressure ratio changes and the stall margin increase for each power line.

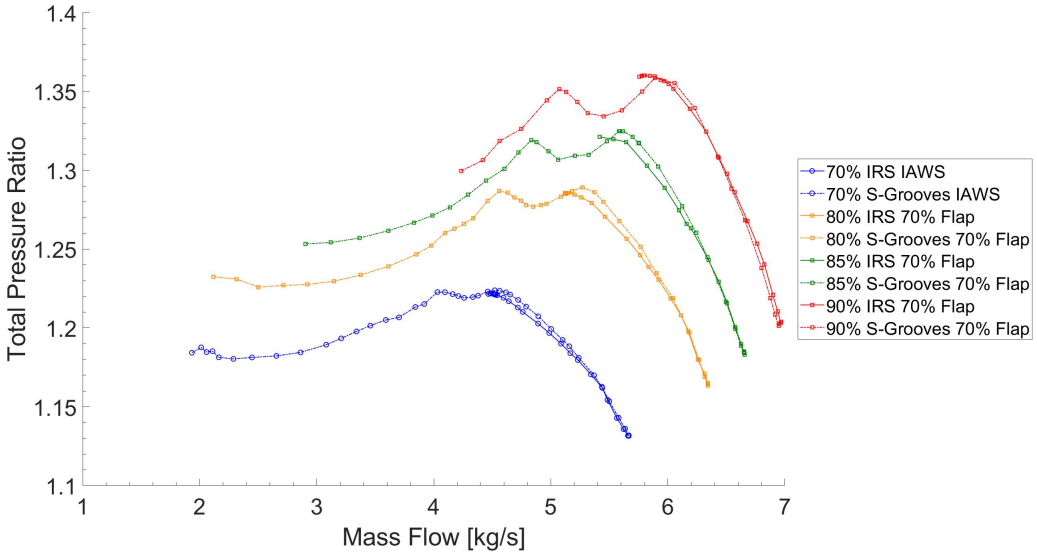


Figure 5.11. Smooth endwall and s-shaped axial grooves with IGV set at 70% scheduling.

Table 5.9. Summary of stall margin and peak pressure ratio change with s-shaped axial grooves installed with IGV set at 70% scheduling.

Power	$\Delta\pi_t$ [%]	ΔSM [%]
70%	0.155	230.88
80%	0.296	286.03
85%	0.280	230.34
90%	-0.110	117.57

The efficiency did drop in all cases with the casing treatment installed. Significant efficiency losses were experienced. At the maximum operating power, losses of 4% were recorded for peak efficiency and efficiencies less than 30% were observed at the extreme lower end of the mass flow rate. The efficiency lines are shown in Figure 5.12. A summary of efficiency losses is presented in Table 5.10

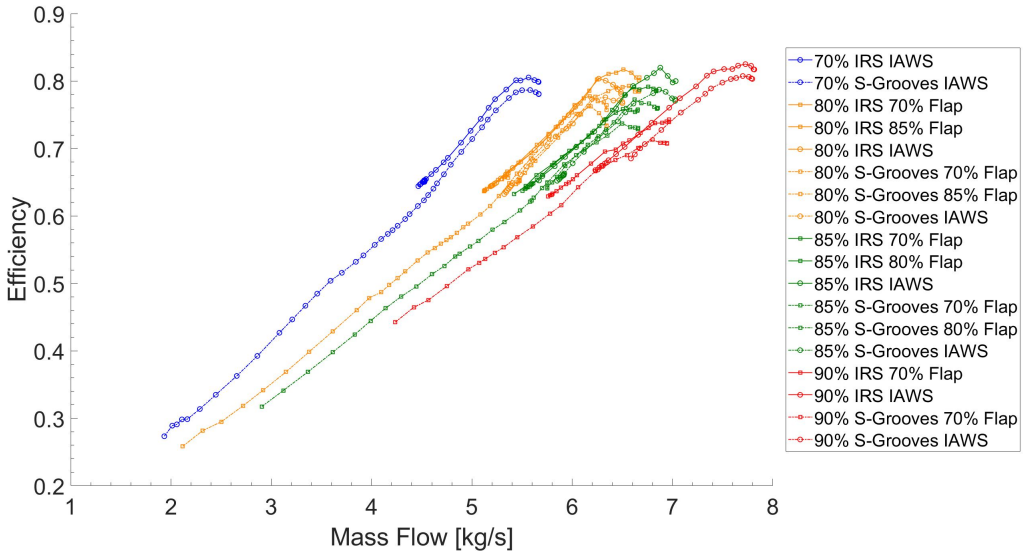


Figure 5.12. Efficiency for smooth endwalls and s-shaped axial grooves for all IGV angles and power lines.

Table 5.10. Summary of efficiency changes with s-shaped axial grooves installed.

Power	Flap Setting	$\Delta\eta_{TT}$ [%]
70%	70%	-2.318
80%	70%	-1.962
	80%	-3.046
	85%	-3.442
85%	70%	-2.771
	80%	-2.366
	85%	-3.962
90%	70%	-4.015
	90%	-2.138

5.2 Computational

5.2.1 Pseudo-Steady Compressor Operation

The pseudo-steady approach described in Section 3.2.4 was used for all power line simulations. A 90% smooth casing simulation was conducted using the traditional steady-state method for comparison and validation purposes. Validation of the approach was conducted through continuity tracking throughout the simulations and a hysteresis examination on a 90% power simulation.

Mass flow was monitored at the inlet and exit of the blade gas passage. This allowed convergence to be continually monitored. The difference between exit and inlet flow was calculated and normalized based off of the inlet mass flow. For a steady system the inlet and exit mass flow should be equal and constant; however, due to the pseudo-steady nature of these simulations, some error exits. Figure 5.13 shows the mass error for an axial groove and an internal passage casing treatment simulations. Once the simulation stalled, the mass flow agreement diverged; the increased stability of the internal passages can be seen from the figure and is discussed later.

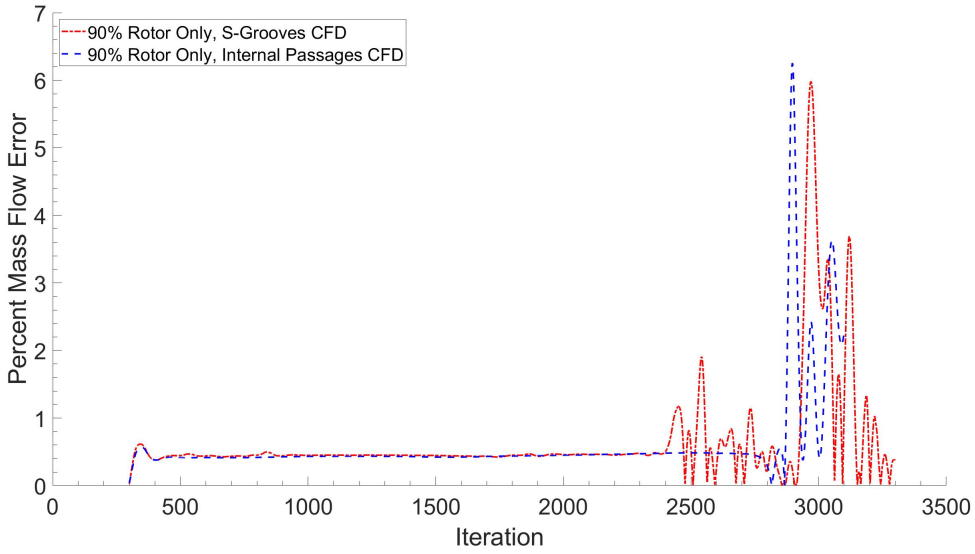


Figure 5.13. Mass flow error in the pseudo-steady simulation.

In Figure 5.13, an initial spike in the residuals is observed at 300 iterations because this is where the simulation is first taken from steady-state (with zero error) to a pseudo-steady

simulation. Each model then reaches a steady error value over the bulk of the power line. Due to the recirculation inherent with the s-grooves, the error tends to be greater than the internal passage. The overall steadiness of the flow can be determined from the mass error. In the last few hundred iterations, the flow enters a region of deep stall as can be seen in Figure 5.14 which leads to the highly unsteady flow seen by the large spikes in the mass convergence. A region of unsteady flow begins before this deep stall condition as the compressor approaches stall. This regime effects the casing treatment simulations more than the smooth casings. The flow recirculation generated by the grooves is inherently unstable and results in earlier unsteadiness compared to the discrete passages. However, the compressor is able to operate in the initial unsteadiness formed by the casing. The s-groove condition stalls within this unsteady regime.

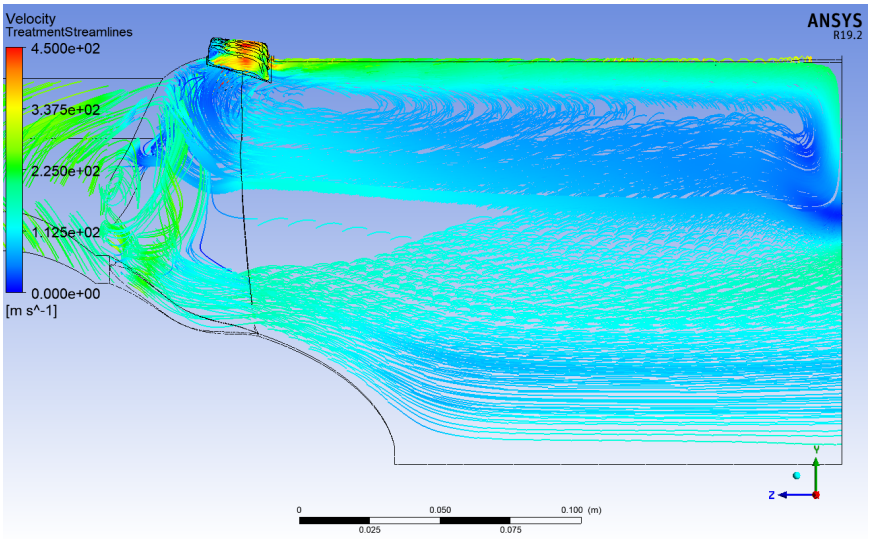


Figure 5.14. Velocity streamlines of a simulation in a deep stall at 90% power in the IR configuration with s-groove casing treatment.

The hysteresis study was conducted on the 90% power line due to pre-existing CFX data taken using the fully steady approach. Additionally, the 90% power lines represents the most unsteady, but useful conditions. Full pseudo-steady simulations were conducted at 90% for the smooth and s-shaped axial grooves and a reverse partial power line was conducted with the s-shaped axial grooves installed. Figure 5.15 compares the steady and pseudo-steady models with experimental results. On top of showing agreement between all three, this figure shows the mass flow difference in the numerical and experimental stalls. Figure 5.16

presents two 90% power lines with the s-grooves installed. The short, blue line is from the same model, but it was started at a reduced mass flow rate then the inlet stagnation pressure was raised to drive it toward an open throttle condition. This was done to examine the pseudo-steady operation for hysteresis. Both the normal and the reverse power line followed the same curve, providing another layer of validation for the approach.

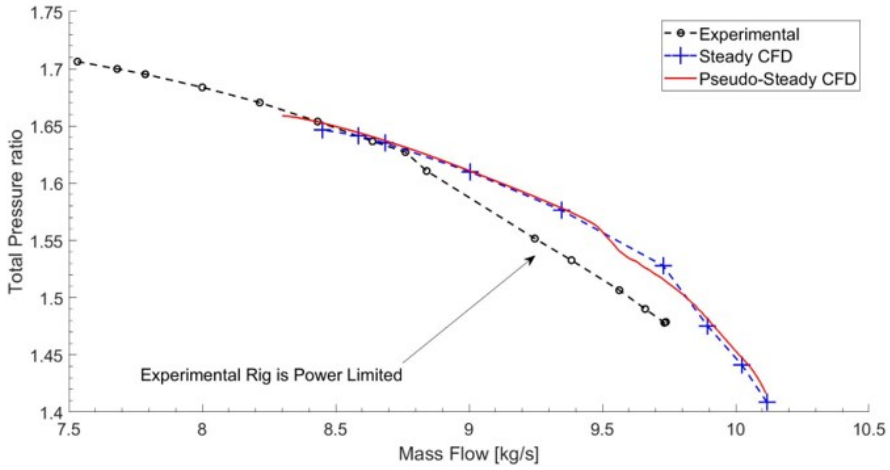


Figure 5.15. Comparison of steady and pseudo-steady data at 90% speed.

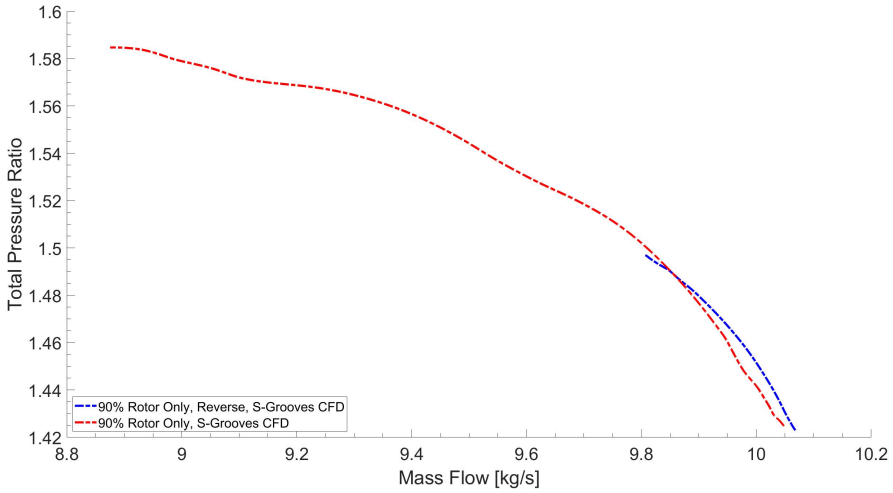


Figure 5.16. 90% CFD power line validation.

The 90% pseudo-steady line follows the steady data points and is able to flesh out the compressor behavior in between the steady data points. As was seen with the TCR data,

the s-shaped groove treatment caused an earlier onset of stall, but importantly, a CFD run conducted starting at the center point of the 90% performance curve and run to choked flow followed the full-power curve.

Stall was determined with the mass averaged compressor efficiency. In the data from the TCR, the stage efficiency follows a linear decrease after the peak efficiency point, regardless of the treatment or whirl value. Figures 5.8 and 5.12 demonstrate this trend. During TCR operation, the compressor was never driven past stall, so all data cuts off at the first indication of stall and no data exists on compressor behavior past stall. (The 70% flap cases are a slight exception as unsteadiness was driven through to achieve the stall margin increases; but even these cases exhibited a linear decrease in efficiency). The CFX simulations did not have such limitations (though unsteady data is unreliable) and data extends past stall. Stall was determined numerically as the point at which the decrease in efficiency with respect to mass flow diverged from a linear decrease. Validation was conducted visually to ensure results past the numerically determined stall point were indeed stalled. Figure 5.17 presents the raw CFX data for the smooth casing treatment cases, and Figure 5.18 shows the same data after truncation at stall. Unless otherwise noted, CFD data labeled as "IGV-Rotor" is based off the 70% power IGV schedule. The CFD power lines are continuous data lines, so to avoid confusion only the final data point (stall point) is marked to signify the whirl present. Circles represent 70% IGV setting and squares represent the 60% whirl case.

As can be seen from Figure 5.17, the severity of the stall varies, so the slope change for the efficiency curves varies greatly. In many of the CFD simulations, a pronounced "hook" shape can be seen and the curve takes a nearly vertical slope at the peak mass flow. This is due to increasing the inlet stagnation pressure above ambient in the simulation to ensure a thorough capture of the choked condition and peak efficiency. This preliminary look at post-stall operation of the compressor could be useful for improving compressor control and recovery from the stalled state. While it is only a steady simulation, it does provide some indication of performance after stall which the TCR cannot capture due to structural limitations.

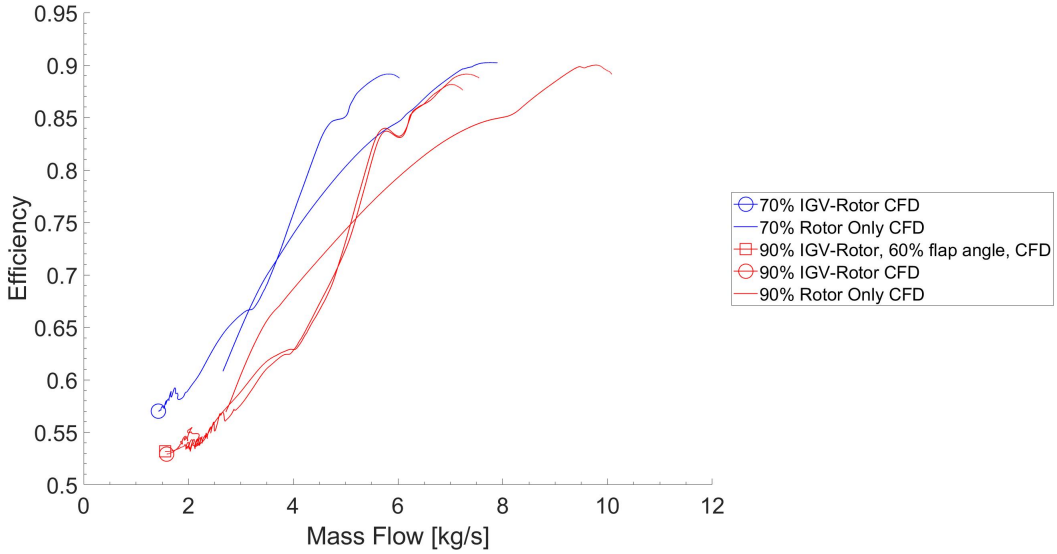


Figure 5.17. Raw CFX efficiency curves for smooth casing treatment model.

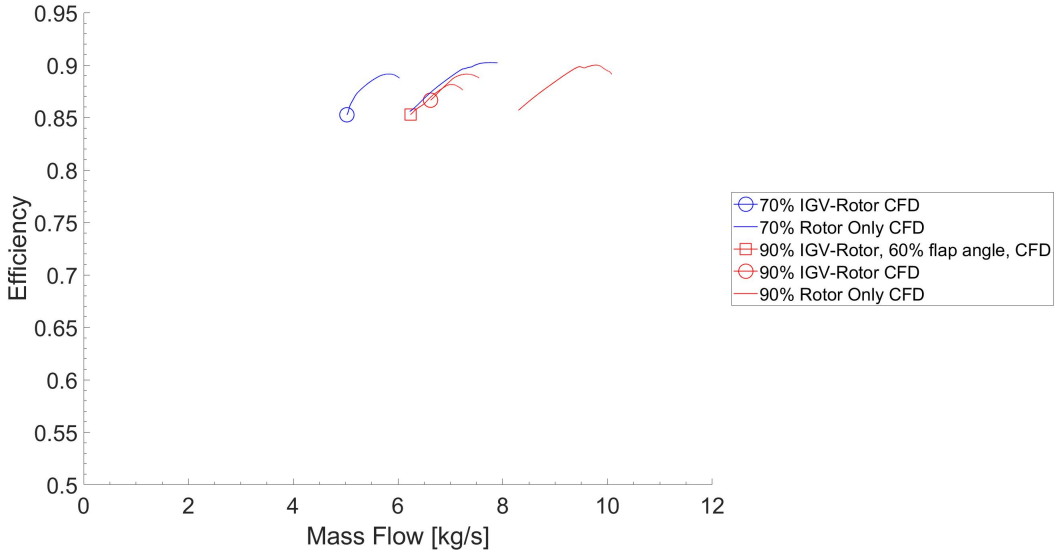


Figure 5.18. Truncated CFX efficiency curves for smooth casing treatment model.

5.2.2 S-Grooves

Table 5.11 presents the conditions which the s-shaped axial groove model was analyzed at; smooth casing models were run for all test points listed as well for comparison. All whirl values were approximated using non-axial boundary conditions specified in section 3.2.3. Initially scheduled values were used, but it was found that using an angle greater than prescribed provided better results from the model as the flow could be pushed subsonic. An additional increased IGV angle was tested and is labeled as "60%" but is not part of the official schedule.

Table 5.11. CFX test conditions for s-shaped axial grooves.

Power	IGV
70%	None
	70%
90%	None
	70%
	60%

From Section 1.2, it is known the s-shaped axial grooves are adapted subsonic casing treatments. As such, it was expected the casing treatments would only work in subsonic or near subsonic conditions. From Figure 5.19 this becomes apparent. The 70% and 90% power settings were chosen because they represent the extreme ends of the transonic compressor operating range. At 90% power the blade tips are supersonic where as at 70% the blade tips are only approaching Mach 1. The resulting performance proves the s-grooves are truly subsonic devices. At 90%, the s-grooves greatly reduce compressor performance, but there is a marginal increase in stall margin at 70%. Similar to increasing the tip-gap size, the maximum pressure ratio decreases for both cases. At 70% though, an interesting phenomenon occurs. The pressure ratio is actually higher for the majority of the performance line, but approaching stall, the slope decreases resulting in a "flat spot" as gasses in the compressor begin recirculating. This is explored visually further down.

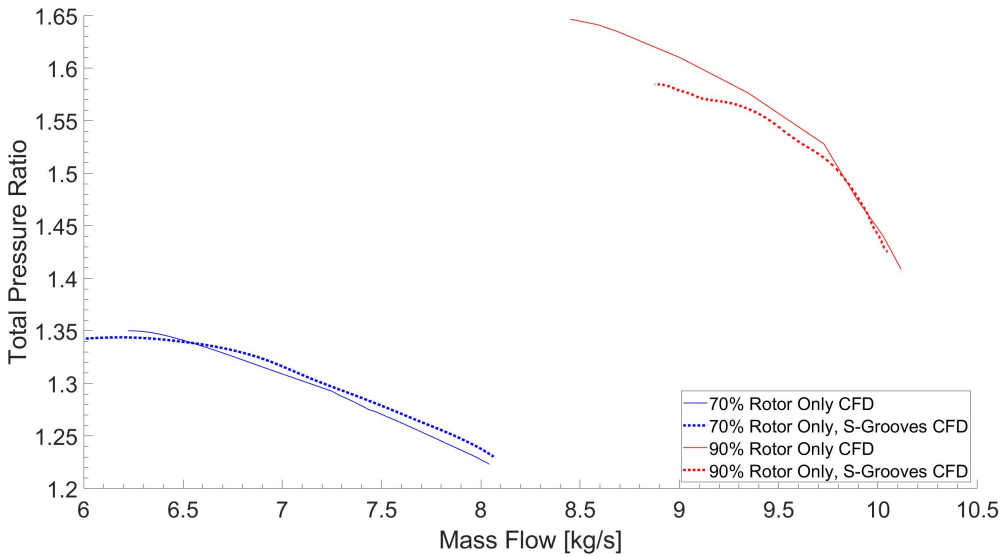


Figure 5.19. Numerical S-Groove performance curves without inlet whirl.

Figure 5.20 presents the efficiency curves for the no whirl s-groove cases. Similar to increasing the tip-gap, the efficiency of the compressor is reduced with the addition of the s-grooves. The reduction in efficiency is most prevalent in the 90% case where there is a nearly 2% drop in efficiency. Additionally, the peak efficiency mass flow is pushed to a lower mass flow rate resulting in a further decrease in stall margin. In the low speed case, the peak efficiency mass flow remains essentially unchanged and the stall mass flow rate decreases, giving a slightly increase in the stall margin. Table 5.12 summarizes the findings for these cases.

Table 5.12. Summary of numerical s-shaped axial grooves performance without IGV.

Power	$\Delta\pi_{tot}$ [%]	$\Delta\eta_{TT}$ [%]	ΔSM [%]
70%	-0.2781	-0.1767	11.3178
90%	-3.7644	-1.6542	-34.6719

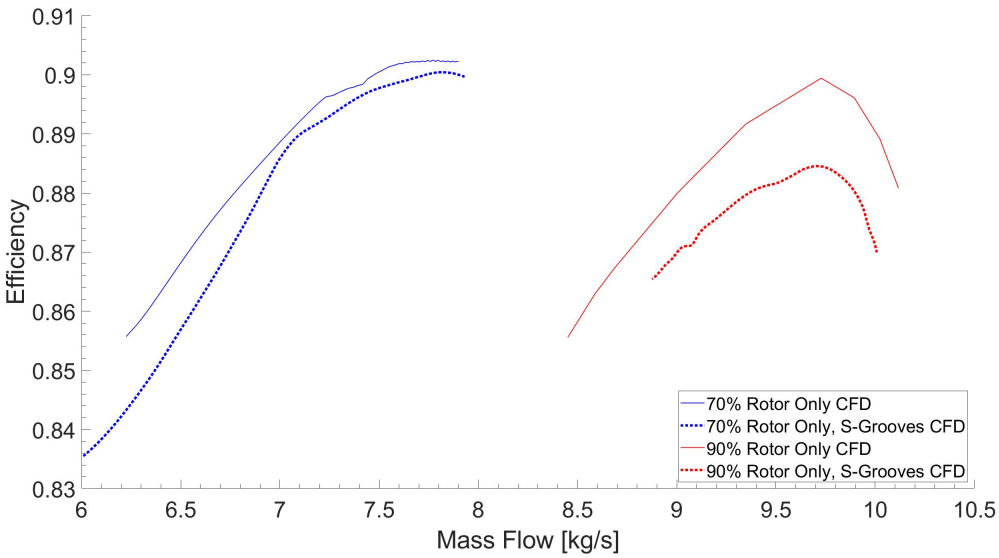


Figure 5.20. Numerical S-Groove efficiency curves without inlet whirl.

To visualize and analyze the flow mechanisms of recirculation, streamlines were placed at the inlet and in the casing treatment. Figure 5.21 shows these velocity streamlines colored using the axial velocity in the stationary frame. The plot is scaled such that flow moving axially through the compressor is red but blue represents flow which has reversed direction. This serves to demonstrate that flow is indeed recirculating due to the s-grooves.

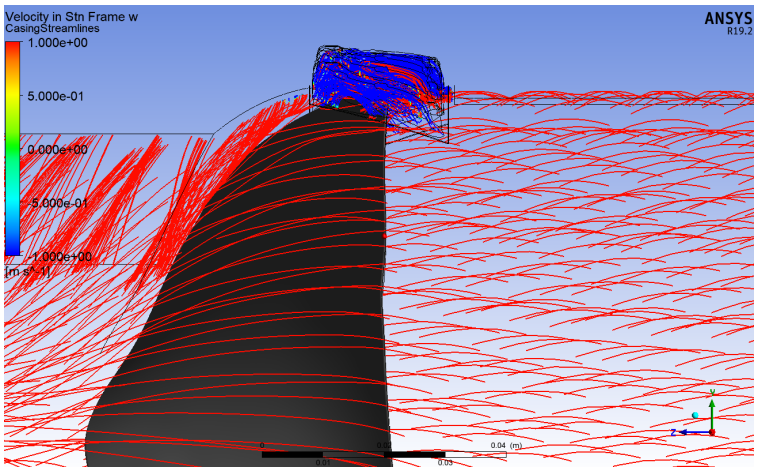


Figure 5.21. Axial velocity in the compressor near peak efficiency.

From Figure 5.22 it can be seen that the relative flow at the tip only achieves local supersonic velocities on the suction side of the blade tip at the 70% speed setting. This is nearly a subsonic case. Flow is entering from the left of the page and the blades are rotating up the page.

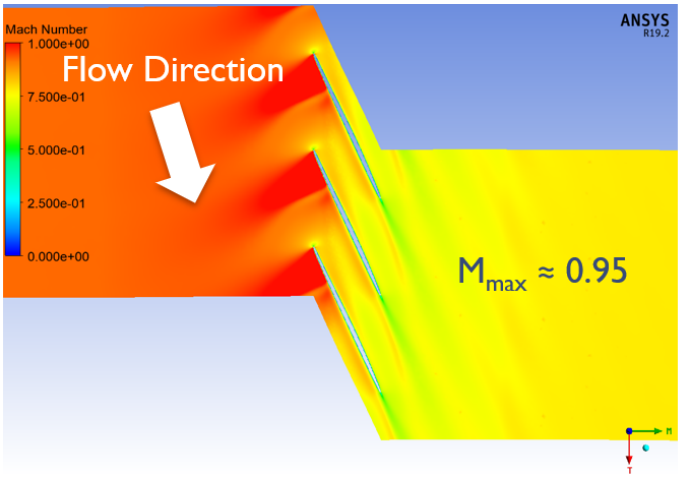


Figure 5.22. Blade-to-blade view displaying Mach number at 95% blade chord for the 70% power setting.

Figure 5.23 presents the progression of the recirculation in the compressor as it approaches then does stall. From the three un-stalled images, the recirculation region can be seen growing and moving forward, but it progresses downward only behind the blade leading edge and the leading edge shock. However, after stall (last image) the recirculation region grows downward rapidly and moves forward as the compressor numerically stalls.

Figure 5.24 presents the same evaluation points looking at the blade from the LE with only the streamlines in the casing treatment activated. This provides a better view of velocity in the casing treatment and the depth of the recirculation. At the more stable points on the power line, recirculation velocity in the grooves remains low and the depth of the resulting recirculation is small. This results in minimal losses at these stable points (see Figure 5.20), but as the compressor approaches an unsteady state, the velocity in the recirculation grooves drastically increases and the recirculation extends well below the boundary layer. The activation of the channels can also be seen from this view. As the blade approaches the channels begin to recirculate rapidly (left side of images), but as the blade passes underneath the tip vortex of the blade slows the recirculation down as the flow mixes.

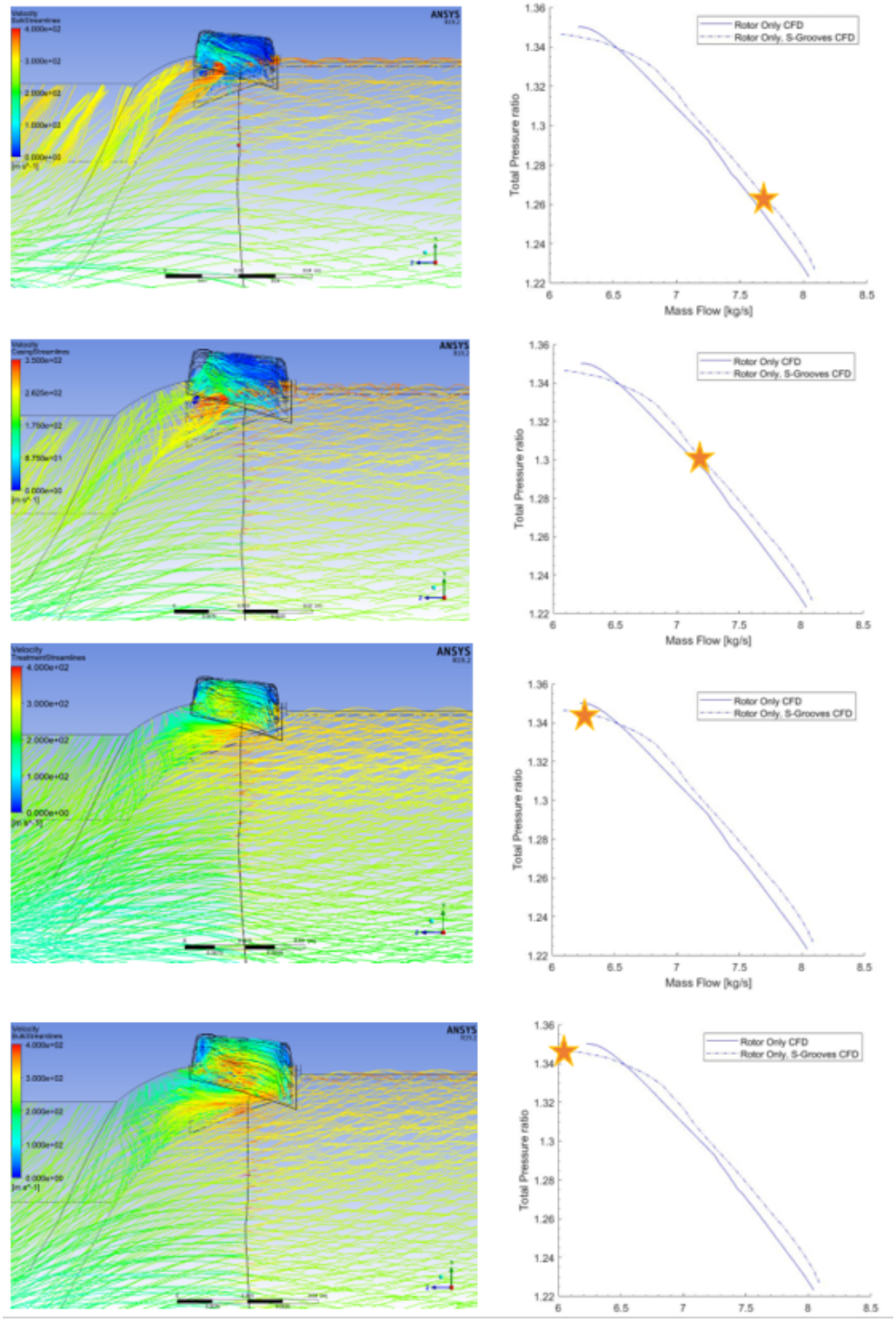


Figure 5.23. Recirculation development in the compressor at 70% power with no inlet whirl.

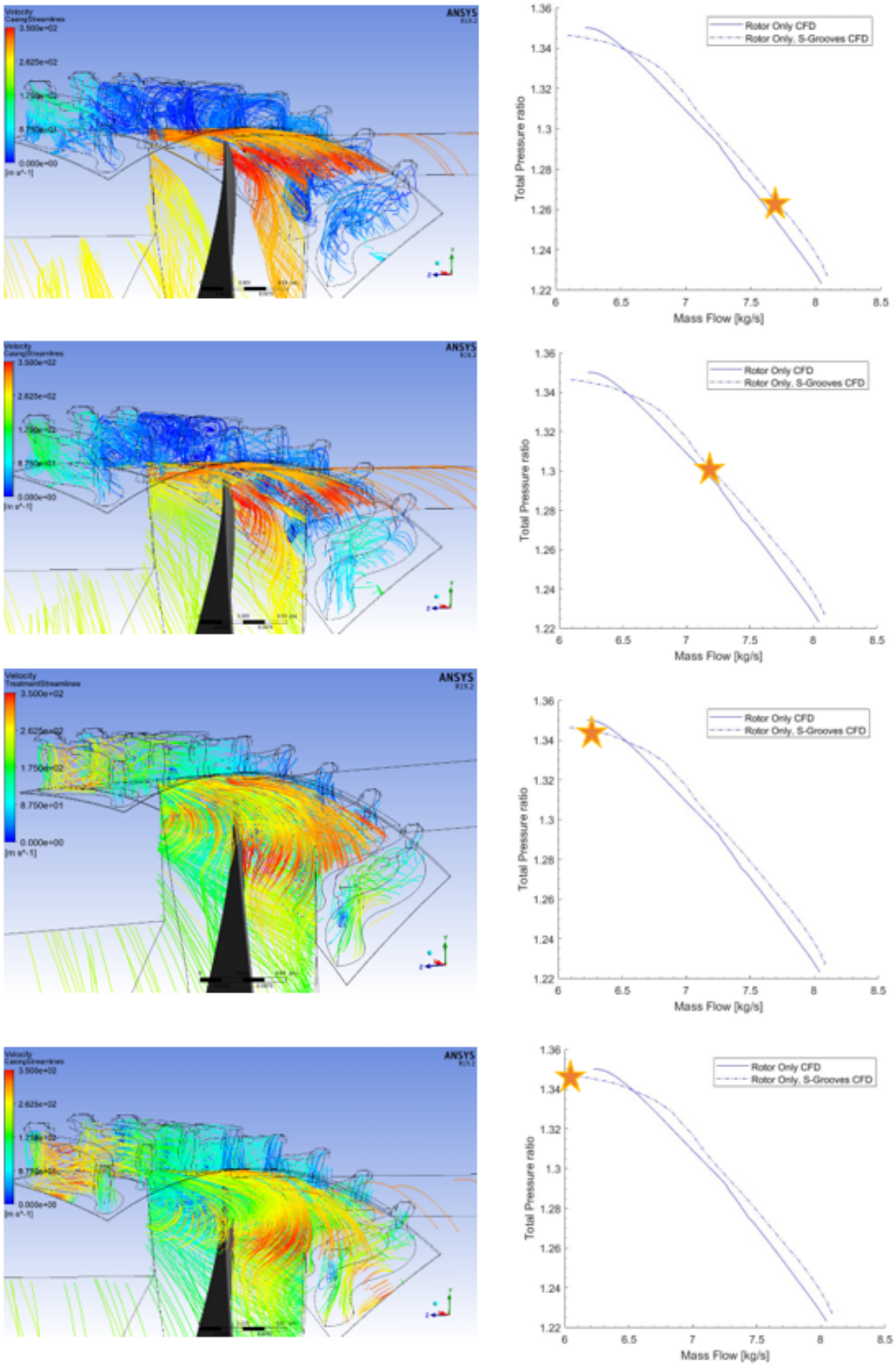
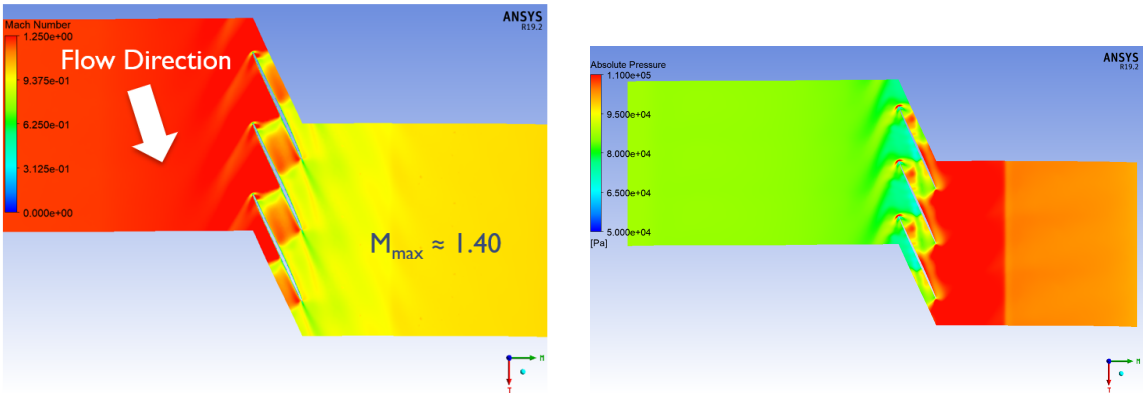


Figure 5.24. Recirculation development in the compressor at 70% power with no inlet whirl viewed from the LE.

At 90% power the tip speed of the compressor approaches M = 1.40 resulting in even worse recirculation. Figure 5.25 shows the Mach and pressure plots of the compressor at 95% chord. The pressure plot is included to better visualize the oblique shocks present as the Mach number remains supersonic through the shocks except at the blade LE.



(a) Mach number at 95% chord. (b) Pressure at 95% chord.

Figure 5.25. Shock visualization in the compressor at 90% speed with no inlet whirl.

The stronger shocks results in negligible recirculation until the compressor stalls. Figure 5.26 displays the development of stall in the velocity streamlines of the compressor at 90% power. Recirculation is occurring throughout the mass flow range, but at higher mass flow rates, little mass is recirculated resulting in little to no recirculation. Immediately before stall, recirculation can be seen behind the LE shocks. However, the compressor still stalls well before the smooth casing treatment case. The early stall is due to the passages not properly recirculating the flow due to the presence of the shocks - essentially creating a compressor with intermittent large tip gaps which allow blade tip spillage.

Figure 5.27 further illustrates the poor recirculation. The streamlines in the casing treatment are set up to show the flow through the casing treatment before and after it goes through the casing. As can be seen in the third image, little flow is being pulled into the s-grooves leaving little energy for the s-grooves to introduce into the flow. All the s-grooves due in a purely supersonic environment is allow tip spillage resulting in reduced efficiency, pressure ratio and stall margin.

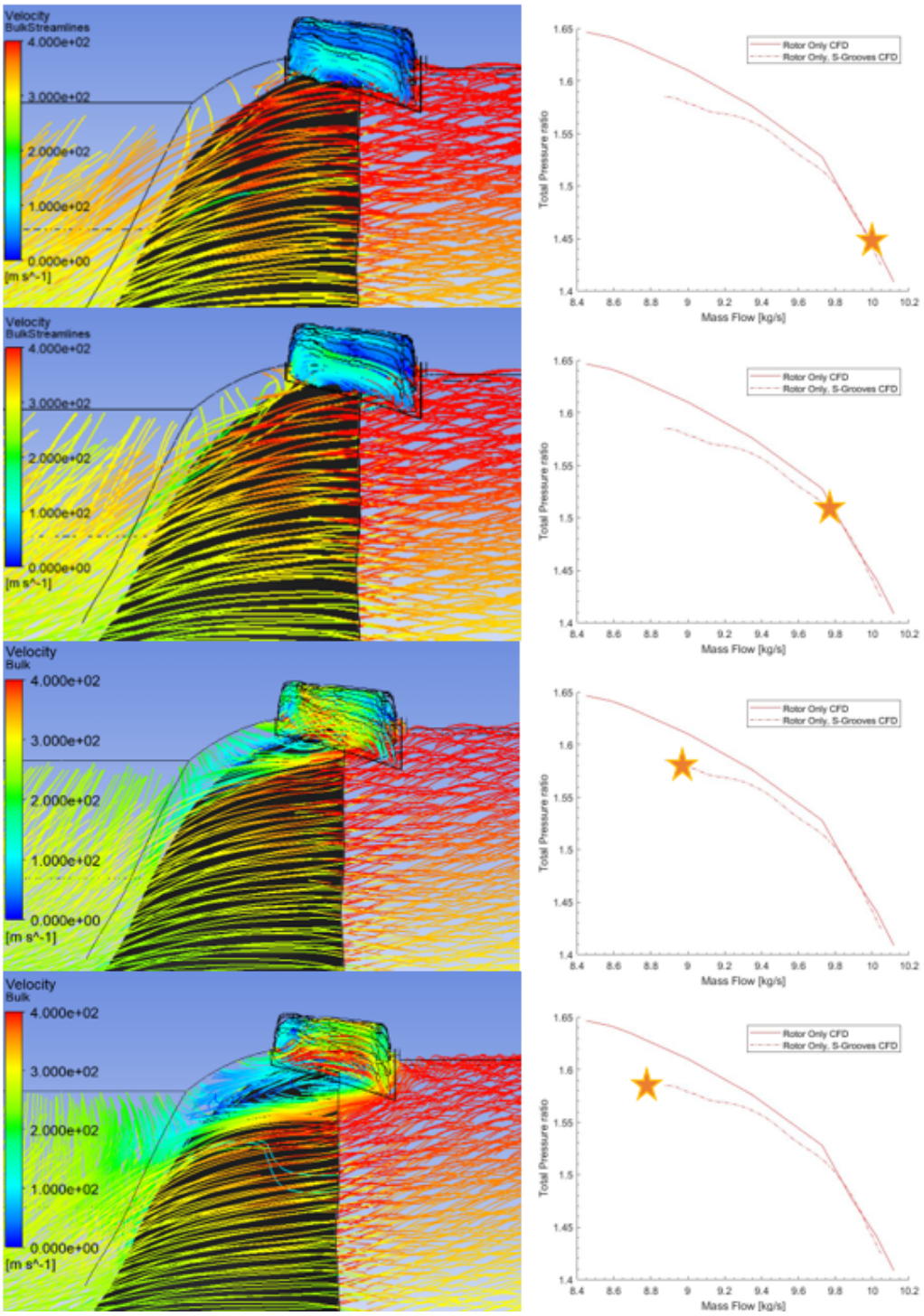


Figure 5.26. Recirculation development in the compressor with s-groove treatment at 90% power with no inlet whirl.

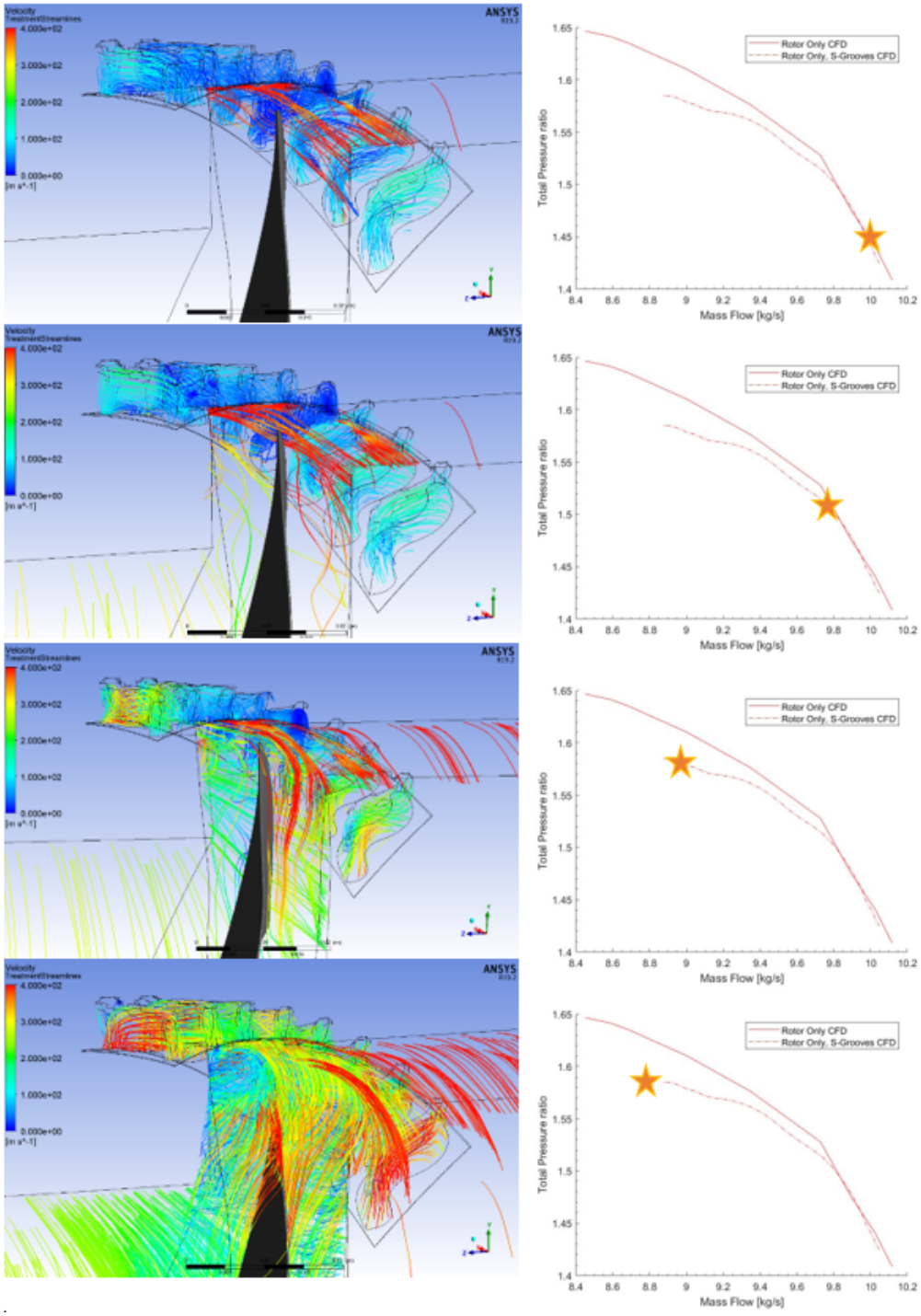


Figure 5.27. Recirculation development in the compressor at 90% power with no inlet whirl viewed from the LE.

The addition of whirl dramatically changes the performance of the s-grooves as seen in the experimental results. The whirl added to the simulation is only an approximation of the IGV. However, the goal of adding the IGV approximation to the simulation was to replicate the reduction in mass flow, relative tip velocity, and angle-of-attack achieved by the IGV. A smooth casing treatment model was run with the same whirl model to provide a baseline performance to compare against.

Figure 5.28 presents the performance curves for the compressor with whirl added. In the figure, a single marker at the stall point is used to denote whirl and was super-imposed on the pseudo-steady result. The first point of interest is the increased pressure ratio with the s-groove installed. Without whirl the 70% speed line demonstrated a slightly higher pressure ratio while the 90% power experienced a reduction in power. The difference between the two simulations was attributable to the higher Mach number of the blade tips at 90%. However, with the added whirl, the 90% power setting experiences Mach numbers akin to those seen by the 70% case without whirl. The resulting change in incidence provided by the whirl also effects the performance of the s-grooves. Increasing the whirl past the 70% setting actually reduced the effectiveness of the s-grooves. This is an interesting finding as it shows the sensitivity of the rotor to the whirl and proves the lower bounds set forth by the schedule. The increased whirl followed the pattern of scheduling used in the TCR and increased the whirl by less than 8%; however, this increase drastically changed the operation of the compressor. Figure 5.29 shows the resulting streamlines with the compressor near the peak efficiency point and 60% whirl setting. Not enough mass flow is allowed into the rotor with the increased whirl and flow begins recirculating essentially narrowing the compressor inlet.

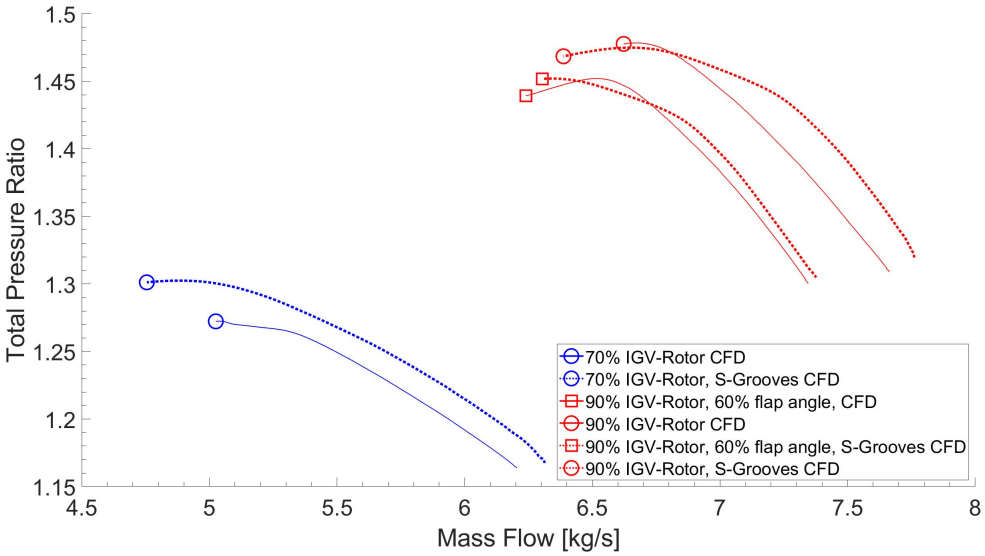


Figure 5.28. Numerical S-Groove performance curves with inlet whirl.

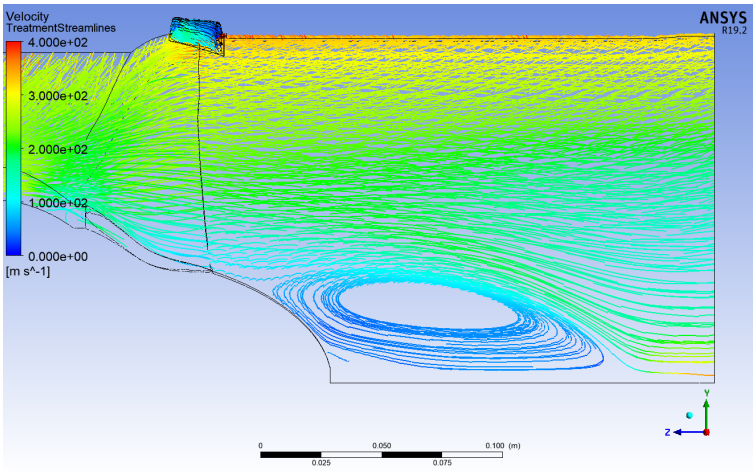


Figure 5.29. Unique behavior observed with the compressor at 90% speed and the IGV set for 60% speed.

The efficiency predicted by CFX is extremely high, and as can be seen in Figure 5.30, the simulation predicts a higher peak efficiency than the smooth casing treatment. From the non-whirl cases, a reduction in efficiency is expected; this would also follow the findings of previous work.

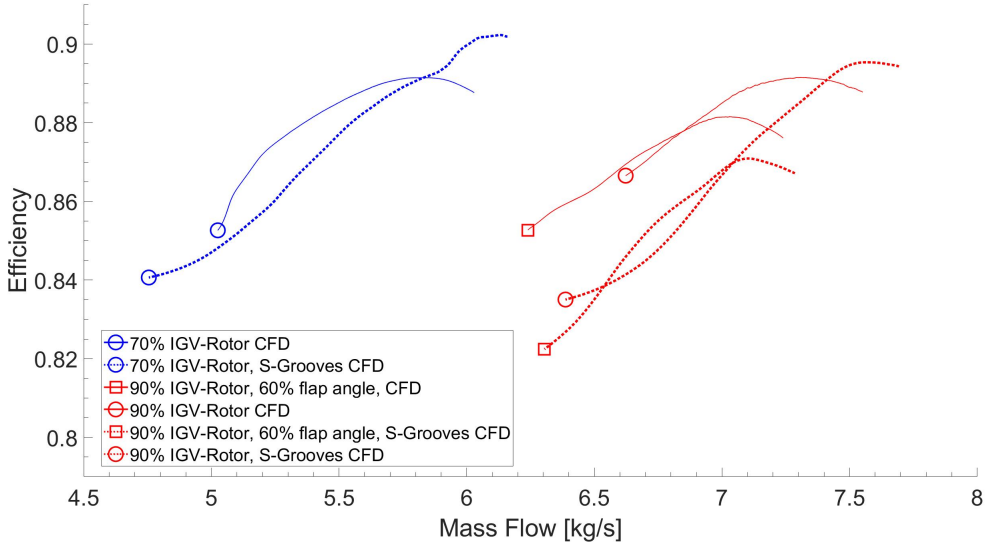


Figure 5.30. Numerical S-Groove efficiency curves with inlet whirl.

Table 5.13 summarizes the findings from the whirl added cases. These simulations used a frozen rotor interface to allow better flow visualization of the tip region; however, frozen rotor does not provide the best performance evaluation. A mixing plane approach could provide better efficiency values but would provide less accurate instantaneous data transfer, poor visuals, and is much costlier.

Table 5.13. Summary of numerical s-shaped axial grooves performance with IGV model.

Power	Flap Angle	$\Delta\pi_{tot}$ [%]	$\Delta\eta_{TT}$ [%]	ΔSM [%]
70%	70%	2.3568	1.2169	60.8106
90%	70%	-0.0547	0.4360	53.5909
90%	60%	0.1739	-1.1753	-5.6379

With the addition of whirl, the 70% case is solidly in the subsonic regime as can be seen by Figure 5.31. The lack of LE shocks allows for the s-grooves to operate as designed and allows a relatively stable recirculation bubble to form.

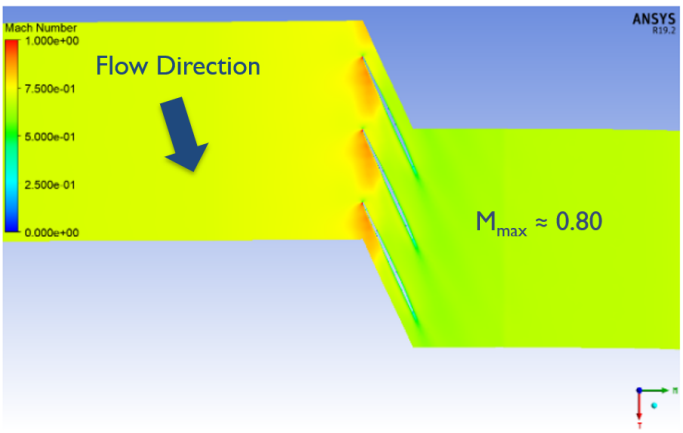


Figure 5.31. Blade-to-blade view displaying Mach number at 95% blade chord for the 70% power setting after inlet whirl has been added.

Figure 5.32 depicts the side view of the recirculation region forming in the 70% case with whirl. At high mass flow rates, the passages have a minimal effect on the operation of the compressor, but the recirculation is able to begin more rapidly than in the transonic regime. Streamlines from the inlet can be seen deflecting in the second image as the velocity in the passages accelerates. As the compressor nears stall, the velocity in the passage reaches greater speeds than the flow in the gas passage and the recirculation bubble grows and moves out past the front of the blade. This simulation reaches an unsteady state. The recirculation regions seen are not a steady phenomenon, so stall is where the simulation can no longer compensate for the unsteadiness. In this case, the compressor numerically stalled and pushed the recirculation isolation region up the inlet. It can be seen in the last image that some flow from the boundary layer is still being siphoned off while the bulk of the flow is deflected downwards.

Figure 5.33 presents the growth of the recirculation region in detail. The grooves begin mixing the boundary layer into the tip region in the second image. Near stall, a well defined vortex has formed due to the high-speed mixing due to the s-grooves. After stall, the vortex has expanded and begun falling apart.

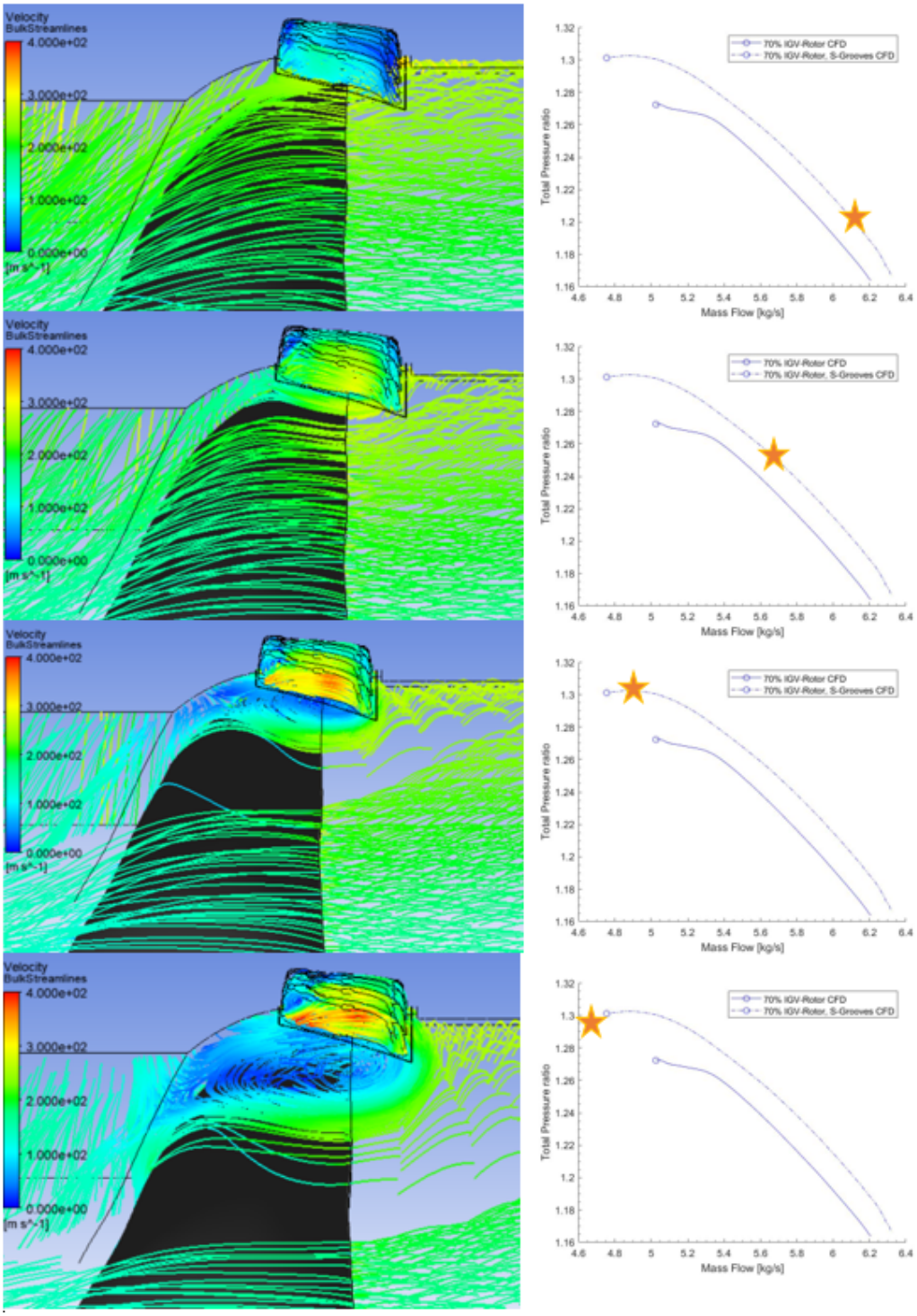


Figure 5.32. Recirculation development in the compressor with s-groove treatment at 70% power and 70% IGV schedule.

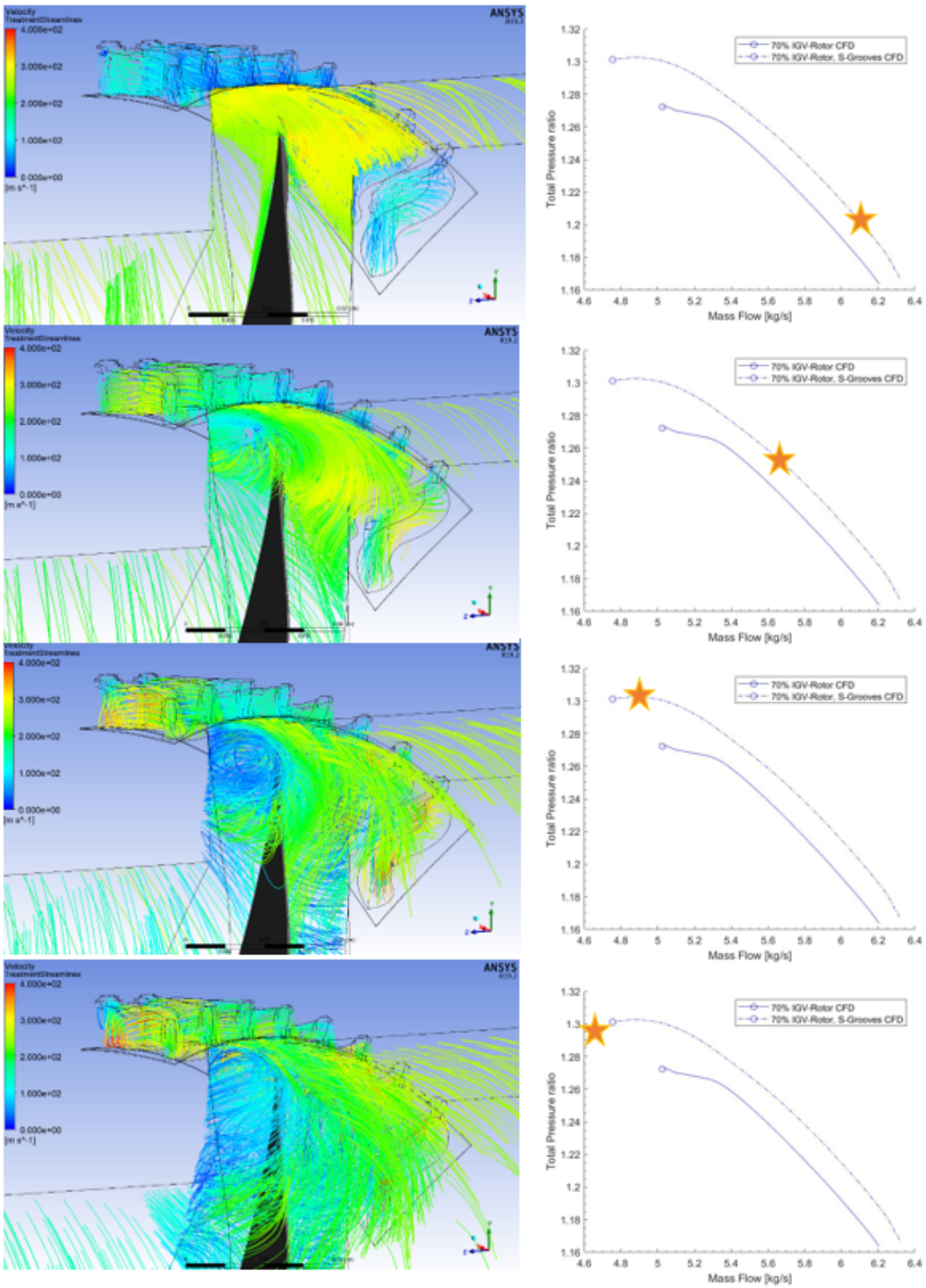


Figure 5.33. Recirculation development in the compressor at 70% power and 70% IGV schedule viewed from the LE.

The 90% case with whirl added is transonic in the truest sense of the word. Flow near the blade tip reaches locally super sonic speeds, but generally lies in the Mach 0.95 range. Figure 5.34 displays the Mach number plot at 95% chord. The result is similar to Figure 5.22 which displays the Mach number plot for the 70% no whirl case.

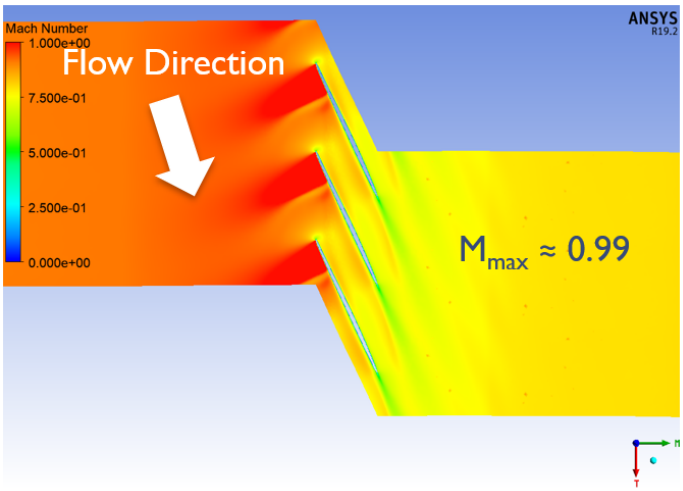


Figure 5.34. Blade-to-blade view displaying Mach number at 95% blade chord for the 90% power setting and 70% IGV schedule.

Flow mechanisms for the 90% whirl case lie between the 70% no whirl case and the 70% whirl case. Recirculation occurs to a greater extend than the baseline 90% scenario which does serve to extend the stall margin, but it is not the massive recirculation seen in the 70% IR configuration. Figure 5.35 shows slight recirculation occurring before stall, but it is limited by the slight onset of shocks on the LE. In Figure 5.36, the same vortex generation can be seen as the 70% whirl case with the vortex falling apart upon stall. Velocity in the 90% case is much higher in the passages as expected. This is an unsteady condition and limited by the simulation type.

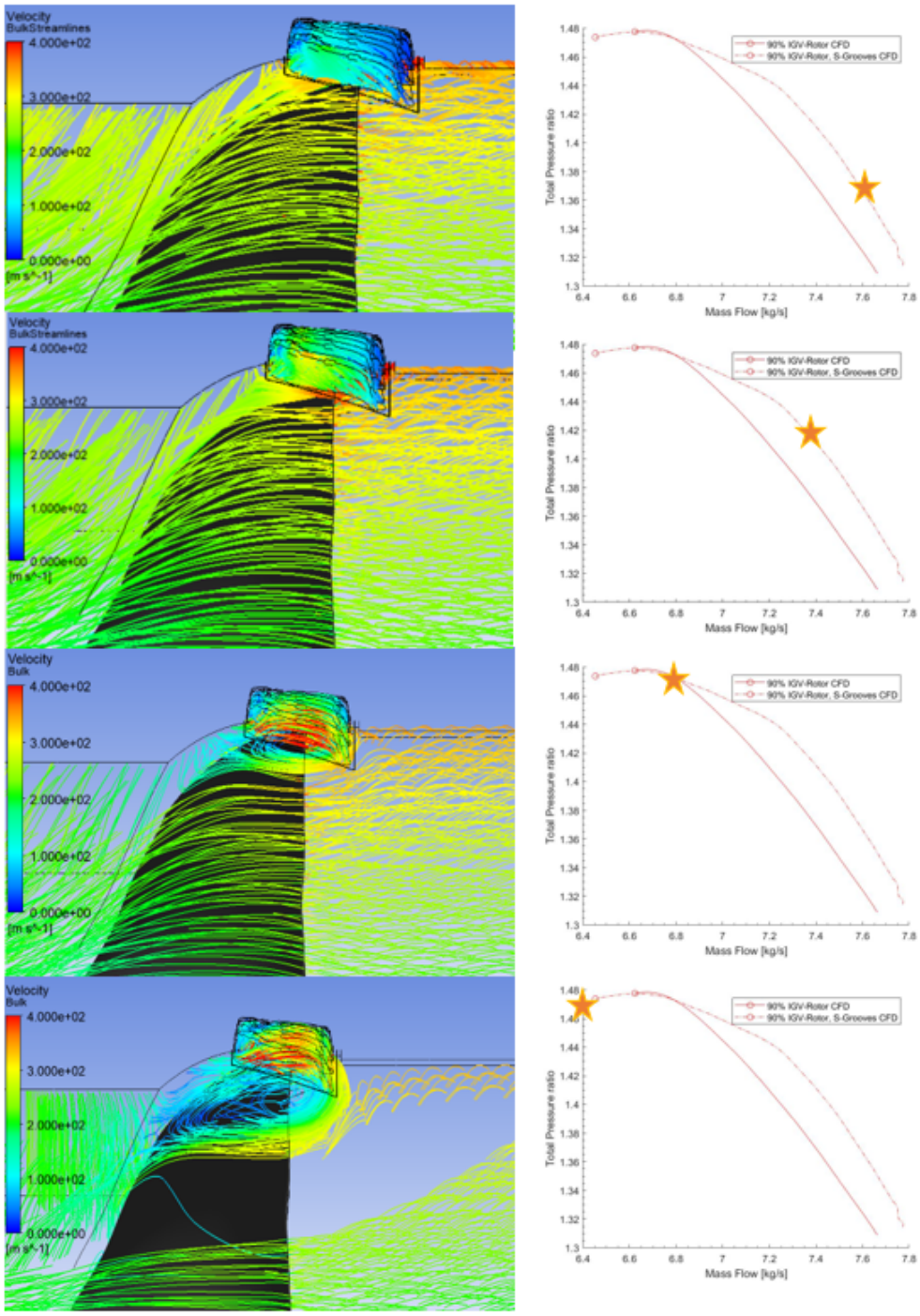


Figure 5.35. Recirculation development in the compressor with s-groove treatment at 90% power and 70% IGV schedule.

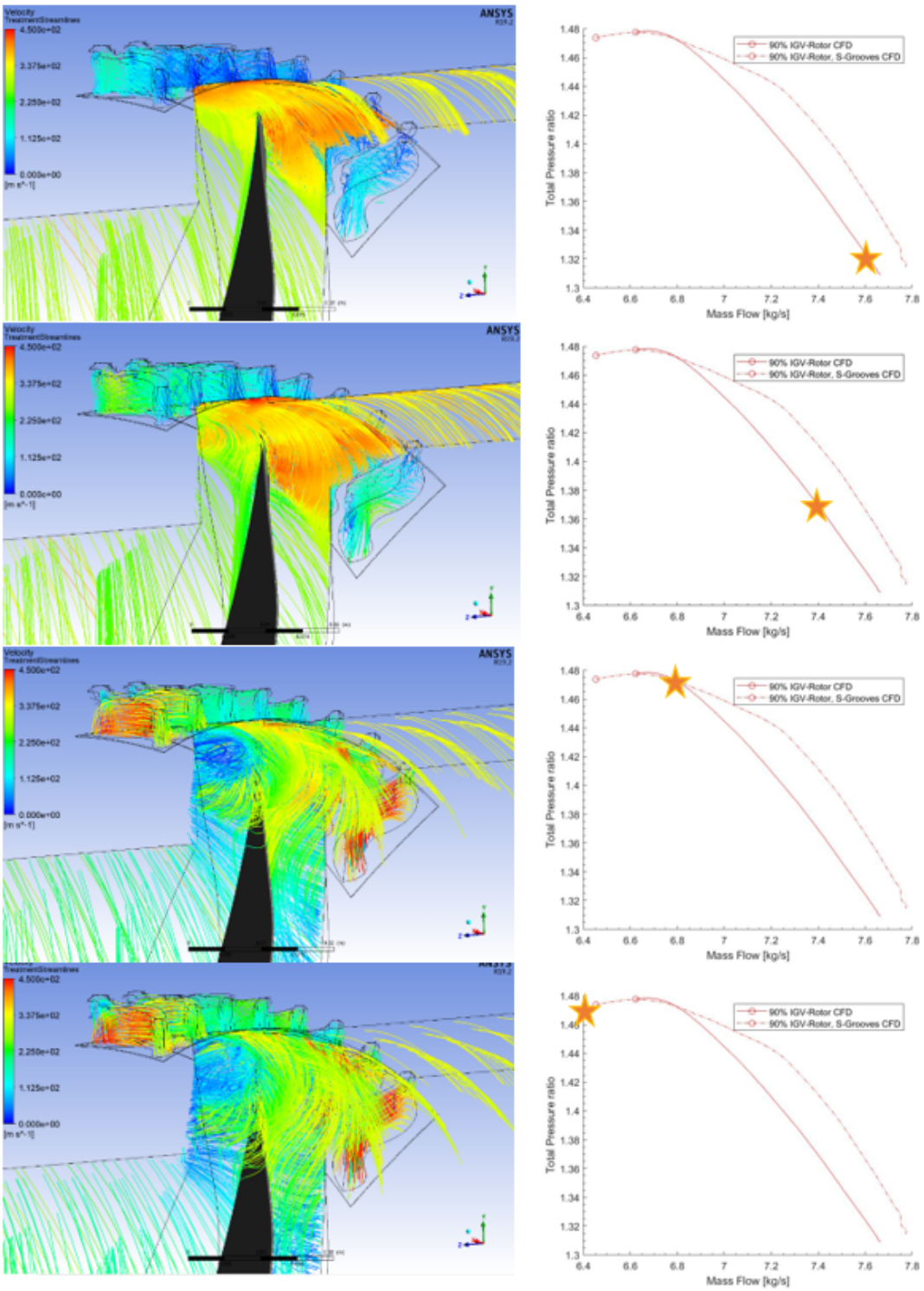


Figure 5.36. Recirculation development in the compressor with s-groove treatment at 90% power and 70% IGV schedule viewed from the LE.

5.2.3 Internal Passages

The internal passages were tested at he conditions listed in Table 5.14. Since the addition of whirl did not prove effective, the internal passages were only run at the established settings. Interface simulation in CFX is an expensive operation, so internal passage operation were costly in time and RAM required. Simulations required twice as many cores as the s-groove simulations, but had similar run times.

Table 5.14. CFX test conditions for novel internal passages.

Power	IGV
70%	None
	70%
90%	None
	70%

The internal passages work in a significantly different manner than the s-grooves. Unlike the open nature of the grooves, the internal passages bleed a minimal amount of air from the boundary layer behind the blade and reinsert it ahead of the blade allowing the tip gap to remain small. Additionally, the passages are narrow and can be approximated by Fanno flow. This results in a form of dampening in the recirculation. Velocity in the passage remains relatively low throughout the operating range while continuing to work in a more even manner.

These difference lead to much better performance than what was seen with the s-grooves — especially in the no whirl case. Figure 5.37 shows the performance curves for the no whirl simulations. Interestingly, the total pressure ratio actually begins dipping before the compressor actually stalls. The passages are able to generate a form of stability through energizing the boundary layer. In the subsonic case, the pressure ratio actually maintains the positive slope well past the smooth casing resulting in a higher total pressure ratio.

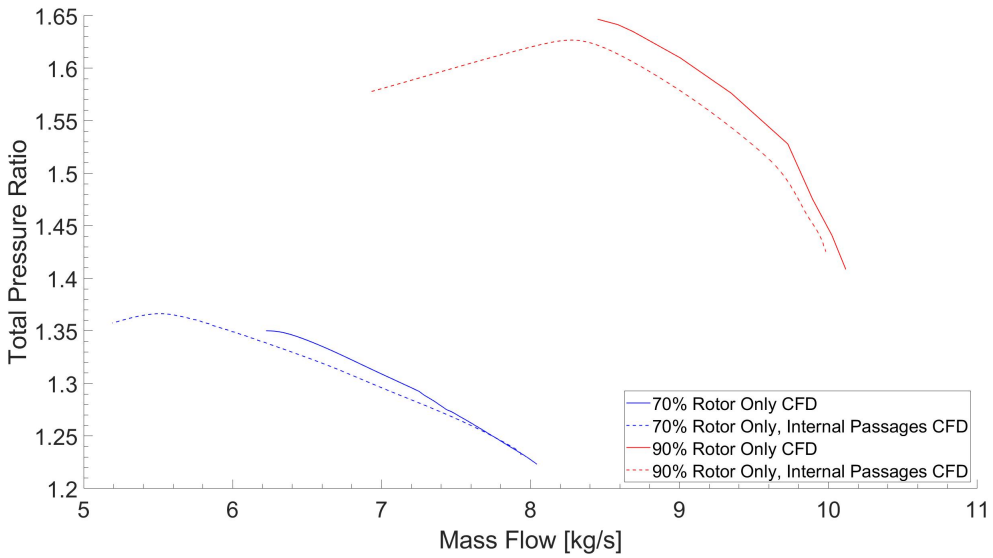


Figure 5.37. Numerical internal passage performance curves without inlet whirl.

Efficiency is less effected than the s-groove case. Both cases are within the uncertainty of the simulation, but the stability of cases can be seen in the linear portion of the efficiency curve. Both display a linear decrease in efficiency which abruptly departs upon stall. An interesting function of the internal passages is the clear definition of numerical stall. Unlike the s-grooves which have a highly unsteady region preceding and throughout stall making the identification of stall difficult, the internal passage cases maintained stability up until stall. The behavior is more similar to the stall behavior reported in [11]. Table 5.15 summarizes the key results of the internal passage no-whirl simulations.

Table 5.15. Summary of numerical internal self-recirculating performance without IGVs.

Power	$\Delta\pi_{tot}$ [%]	$\Delta\eta_{TT}$ [%]	ΔSM [%]
70%	1.2058	0.1945	71.6575
90%	-0.9115	0.1796	82.6137

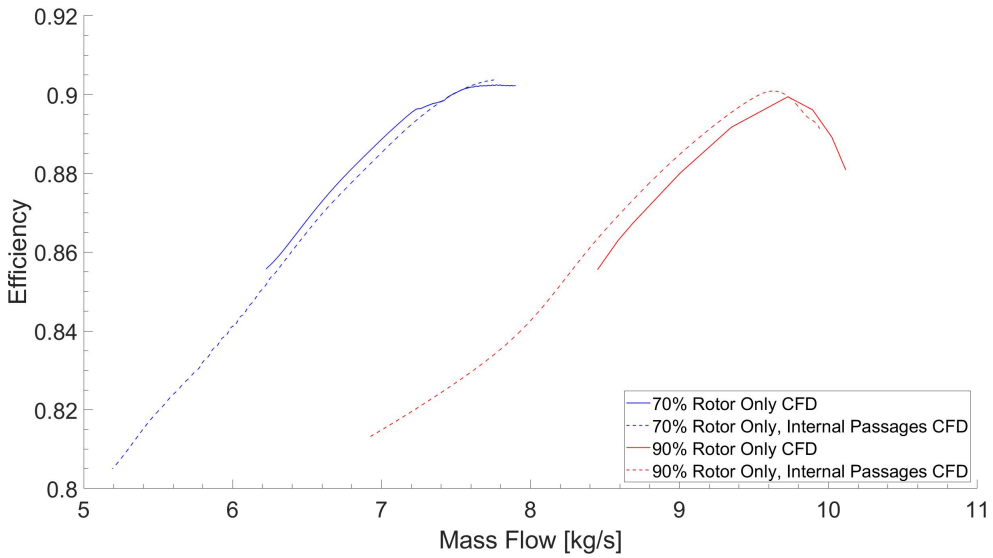


Figure 5.38. Numerical internal passage efficiency curves without inlet whirl.

The internal passages remain effective when whirl is added, but at the lower pressure ratios are not as effective. Figure 5.39 shows the performance curve for the internal passages with the whirl set at 70%. Behavior is strikingly similar at 90% speed but the performance is limited at 70%. Due to the constricted nature of the passage, they rely on a high back pressure to force flow through the passages. The 70% with whirl case is a subsonic case with much lower pressure ratios, resulting in less effective passage recirculation.

Efficiency follows the opposite trend from the no whirl case. The 90% speed has a small, but consistent reduction in efficiency while the 70% case actually sees an increase in efficiency. The findings are summarized in Table 5.16.

Table 5.16. Summary of numerical internal self-recirculating performance with IGVs.

Power	$\Delta\pi_{tot}$ [%]	$\Delta\eta_{TT}$ [%]	ΔSM [%]
70%	-0.2493	0.8373	48.7204
90%	-2.6682	-0.1355	79.1463

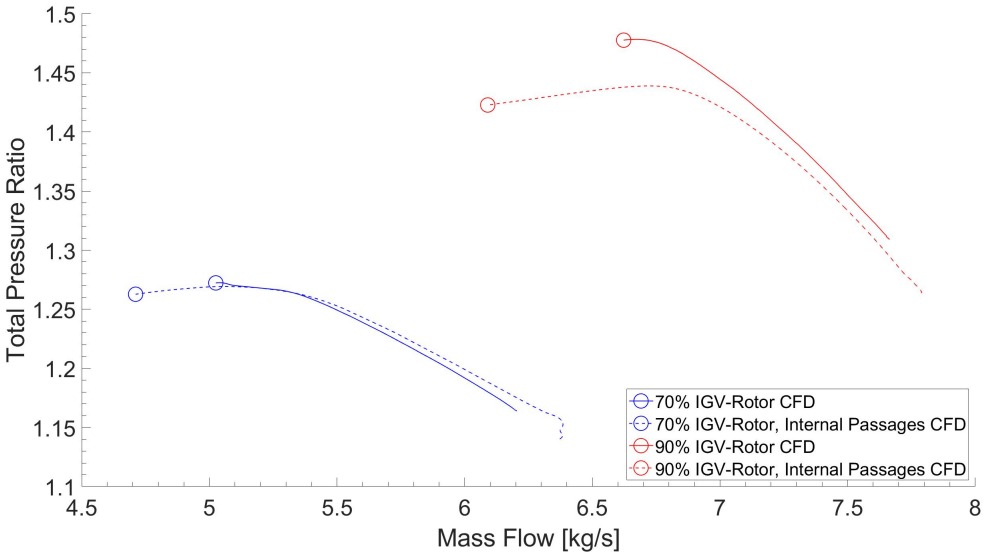


Figure 5.39. Numerical internal passage performance curves with inlet whirl.

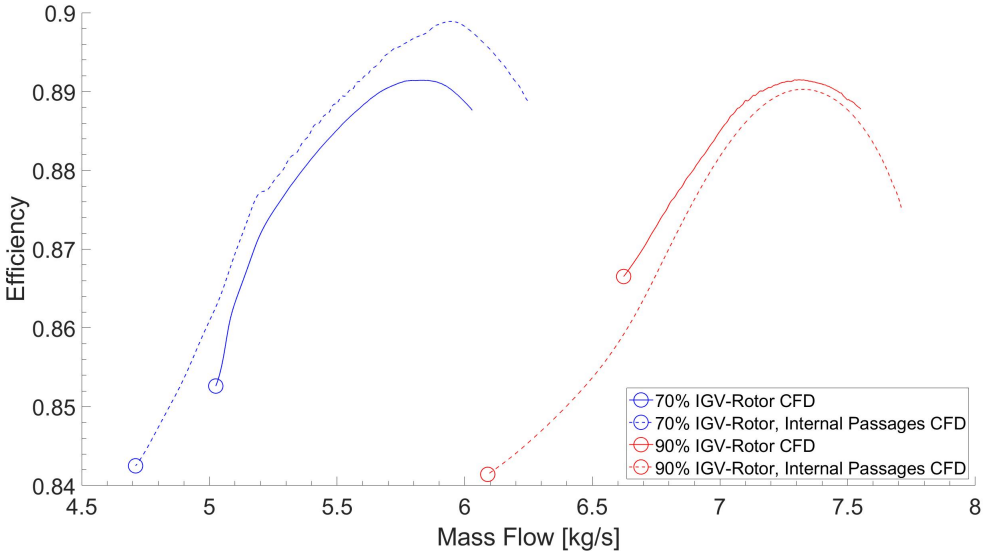


Figure 5.40. Numerical internal passage efficiency curves with inlet whirl.

The internal passages were designed to bleed 2.5% of the compressor flow at the peak pressure. A monitor point was used to measure the mass flow through the passages and normalize it to the corrected mass flow through the compressor. Figure 5.41 displays the results for the four cases studied. The mass flow through the passages increases with the pressure ratio and begins declining as the pressure ratio drops off. The lack of mass flow through the passages directly precedes the compressor stall. As can be seen, the addition of whirl does not affect the normalized mass flow ratio, but rather it is a function of compressor RPM. Finally, none of the passages actually reach 2.5%, but they still manage to increase the stall margin.

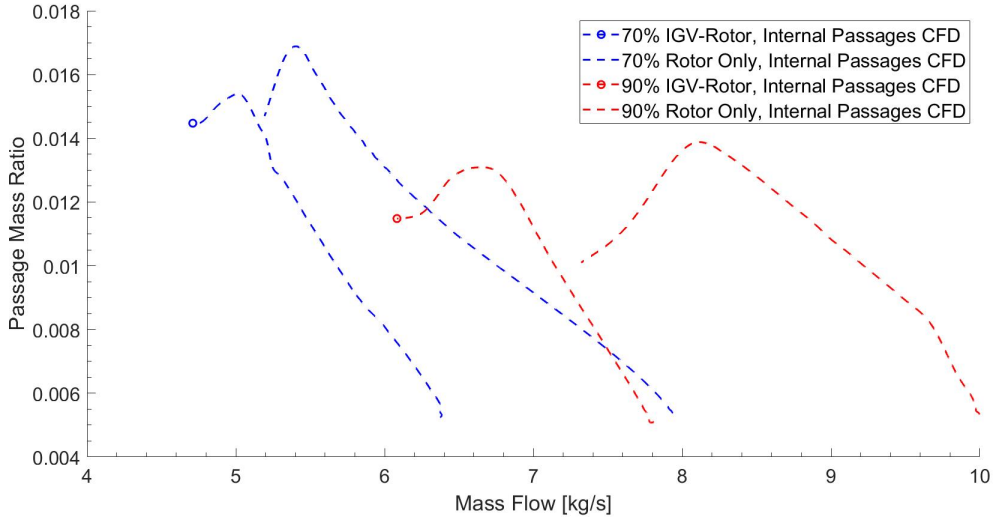


Figure 5.41. Mass flow ratio of flow through the internal passages against mass flow through the compressor.

The internal passages are able to recirculate and inject the bleed flow into the boundary layer effectively. By removing the recirculation from the compressor passage and putting it in discrete passages, the flow is able to be injected precisely without flow recirculating before the desired area. This leads to high-speed flow being injected into the boundary layer directly ahead of the compressor blades. Figure 5.42 details the flow recirculation in the compressor. As can be seen, only the passages ahead and on top of the blade actually recirculate flow. In an experimental set up this could lead to transient effects. A prime number of passages should be used to avoid exciting the blade. The passages gradually activate as the blade passes and insert flow into the boundary layer. The flow exiting the passages is high velocity

and remains in the boundary layer. Energy addition into the boundary layer causes a more steady operating condition.

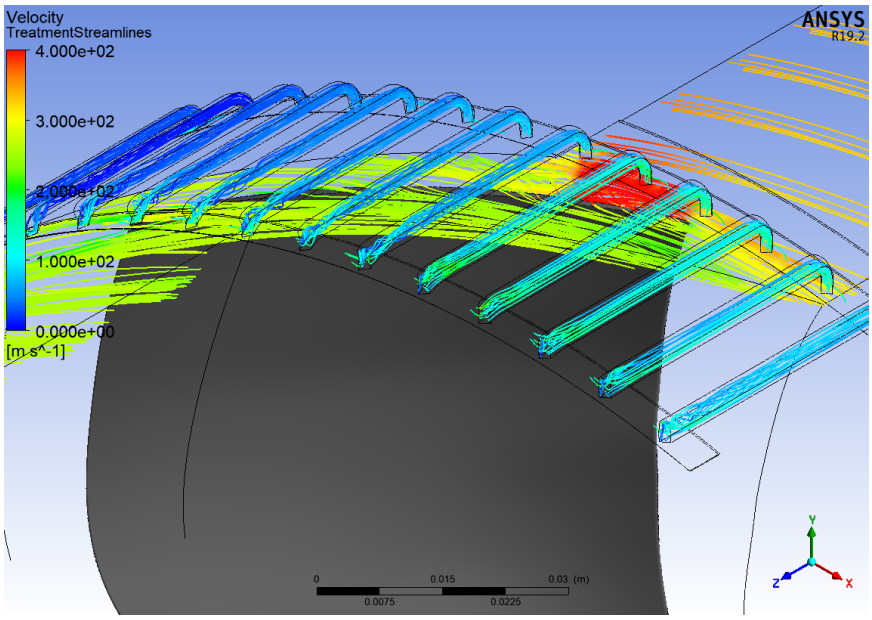


Figure 5.42. Detailed view of compressor operation with internal passage recirculation.

Figure 5.43 presents the development of stall in the compressor with the internal passages installed. The key observation is the lack of recirculation in the tip region until the compressor stalls. Disregarding the changes in velocity, the compressor operates in a smooth manner until it stalls — well past the normal stall point. The internal passages move the flow recirculation and injection out of the actual passage and keeps it from interacting until injection in the boundary layer resulting in a more stable simulation.

Viewing the compressor from the front shows the changes which do occur as the compressor is driven to stall. Velocity within the passages increases up until stall, and as the pressure ratio across the compressor increases, more channels become active simultaneously. This is likely what drives the mass flow ratio up as the pressure ratio increases. Figure 5.44 presents these findings.

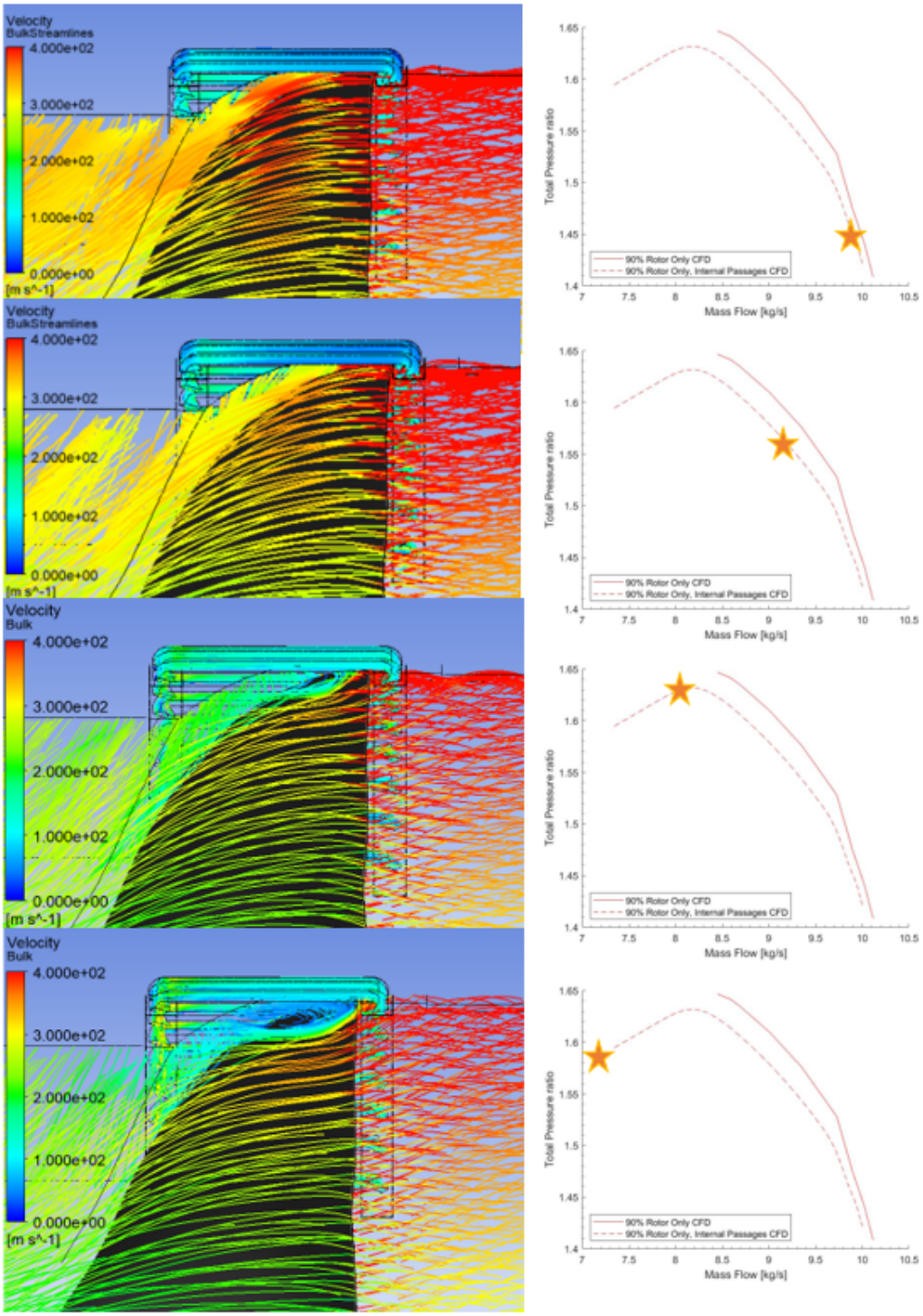


Figure 5.43. Flow development for the compressor with internal recirculation passages at 90% speed with no inlet whirl.

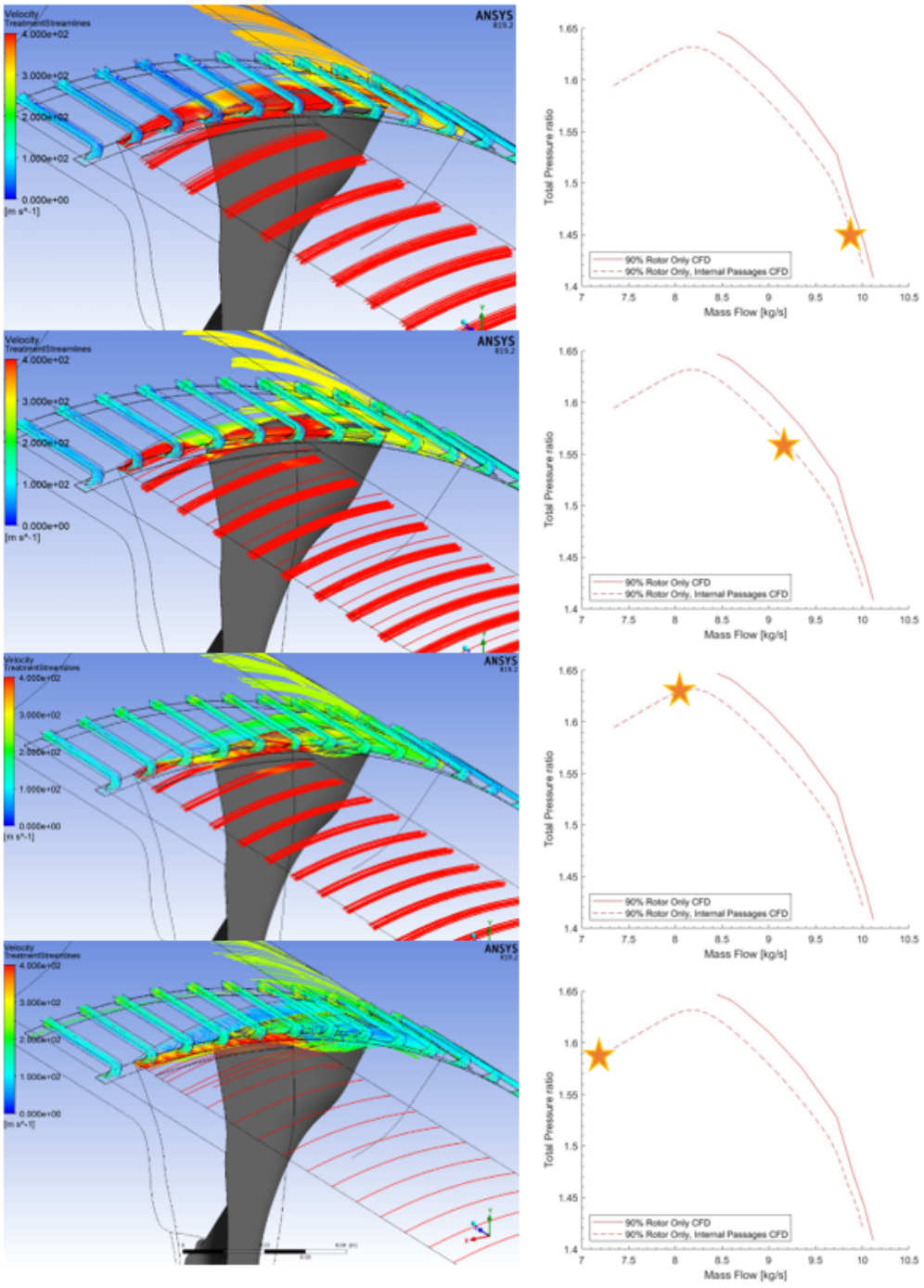


Figure 5.44. Flow development detailing passage operation for the compressor at 90% speed and no inlet whirl with internal passages installed.

The introduction of whirl takes the flow primarily subsonic — even at 90% speed — as was shown in Figure 5.34 which results in lower pressure ratios and less mass recirculation. This results in an earlier onset of bulk flow recirculation and stall, but the flow does not experience recirculation in the same manner as the axial groves. Figure 5.45 shows the development of the recirculation region leading to stall. Noticeable recirculation does not occur until out past the base line case's stall point, and stall occurs much more suddenly than was seen with the s-grooves.

Figure 5.46 shows the development of recirculation in the passages as the compressor approaches stall. In the first two images, the passages start recirculating as the blade approaches and inject high velocity flow into the boundary layer at the LE of the blade, which is where the largest pressure deferential is located. However, as the passage approaches stall and the mass fraction in the passage increases, more passages become increasingly active and more high velocity flow is injected in front and behind the leading edge. In the final image the compressor is fully stalled and flow pushed from the passages enters the recirculation of the passage.

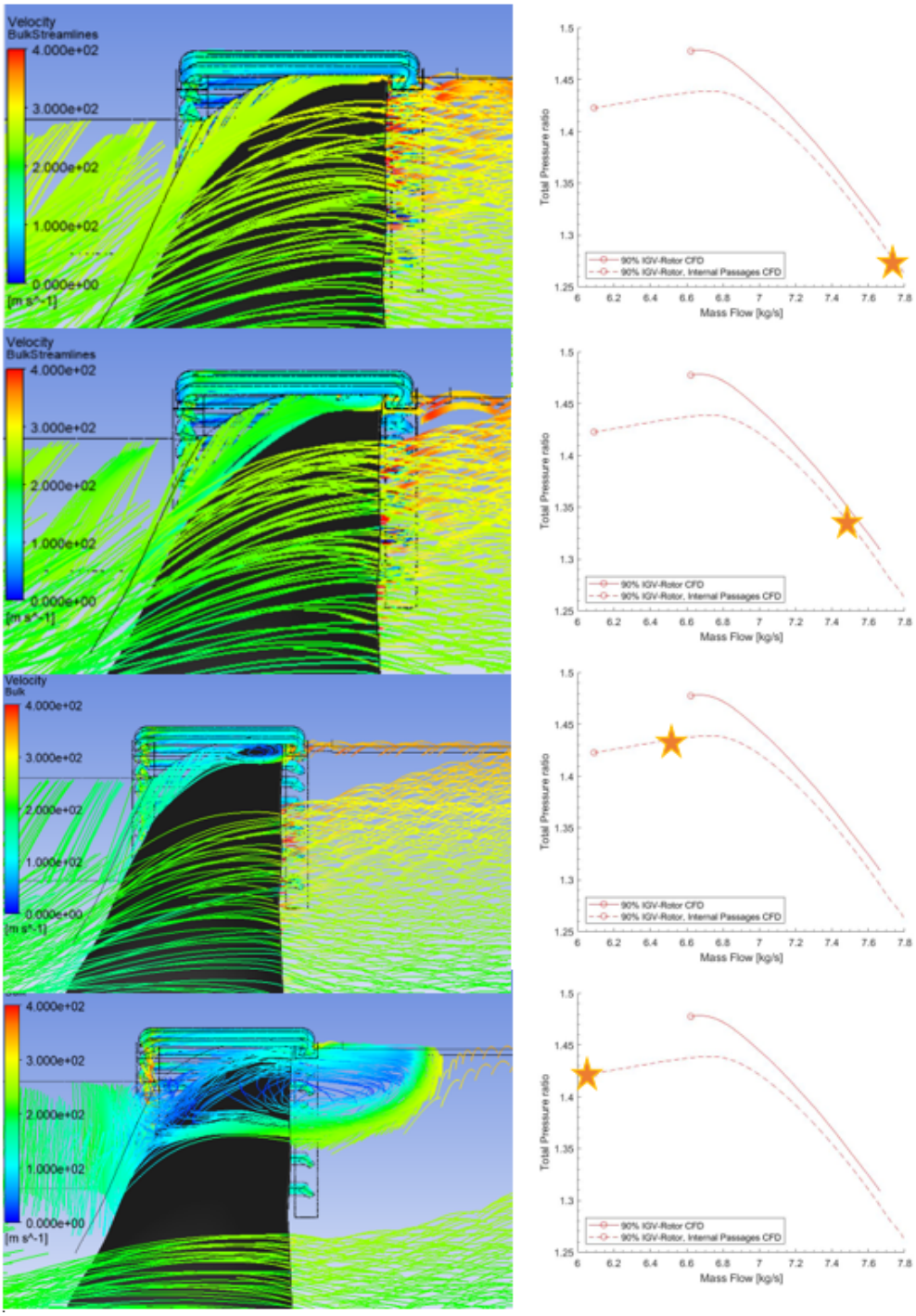


Figure 5.45. Flow development for the compressor with internal recirculation passages at 90% speed and 70% IGV schedule.

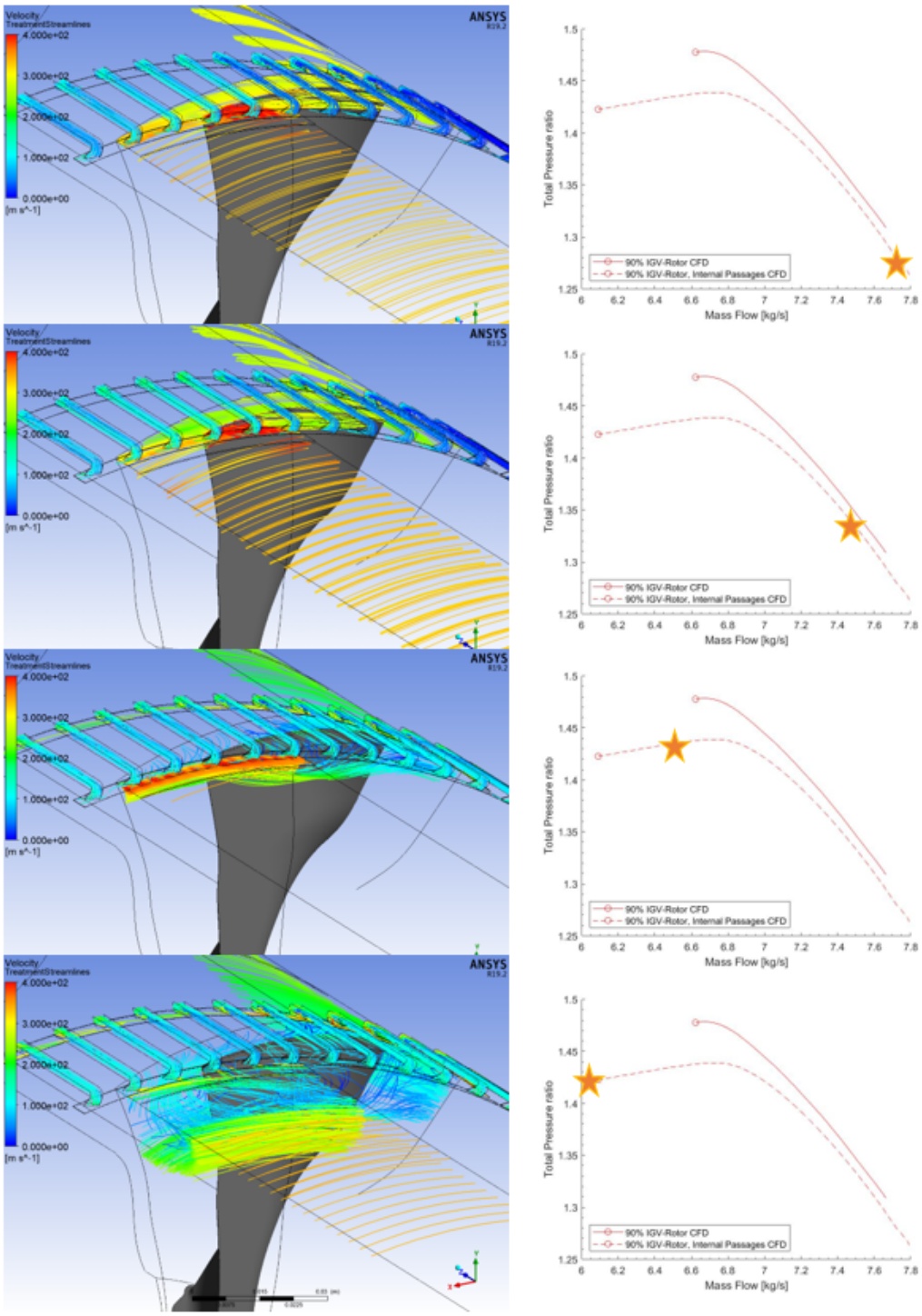


Figure 5.46. Flow development detailing passage operation for the compressor at 90% speed and 70% IGV schedule with internal passages installed.

5.3 Comparison

Both treatments showed various levels of success in the numerical simulation, but the internal passage shows much more promise. Ultimately, the s-shaped axial grooves are a subsonic treatment, and they worked as such and demonstrated stall margin losses in purely supersonic regions. Figure 5.47 presents the performance curves of all CFD cases examined, and Figure 5.48 presents the associated efficiency curves. Table 5.17 summarizes the stall margin predictions for each case.

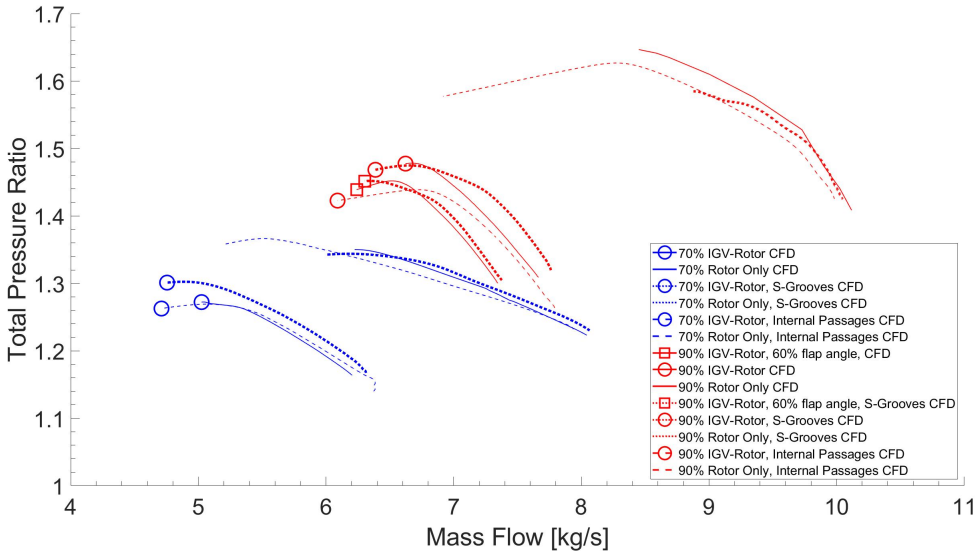


Figure 5.47. Comparison of numerical performance results.

Table 5.17. Summary of numeric stall margin predictions

Power	Casing	IGV	ΔSM [%]
70%	S-Groove	none	11.32
70%	IP	none	71.66
70%	S-Groove	70%	60.81
70%	IP	70%	79.34
90%	S-Groove	none	-34.67
90%	IP	none	82.61
90%	S-Groove	70%	65.98
90%	IP	70%	79.34

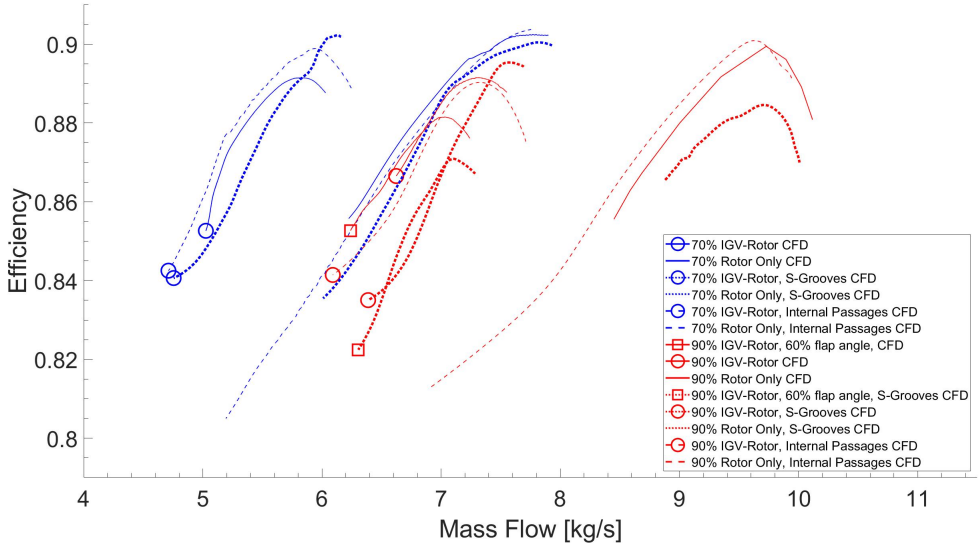


Figure 5.48. Comparison of numerical efficiency results.

Only the s-grooves were tested experimentally, and they were tested in the full IRS configuration. This does not allow a direct comparison to the CFD results, but does serve to validate trends. The numerical simulations demonstrated increased stall margin when whirl was applied, but losses when the compressor was allowed to operate with tip velocities greater than Mach = 1. Due to the highly unsteady nature of the s-groove operation, the CFX simulations were not able to predict the full extent of the stall margin increase. Both pressure ratio and efficiency trends followed experimental results. Total pressure ratios were higher for given mass flow rates and efficiency was reduced.

CHAPTER 6:
Conclusions and Recommendations

This study combined previous work on transonic compressor modeling and work on advanced compressor endwall treatments to create a frame work for evaluation of future designs. A multi-domain approach was conducted and the turbo-machinery tools built into ANSYS CFX were adapted to allow information transfer in the radial direction between the rotating and the stationary domain. A mesh sensitivity study was conducted to refine the mesh around the domain interface which resulted in an extremely fine hybrid mesh around the interface. The TCR model was set up to run in a rotor-only configuration, and, through careful use of inlet boundary conditions, the IGVs were modeled resulting in an IGV-rotor configuration. Finally, a pseudo-steady technique was evaluated and provided a more efficient means of driving the simulation through the power line up to stall.

Two different casing treatments were tested numerically — s-shaped axial grooves and self-recirculating internal passages. It was found the internal passages provide a much steadier performance allowing better CFD analysis and larger stall margin increases than the s-grooves. The internal passages were found to work even in the transonic cases, unlike the s-grooves. Performance of the s-grooves is unsteady, so CFD analysis was limited, but the simulations were able to prove they are only useful in subsonic scenarios.

Future work can improve on these results through more complete models of the TCR to include working models of the IGV and stator to allow direct comparison with the TCR. Rotor only simulations were used to validate those results, but no true validation was conducted for the IGV approximation. Fully transient simulations will be required to further expand on the evaluation of unsteady casing treatment designs. Finally, work should be done to decrease the computational expense of the domain interface between the gas passage and endwall treatment.

Experimental research was conducted in the half-stage, full-stage, and IRS configurations. The s-grooves were tested in the IRS configuration with the IGVs set at a variety of angles. It was found the s-grooves only worked when the IGVs were set to the scheduling for 70% speed. At this case stall margin increases of 117% were observed at 90% speed and an

increase of 286% was recorded at 70% speed. However, at normal scheduling the increases were not observed and at many point decreases were observed. This shows the s-grooves are only a subsonic casing treatment which aligns with CFD observations.

The internal passages tested numerically were not available for experimental testing. Future work should seek to refine the manufacturing techniques associated to allow the evaluate of this novel design as the CFD simulations show promise.

APPENDIX A:
Inlet Guide Vane Jigs

The IGVs have discrete settings for each power line tested; blade angle is based off of the protruding studs seen in Figure A.1 since the blades have a complex, varying angle. Previously, a machined aluminum plate was secured onto the blade ends and the blades were turned with a wrench until both blades aligned with the plate. Once roughly aligned, pins were run through an eye-hole in the blade stud which aligned with grooves in the plate. This kept the blades aligned while the locking nuts were tightened. This method worked, but it was a time-consuming method and required each blade angle to be set individually with a custom machined plate for each test point. As the angles needed for this experiment did not already have alignment plates made, a new jig was designed to allow rapid IGV blade angle setting.

The jig envisioned was a ring which would be inserted into the front of the IGV rig which would have slots for each of the blade leading edges and would be shaped such that the blades could only be rotated to the desired angle. Setting the blade angles with such a tool would be accomplished as follows. First, the jam nuts of all seventeen blades would be loosened to allow the blades to turn freely. Second, the blades would be turned to a greater angle then was being set (i.e. the set angle is 35° and the blades are turned to $\sim 50°$). Next, the ring would be placed onto the rig forcing the blades to open to the desired angle. After confirming the jig is snugly against the leading edges and hence confined in the proper location by its shape, each blade would be verified to be against the tool and then tightened. It is important to ensure the tool remains against the rig and each blade is tightened uniformly to keep the blade angle consistent and reduce error.

Additive manufacturing allows for the creating of unique shapes quickly which would otherwise be impossible or extremely complex to manufacture. An existing SolidWorks model which represents the IGV rig as designed was used. The SolidWorks model is designed such that a single mate controls the angle of each of the seventeen IGV blades (Figure A.1) based on the end bolt position. This allows the exact geometry and shape of the blades to be modeled for any discrete angle. It was necessary when modeling to save

the IGV assembly as a SolidWorks part file to allow the jig shaping methods to be applied. Saving it as a part file converted it to a multibody part which leaves the blades as bodies which can be manipulated to make the jig.

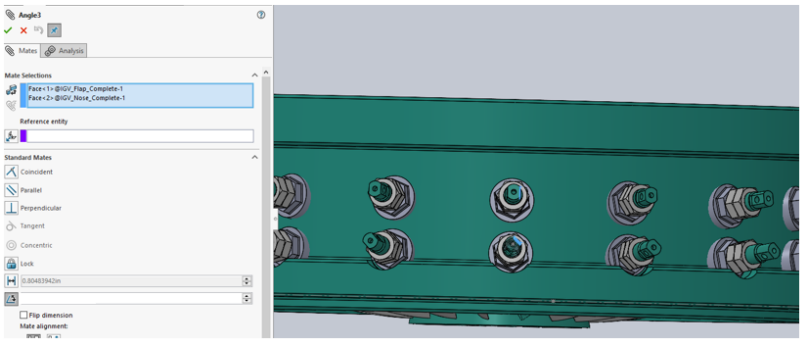


Figure A.1. Definition and setting of inlet guide vane flap angle with a side view of the IGV rig model.

A SolidWorks Boolean operator was used to design the unique shape of the blades. A solid ring was drawn such that it fit in approximately the middle of each blade. This ring was then extruded down into the blades as seen in Figure A.2. Using the Boolean subtraction tool, the ring was set as the body to be tooled and the IGV vanes were set as the tool as depicted in Figure A.3. A relief cut was required to allow the jig to easily slide on and off of the fixed forward part of the IGV. This cut was made on one blade then circularly patterned to each blade.

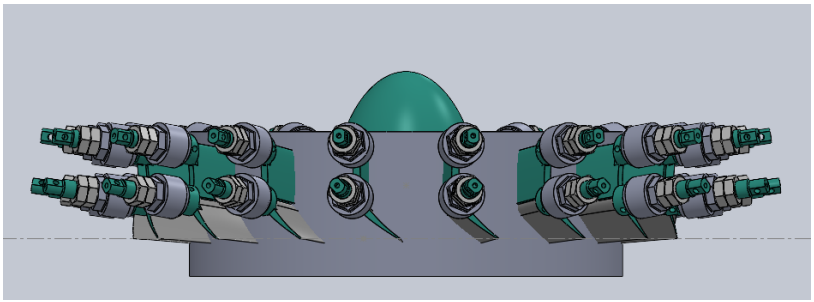


Figure A.2. The solid ring showing placement in the IGV with the endwall removed.

As built, the jig is a tolerance fit. Even with the heated volume available on the polycarbonate printer used, some thermal contraction was expected, so an adjustable tolerance was built into the jig model. The tightest fit possible was desired to properly set the blade

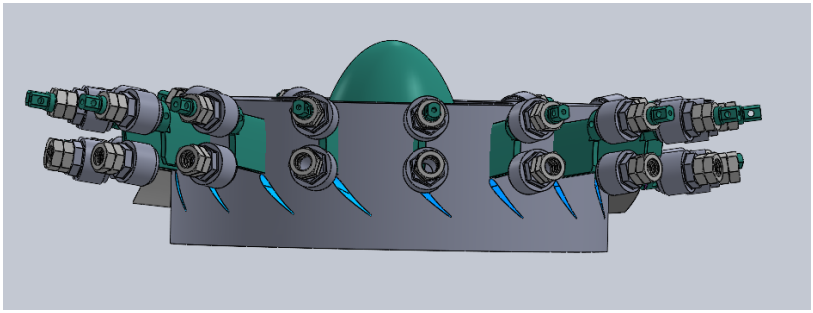


Figure A.3. The ring after the Boolean subtraction with blade cavities shown in blue.

angles; however, if the jig is too tight, it will not seat all the way down onto the IGVs altering the jig contact area and the blade set angle. Several test sections were printed in order to analyze the effect of the jig tolerance. The sections only spanned three of the seventeen blades ($\sim 60°$) and had tolerances of 0.000 in, 0.003 in, and 0.006 in respectively and are displayed in FigureA.4.

As expected, the tolerance fit (0.000") would not fully seat, the 0.003" tolerance had a complete but tight fit, and the 0.006" section fitted easily with little noticeable clearance. It was decided to make the complete ring using the 0.003" tolerance to allow more repeatable results. In order to assist in keeping the jig in place and make removing easier, a back plate was designed and printed to allow jacking bolts to be used for pushing and pulling. Figure A.5 shows the complete apparatus with the bolts protruding through the rig.

With the bolts in place, a nut and washer could be placed on both sides of the plate allowing the jig to be lowered and raised with a wrench; it was expected the full ring would be difficult to remove once fully seated. The plate could also be bolted to the rig via the through holes on the edge which line up with the IGV edge holes.

In practice, the full ring proved to be difficult to handle compared to the three blade section. Shop personnel preferred to use the test section vice the completed part. Additionally, the small section allows for quicker and cheaper production (the section took about 6 hrs to print versus the 30 hrs of the full rig). With the new strategy in place, sections for several other angles were manufactured. Rather than building the part from scratch each time as described previously, the “Surface-Extrude” command was used. This function allowed the



Figure A.4. The IGV test sections and a completed ring.

contact surface of the rig to be attached to the blade itself in the model, as shown in Figure A.6.

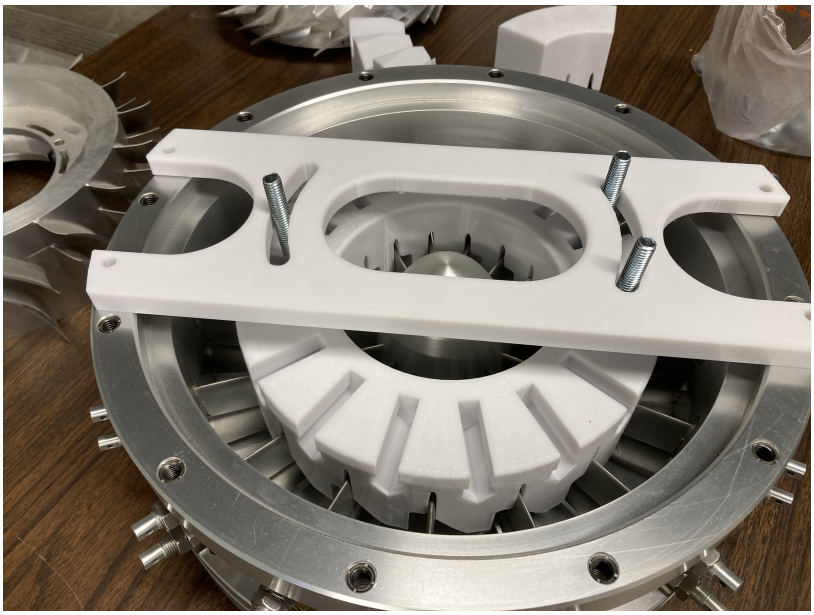


Figure A.5. The prototype IGV angle jig with the jacking bolts installed.

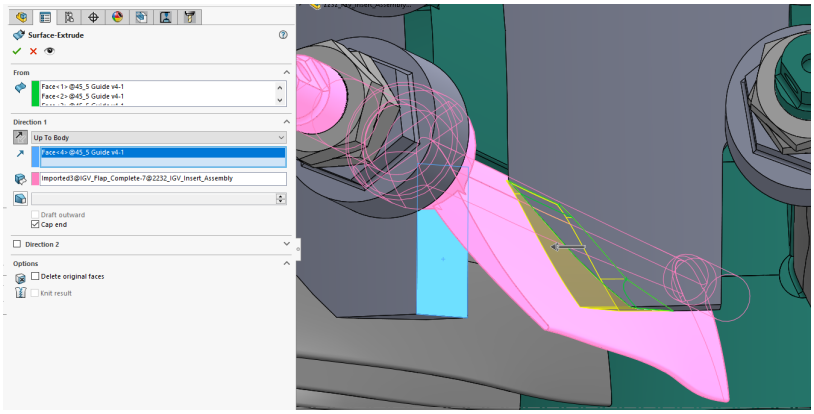


Figure A.6. Demonstration of the technique for automatic IGV jig generation.

Now, when the blade angle is changed in the assembly, the jig itself will conform to the new angle. Before each new jig was manufactured, the clearances and tolerances would be quickly adjusted to ensure a solid fit.

To validate these rigs, an uncertainty study was conducted on the blade angle and is presented in Section 2.2.1. It was found that operator consistency was key, so the full ring was revisited for future experiments. The new rings use a larger tolerance (0.006") and are significantly

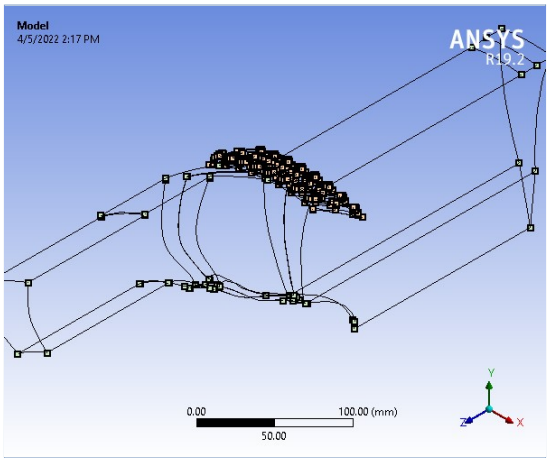
thinner providing less resistance when installed and removed from the IGV assembly. As the jig should still work even with an infinitely thin slice in contact with the blade, the new design should allow the tool to be installed and removed much easier. As such, no provision for a base plate or jacking screws was designed.

APPENDIX B:
Mesh Reports

B.1 S-Shaped Axial Grooves

Project

First Saved	Wednesday, October 27, 2021
Last Saved	Tuesday, March 29, 2022
Product Version	19.2 Release
Save Project Before Solution	No
Save Project After Solution	No



Contents

- Units
- Model (C3)
  - Geometry
    - Parts
  - Materials
  - Coordinate Systems
  - Connections
    - Contacts
      - Bonded - Gas_Path To Treatment_Domain
  - Mesh
    - Mesh Controls
  - Named Selections

Units

TABLE 1

Unit System	Metric (mm, kg, N, s, mV, mA) Degrees RPM Celsius
Angle	Degrees
Rotational Velocity	RPM
Temperature	Celsius

Model (C3)

Geometry

TABLE 2
Model (C3) > Geometry

Object Name	*Geometry*
State	Fully Defined
Definition	
Source	F:\M_Blake_Jones\S_Groove_files\dp1\CFX-3\DM\CFX-3.agdb
Type	DesignModeler
Length Unit	Meters
Bounding Box	
Length X	138.85 mm
Length Y	150.99 mm
Length Z	404.59 mm
Properties	
Volume	1.0692e+006 mm³
Scale Factor Value	1.
Statistics	
Bodies	2
Active Bodies	2
Nodes	11804465
Elements	28340490
Mesh Metric	Orthogonal Quality
Min	6.79227154520845E-08
Max	0.999909534922505
Average	0.745122592384659
Standard Deviation	0.148270095223723
Update Options	
Assign Default Material	No
Basic Geometry Options	
Parameters	Independent
Parameter Key	
Attributes	Yes
Attribute Key	
Named Selections	Yes
Named Selection Key	
Material Properties	Yes
Advanced Geometry Options	
Use Associativity	Yes
Coordinate Systems	Yes
Coordinate System Key	
Reader Mode Saves Updated File	No
Use Instances	Yes
Smart CAD Update	Yes
Compare Parts On Update	No
Analysis Type	3-D
Clean Bodies On Import	No
Stitch Surfaces On Import	No
Decompose Disjoint Geometry	Yes
Enclosure and Symmetry Processing	No

TABLE 3
Model (C3) > Geometry > Parts

Object Name	*GasPath_20TG_grooves_v1*	*20TG_S_Grooves_v2*
State	Meshed	
Graphics Properties		
Visible	Yes	
Transparency	1	
Definition		

Suppressed	No	
Coordinate System	Default Coordinate System	
Behavior	None	
Reference Frame	Lagrangian	
Material		
Assignment		
Fluid/Solid	Defined By Geometry (Solid)	
Bounding Box		
Length X	106.68 mm	115.26 mm
Length Y	144.48 mm	21.337 mm
Length Z	404.59 mm	22.86 mm
Properties		
Volume	1.064e+006 mm³	5167.5 mm³
Centroid X	-23.39 mm	-7.0448 mm
Centroid Y	98.638 mm	143.97 mm
Centroid Z	-28.571 mm	9.7969 mm
Statistics		
Nodes	11774746	29719
Elements	28219795	120695
Mesh Metric	Orthogonal Quality	
Min	7.82471021087972E-07	6.79227154520845E-08
Max	0.999909534922505	0.991427663023706
Average	0.745461919227719	0.66578431035852
Standard Deviation	0.14768933045487	0.236328278615978

Coordinate Systems

TABLE 4
Model (C3) > Coordinate Systems > Coordinate System

Object Name	*Global Coordinate System*	*Rotation Coordinate System*
State	Fully Defined	Suppressed
Definition		
Type	Cartesian	
Coordinate System ID	0.	
Coordinate System		Program Controlled
APDL Name		
Suppressed		Yes
Origin		
Origin X	0. mm	283.47 mm
Origin Y	0. mm	172.18 mm
Origin Z	0. mm	118.51 mm
Define By		Geometry Selection
Geometry		Defined
Directional Vectors		
X Axis Data	[1. 0. 0.]	
Y Axis Data	[0. 1. 0.]	[0. 0. 1.]
Z Axis Data	[0. 0. 1.]	[0. -1. 0.]
Principal Axis		
Axis		X
Define By		Global X Axis
Orientation About Principal Axis		
Axis		Y
Define By		Default
Transformations		
Base Configuration		Absolute
Transformed Configuration		[283.47 172.18 118.51]

Connections

TABLE 5
Model (C3) > Connections

Object Name	*Connections*
State	Fully Defined
Auto Detection	
Generate Automatic Connection On Refresh	Yes
Transparency	
Enabled	Yes

TABLE 6
Model (C3) > Connections > Contacts

Object Name	*Contacts*
State	Fully Defined
Definition	
Connection Type	Contact
Scope	
Scoping Method	Geometry Selection
Geometry	All Bodies
Auto Detection	
Tolerance Type	Slider
Tolerance Slider	0.
Tolerance Value	1.1341 mm
Use Range	No
Face/Face	Yes
Face Overlap Tolerance	Off
Cylindrical Faces	Include
Face/Edge	No
Edge/Edge	No
Priority	Include All

Group By	Bodies
Search Across	Bodies
Statistics	
Connections	1
Active Connections	1

TABLE 7
Model (C3) > Connections > Contacts > Contact Regions

Object Name	*Bonded - Gas_Path To Treatment_Domain*
State	Fully Defined
Scope	
Scoping Method	Named Selection
Contact	Gas_Path
Target	Treatment_Domain
Contact Bodies	GasPath_20TG_grooves_v1
Target Bodies	20TG_S_Grooves_v2
Protected	No
Advanced	
Small Sliding	Program Controlled

Mesh

TABLE 8
Model (C3) > Mesh

Object Name	*Mesh*
State	Solved
Display	
Display Style	Use Geometry Setting
Defaults	
Physics Preference	CFD
Solver Preference	CFX
Element Order	Linear
Element Size	4.0 mm
Sizing	
Use Adaptive Sizing	No
Growth Rate	Default (1.2)
Max Size	5.0 mm
Mesh Defeaturing	Yes
Defeature Size	3.e-002 mm
Capture Curvature	Yes
Curvature Min Size	Default (4.e-002 mm)
Curvature Normal Angle	Default (18.0°)
Capture Proximity	Yes
Proximity Min Size	3.e-002 mm
Num Cells Across Gap	5
Proximity Size Function Sources	Faces and Edges
Bounding Box Diagonal	453.62 mm
Average Surface Area	464.22 mm²
Minimum Edge Length	3.764e-004 mm
Quality	
Check Mesh Quality	Yes, Errors and Warnings
Target Skewness	Default (0.900000)
Smoothing	Medium
Mesh Metric	Orthogonal Quality
Min	6.7923e-008
Max	0.99991
Average	0.74512
Standard Deviation	0.14827
Inflation	
Use Automatic Inflation	None
Inflation Option	Smooth Transition
Transition Ratio	0.77
Maximum Layers	5
Growth Rate	1.2
Inflation Algorithm	Pre
View Advanced Options	No
Advanced	
Number of CPUs for Parallel Part Meshing	Program Controlled
Straight Sided Elements	
Rigid Body Behavior	Dimensionally Reduced
Triangle Surface Mesher	Program Controlled
Topology Checking	Yes
Pinch Tolerance	Default (2.7e-002 mm)
Generate Pinch on Refresh	No
Statistics	
Nodes	11804465
Elements	28340490

TABLE 9
Model (C3) > Mesh > Mesh Controls

Object Name	*Patch Conforming Method*	*Inflation*	*Match Control*	*Blade Faces*	*Blade Edges*	*Blade Base*	*Blade Base Outer*	*Blade Tip*	*Treatment Match*	*Treatment_Sizing*	*Lower Periodic*
State	Fully Defined										
Scope											
Scoping Method	Named Selection	Geometry Selection	Named Selection	Geometry Selection					Named Selection		Geometry Selection
Named Selection	Gas_Path									Treatment_Domain	

Geometry		1 Body		2 Faces	3 Faces	6 Faces	1 Face	4 Faces			2 Faces
High Boundary			Periodic_High						Treatment_Periodic_High		
Low Boundary			Periodic_Low						Treatment_Periodic_Low		
Definition											
Suppressed	No										
Method	Tetrahedrons										
Algorithm	Patch Conforming										
Element Order	Use Global Setting										
Boundary Scoping Method		Named Selections									
Boundary		Multiple Entities									
Inflation Option		First Layer Thickness									
First Layer Height		1.e-003 mm									
Maximum Layers		23									
Growth Rate		1.2									
Inflation Algorithm		Pre									
Transformation			Cyclic						Cyclic		
Axis of Rotation			Global Coordinate System						Global Coordinate System		
Control Messages			No						No		
Type				Element Size						Element Size	
Element Size				0.5 mm	5.e-002 mm	0.25 mm	0.1 mm	1.e-002 mm		0.8 mm	4.0 mm
Advanced											
Defeature Size				1.e-006 mm						Default (3.e-002 mm)	
Behavior				Soft						Soft	
Growth Rate				Default (1.2)						Default (1.2)	
Capture Curvature				No						No	
Capture Proximity				No						No	

TABLE 10
Model (C3) > Mesh > Mesh Controls

Object Name	*Treatment Interface*
State	Fully Defined
Scope	
Scoping Method	Named Selection
Named Selection	Treatment_Interface
Definition	
Suppressed	No
Type	Element Size
Element Size	0.5 mm
Advanced	
Defeature Size	1.e-002 mm
Behavior	Soft
Growth Rate	1.2
Capture Curvature	No
Capture Proximity	No

Named Selections

TABLE 11
Model (C3) > Named Selections > Named Selections

Object Name	*Inlet*	*Outlet*	*Periodic_Low*	*Periodic_High*	*OuterWall*	*InnerWall*	*Blisk_minus_Blade*	*Blade*	*Treatment_Bottom*	*Treatment_Periodic_Low*	*Treatment_Periodic_High*
State	Fully Defined										
Scope											
Scoping Method	Geometry Selection										
Geometry	1 Face		4 Faces		8 Faces	7 Faces	5 Faces	15 Faces	3 Faces	1 Face	
Definition											
Send to Solver	Yes										
Protected	Program Controlled										
Visible	No						Yes				
Program Controlled Inflation	Exclude										
Statistics											
Type	Manual										
Total Selection	1 Face		4 Faces		8 Faces	7 Faces	5 Faces	15 Faces	3 Faces	1 Face	
Surface Area	3265.5 mm²	1835.3 mm²	42632 mm²		17320 mm²	4340.4 mm²	864.73 mm²	11727 mm²	2191.8 mm²	4.2877 mm²	3.9106 mm²
Suppressed	0										
Used by Mesh Worksheet	No										

TABLE 12
Model (C3) > Named Selections > Named Selections

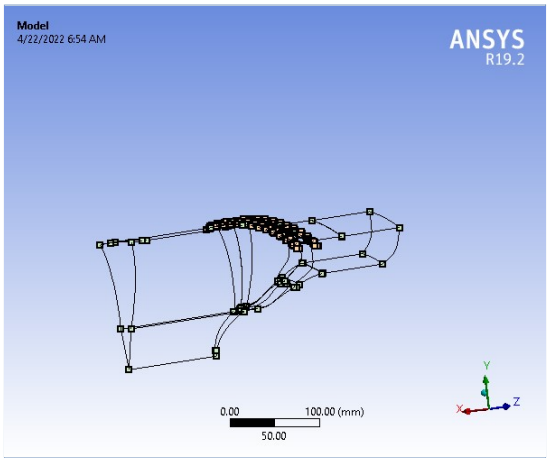
Object Name	*Treatment_Wall*	*Treatment_Interface*	*Treatment_Domain*	*Gas_Path*
State	Fully Defined			
Scope				
Scoping Method	Geometry Selection			
Geometry	233 Faces	3 Faces	1 Body	
Definition				

Send to Solver	Yes		
Protected	Program Controlled		
Visible	Yes	No	Yes
Program Controlled Inflation	Exclude		
Statistics			
Type	Manual		
Total Selection	233 Faces	3 Faces	1 Body
Surface Area	4908.9 mm²	1041.1 mm²	
Suppressed	0		
Used by Mesh Worksheet	No		

B.2 Internal Passages

Project

First Saved	Monday, March 28, 2022
Last Saved	Wednesday, April 20, 2022
Product Version	19.2 Release
Save Project Before Solution	No
Save Project After Solution	No



Contents

- Units
- Model (C3)
  - Geometry
    - Parts
  - Materials
  - Coordinate Systems
  - Connections
    - Contacts
      - Contact Region
  - Mesh
    - Mesh Controls
  - Named Selections

Units

TABLE 1

Unit System	Metric (mm, kg, N, s, mV, mA) Degrees RPM Celsius
Angle	Degrees
Rotational Velocity	RPM
Temperature	Celsius

Model (C3)

Geometry

TABLE 2
Model (C3) > Geometry

Object Name	*Geometry*
State	Fully Defined
Definition	
Source	F:\M_Blake_Jones\Recirculating_Treatment_files\dp0\CFX\DM\CFX.agdb
Type	DesignModeler
Length Unit	Meters
Bounding Box	
Length X	124.39 mm
Length Y	146.68 mm
Length Z	404.59 mm
Properties	
Volume	1.0631e+006 mm³
Scale Factor Value	1.
Statistics	
Bodies	2
Active Bodies	2
Nodes	10167000
Elements	34482633
Mesh Metric	None
Update Options	
Assign Default Material	No
Basic Geometry Options	
Parameters	Independent
Parameter Key	
Attributes	Yes
Attribute Key	
Named Selections	Yes
Named Selection Key	
Material Properties	Yes
Advanced Geometry Options	
Use Associativity	Yes
Coordinate Systems	Yes
Coordinate System Key	
Reader Mode Saves Updated File	No
Use Instances	Yes
Smart CAD Update	Yes
Compare Parts On Update	No
Analysis Type	3-D
Clean Bodies On Import	No
Stitch Surfaces On Import	No
Decompose Disjoint Geometry	Yes
Enclosure and Symmetry Processing	No

TABLE 3
Model (C3) > Geometry > Parts

Object Name	*ColdBlade_15TG_slot_v3*	*Internal_Passage_Domain_v4*
State	Meshed	
Graphics Properties		
Visible	Yes	
Transparency	1	
Definition		
Suppressed	No	
Coordinate System	Default Coordinate System	
Behavior	None	
Reference Frame	Lagrangian	

Material		
Assignment		
Fluid/Solid	Defined By Geometry (Solid)	
Bounding Box		
Length X	106.2 mm	124.39 mm
Length Y	143.89 mm	37.958 mm
Length Z	404.59 mm	39.078 mm
Properties		
Volume	1.0611e+006 mm³	1959.6 mm³
Centroid X	-23.315 mm	-34.446 mm
Centroid Y	98.528 mm	136.29 mm
Centroid Z	-28.698 mm	21.068 mm
Statistics		
Nodes	6445181	3721819
Elements	17084453	17398180
Mesh Metric	None	

Coordinate Systems

TABLE 4
Model (C3) > Coordinate Systems > Coordinate System

Object Name	*Global Coordinate System*
State	Fully Defined
Definition	
Type	Cartesian
Coordinate System ID	0.
Origin	
Origin X	0. mm
Origin Y	0. mm
Origin Z	0. mm
Directional Vectors	
X Axis Data	[1. 0. 0.]
Y Axis Data	[0. 1. 0.]
Z Axis Data	[0. 0. 1.]

Connections

TABLE 5
Model (C3) > Connections

Object Name	*Connections*
State	Fully Defined
Auto Detection	
Generate Automatic Connection On Refresh	Yes
Transparency	
Enabled	Yes

TABLE 6
Model (C3) > Connections > Contacts

Object Name	*Contacts*
State	Fully Defined
Definition	
Connection Type	Contact
Scope	
Scoping Method	Geometry Selection
Geometry	All Bodies
Auto Detection	
Tolerance Type	Slider
Tolerance Slider	0.
Tolerance Value	1.1199 mm
Use Range	No
Face/Face	Yes
Face Overlap Tolerance	Off
Cylindrical Faces	Include
Face/Edge	No
Edge/Edge	No
Priority	Include All
Group By	Bodies
Search Across	Bodies
Statistics	
Connections	1
Active Connections	1

TABLE 7
Model (C3) > Connections > Contacts > Contact Regions

Object Name	*Contact Region*
State	Fully Defined
Scope	
Scoping Method	Geometry Selection
Contact	10 Faces
Target	7 Faces
Contact Bodies	ColdBlade_15TG_slot_v3
Target Bodies	Internal_Passage_Domain_v4
Protected	No
Advanced	
Small Sliding	Program Controlled

Mesh

TABLE 8
Model (C3) > Mesh

Object Name	*Mesh*
State	Solved
Display	
Display Style	Use Geometry Setting
Defaults	
Physics Preference	CFD
Solver Preference	CFX
Element Order	Linear
Element Size	3.0 mm
Sizing	
Use Adaptive Sizing	No
Growth Rate	Default (1.2)
Max Size	Default (6.0 mm)
Mesh Defeaturing	Yes
Defeature Size	Default (1.5e-002 mm)
Capture Curvature	Yes
Curvature Min Size	Default (3.e-002 mm)
Curvature Normal Angle	Default (18.0°)
Capture Proximity	Yes
Proximity Min Size	Default (3.e-002 mm)
Num Cells Across Gap	5
Proximity Size Function Sources	Faces and Edges
Bounding Box Diagonal	447.98 mm
Average Surface Area	485.3 mm²
Minimum Edge Length	3.764e-004 mm
Quality	
Check Mesh Quality	Yes, Errors
Target Skewness	Default (0.900000)
Smoothing	Medium
Mesh Metric	None
Inflation	
Use Automatic Inflation	None
Inflation Option	Smooth Transition
Transition Ratio	0.77
Maximum Layers	5
Growth Rate	1.2
Inflation Algorithm	Pre
View Advanced Options	No
Advanced	
Number of CPUs for Parallel Part Meshing	Program Controlled
Straight Sided Elements	
Rigid Body Behavior	Dimensionally Reduced
Triangle Surface Mesher	Program Controlled
Topology Checking	Yes
Pinch Tolerance	Default (2.7e-002 mm)
Generate Pinch on Refresh	No
Statistics	
Nodes	10167000
Elements	34482633

TABLE 9
Model (C3) > Mesh > Mesh Controls

Object Name	*Blade Tip*	*Blade Faces*	*Blade Tip 2*	*Patch Conforming Method*	*Gas_Passage_Periodic*	*Treatment_Forward_Periodic*	*Match Control*	*Treatment Interface Forward*	*Blade Base*	*Bl Ba Ou*
State	Fully Defined									
Scope										
Scoping Method	Geometry Selection		Named Selection						Geomet Selectio	
Geometry	3 Faces	2 Faces							6 Faces	Fa
Named Selection			Blade Tip 2	Gas_Passage				Treatment_Interface_Forward		
High Boundary					Periodic_High	Treatment_Periodic_High_Forward	Treatment_Periodic_High_Aft			
Low Boundary					Periodic_Low	Treatment_Periodic_Low_Forward	Treatment_Periodic_Low_Aft			
Definition										
Suppressed	No									
Type	Element Size							Element Size		
Element Size	0.1 mm	0.5 mm	5.e-002 mm					0.25 mm		
Method				Tetrahedrons						
Algorithm				Patch Conforming						
Element Order				Use Global Setting						
Transformation					Cyclic					
Axis of Rotation					Global Coordinate System					
Control Messages					No					
Advanced										
Defeature Size	Default (1.5e-002 mm)							Default (1.5e-002		
Behavior	Soft							Soft		
Growth Rate	Default (1.2)							Default (1.2)		
Capture Curvature	No							No		

Capture Proximity	No		No

TABLE 10
Model (C3) > Mesh > Mesh Controls

Object Name	*Treatment Interface Aft*	*TreatmentBottomForward*	*Inflation*
State	Fully Defined		
Scope			
Scoping Method	Named Selection		Geometry Selection
Named Selection	Treatment_Interface_Aft	Treatment_Bottom_Forward	
Geometry			1 Body
Definition			
Suppressed	No		
Type	Element Size		
Element Size	0.25 mm		
Boundary Scoping Method			Named Selections
Boundary			Multiple Entities
Inflation Option			First Layer Thickness
First Layer Height			1.e-003 mm
Maximum Layers			23
Growth Rate			1.2
Inflation Algorithm			Pre
Advanced			
Defeature Size	Default (1.5e-002 mm)		
Behavior	Soft		
Growth Rate	Default (1.2)		
Capture Curvature	No		
Capture Proximity	No		

Named Selections

TABLE 11
Model (C3) > Named Selections > Named Selections

Object Name	*Treatment*	*Gas_Passage*	*Outlet*	*Periodic_High*	*Inlet*	*Periodic_Low*	*Inner_Wall*	*Blisk_minus_Blade*	*Treatment_Interface_Forward*	*Treatment_Interface_Aft*	*Outer_W*
State	Fully Defined										
Scope											
Scoping Method	Geometry Selection										
Geometry	1 Body		1 Face	4 Faces	1 Face	4 Faces	7 Faces	5 Faces	3 Faces		9 Face
Definition											
Send to Solver	Yes										
Protected	Program Controlled										
Visible	Yes		No					Yes	No		
Program Controlled Inflation	Exclude										
Statistics											
Type	Manual										
Total Selection	1 Body		1 Face	4 Faces	1 Face	4 Faces	7 Faces	5 Faces	3 Faces		9 Face
Suppressed	0										
Used by Mesh Worksheet	No										
Surface Area			1835.3 mm²	42538 mm²	3238.9 mm²	42538 mm²	4340.4 mm²	864.74 mm²	233.93 mm²	234.04 mm²	17818 m

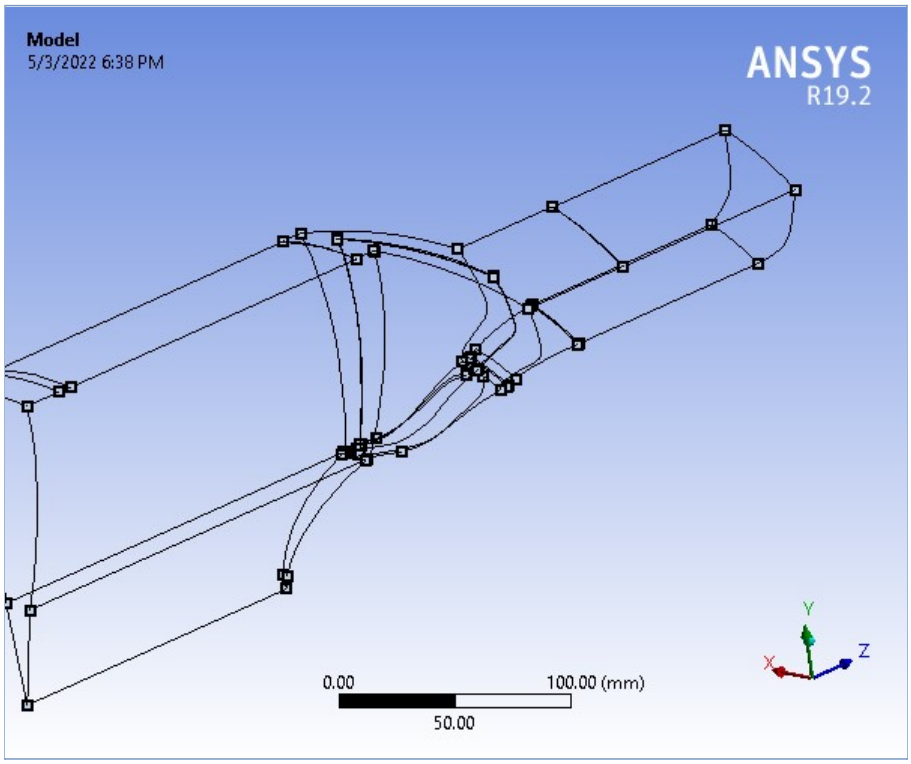
TABLE 12
Model (C3) > Named Selections > Named Selections

Object Name	*Blade*	*Treatment_Bottom_Forward*	*Treatment_Periodic_Low_Forward*	*Treatment_Periodic_Low_Aft*	*Treatment_Periodic_High_Forward*	*Treatment_Periodic_High_Aft*	*Tr*
State	Fully Defined						
Scope							
Scoping Method	Geometry Selection						
Geometry	15 Faces	3 Faces	1 Face				
Definition							
Send to Solver	Yes						
Protected	Program Controlled						
Visible	Yes	No					
Program Controlled Inflation	Exclude						
Statistics							
Type	Manual						
Total Selection	15 Faces	3 Faces	1 Face				
Surface Area	11727 mm²	689.31 mm²	0.62902 mm²		0.629 mm²		
Suppressed	0						
Used by Mesh Worksheet	No						

B.3 Refined Standard Passage

Project

First Saved	Thursday, November 19, 2020
Last Saved	Monday, April 25, 2022
Product Version	19.2 Release
Save Project Before Solution	No
Save Project After Solution	No



Contents

- Units
- Model (A3)
  - Geometry
    - Part 1
  - Materials
  - Coordinate Systems
  - Connections
    - Contacts
  - Mesh
    - Mesh Controls
  - Named Selections

Units

TABLE 1

Unit System	Metric (mm, kg, N, s, mV, mA) Degrees RPM Celsius
Angle	Degrees
Rotational Velocity	RPM
Temperature	Celsius

Model (A3)

Geometry

TABLE 2
Model (A3) > Geometry

Object Name	*Geometry*
State	Fully Defined
Definition	
Source	F:\M_Blake_Jones\Solid Works\Ben's Models\1Blade_ColdShape_15TTG.x_t
Type	Parasolid
Length Unit	Meters
Bounding Box	
Length X	106.2 mm
Length Y	143.89 mm
Length Z	404.59 mm
Properties	
Volume	1.0615e+006 mm³
Scale Factor Value	1.
Statistics	
Bodies	1
Active Bodies	1
Nodes	13857291
Elements	33370058
Mesh Metric	Orthogonal Quality
Min	5.62235112610554E-04

Max	0.999926055255414
Average	0.742378567746195
Standard Deviation	0.154184697915113
Update Options	
Assign Default Material	No
Basic Geometry Options	
Solid Bodies	Yes
Surface Bodies	Yes
Line Bodies	No
Parameters	Independent
Parameter Key	ANS;DS
Attributes	No
Named Selections	No
Material Properties	No
Advanced Geometry Options	
Use Associativity	Yes
Coordinate Systems	No
Reader Mode Saves Updated File	No
Use Instances	Yes
Smart CAD Update	Yes
Compare Parts On Update	No
Analysis Type	3-D
Mixed Import Resolution	None
Clean Bodies On Import	No
Stitch Surfaces On Import	No
Decompose Disjoint Geometry	Yes
Enclosure and Symmetry Processing	No

TABLE 3
Model (A3) > Geometry > Parts

Object Name	*Part 1*
State	Meshed
Graphics Properties	
Visible	Yes
Transparency	1
Definition	
Suppressed	No
Coordinate System	Default Coordinate System
Behavior	None
Reference Frame	Lagrangian
Material	
Assignment	
Fluid/Solid	Defined By Geometry (Solid)
Bounding Box	
Length X	106.2 mm
Length Y	143.89 mm
Length Z	404.59 mm
Properties	
Volume	1.0615e+006 mm³
Centroid X	-23.303 mm
Centroid Y	98.536 mm
Centroid Z	-28.465 mm

Statistics	
Nodes	13857291
Elements	33370058
Mesh Metric	Orthogonal Quality
Min	5.62235112610554E-04
Max	0.999926055255414
Average	0.742378567746195
Standard Deviation	0.154184697915113

Coordinate Systems

TABLE 4
Model (A3) > Coordinate Systems > Coordinate System

Object Name	*Global Coordinate System*
State	Fully Defined
Definition	
Type	Cartesian
Coordinate System ID	0.
Origin	
Origin X	0. mm
Origin Y	0. mm
Origin Z	0. mm
Directional Vectors	
X Axis Data	[1. 0. 0.]
Y Axis Data	[0. 1. 0.]
Z Axis Data	[0. 0. 1.]

Connections

TABLE 5
Model (A3) > Connections

Object Name	*Connections*
State	Fully Defined
Auto Detection	
Generate Automatic Connection On Refresh	Yes
Transparency	
Enabled	Yes

TABLE 6
Model (A3) > Connections > Contacts

Object Name	*Contacts*
State	Fully Defined
Definition	
Connection Type	Contact
Scope	
Scoping Method	Geometry Selection
Geometry	All Bodies
Auto Detection	
Tolerance Type	Slider
Tolerance Slider	0.
Tolerance Value	1.1059 mm
Use Range	No

Face/Face	Yes
Face Overlap Tolerance	Off
Cylindrical Faces	Include
Face/Edge	No
Edge/Edge	No
Priority	Include All
Group By	Bodies
Search Across	Bodies
Statistics	
Connections	0
Active Connections	0

Mesh

TABLE 7
Model (A3) > Mesh

Object Name	*Mesh*
State	Solved
Display	
Display Style	Use Geometry Setting
Defaults	
Physics Preference	CFD
Solver Preference	CFX
Element Order	Linear
Element Size	0.8 mm
Sizing	
Use Adaptive Sizing	No
Growth Rate	Default (1.2)
Max Size	5.0 mm
Mesh Defeaturing	Yes
Defeature Size	1.e-006 mm
Capture Curvature	No
Capture Proximity	No
Bounding Box Diagonal	442.35 mm
Average Surface Area	2849.6 mm²
Minimum Edge Length	3.764e-004 mm
Quality	
Check Mesh Quality	Yes, Errors and Warnings
Target Skewness	0.9
Smoothing	High
Mesh Metric	Orthogonal Quality
Min	5.6224e-004
Max	0.99993
Average	0.74238
Standard Deviation	0.15418
Inflation	
Use Automatic Inflation	None
Inflation Option	First Layer Thickness
First Layer Height	1.125e-004 mm
Maximum Layers	53
Growth Rate	1.2
Inflation Algorithm	Pre

View Advanced Options	No
Advanced	
Number of CPUs for Parallel Part Meshing	8
Straight Sided Elements	
Rigid Body Behavior	Dimensionally Reduced
Triangle Surface Mesher	Program Controlled
Topology Checking	Yes
Pinch Tolerance	Default (7.2e-003 mm)
Generate Pinch on Refresh	No
Statistics	
Nodes	13857291
Elements	33370058

TABLE 8
Model (A3) > Mesh > Mesh Controls

Object Name	*Patch Conforming Method*	*Inflation*	*Face Sizing 2*	*Face Sizing*	*Match Control*	*Face Sizing 3*	*Face Sizing 4*	*Face Sizing 5*
State	Fully Defined							
Scope								
Scoping Method	Geometry Selection							
Geometry	1 Body		2 Faces	3 Faces		6 Faces	1 Face	4 Faces
High Geometry Selection					4 Faces			
Low Geometry Selection					4 Faces			
Definition								
Suppressed	No							
Method	Tetrahedrons							
Algorithm	Patch Conforming							
Element Order	Use Global Setting							
Boundary Scoping Method		Geometry Selection						
Boundary		23 Faces						
Inflation Option		First Layer Thickness						
First Layer Height		1.e-003 mm						
Maximum Layers		23						
Growth Rate		1.4						
Inflation Algorithm		Pre						
Type			Element Size			Element Size		
Element Size			0.36 mm	4.e-002 mm		0.18 mm	8.e-002 mm	1.e-002 mm
Transformation					Cyclic			
Axis of Rotation					Global Coordinate System			
Control Messages					No			
Advanced								

Defeature Size		Default (1.e-006 mm)	1.e-006 mm		Default (1.e-006 mm)
Behavior		Soft			Soft
Growth Rate		Default (1.2)			Default (1.2)
Capture Curvature		No			No
Capture Proximity		No			No

Named Selections

TABLE 9
Model (A3) > Named Selections > Named Selections

Object Name	*Inlet*	*Outlet*	*Periodic_Low*	*Periodic_high*	*OuterWall*	*InnerWall*	*Blisk_minus_Blade*	*Blade*
State	Fully Defined							
Scope								
Scoping Method	Geometry Selection							
Geometry	1 Face		4 Faces		7 Faces	6 Faces	5 Faces	11 Faces
Definition								
Send to Solver	Yes							
Protected	Program Controlled							
Visible	Yes							
Program Controlled Inflation	Exclude							
Statistics								
Type	Manual							
Total Selection	1 Face		4 Faces		7 Faces	6 Faces	5 Faces	11 Faces
Surface Area	3238.9 mm²	1835.3 mm²	42541 mm²	42546 mm²	18281 mm²	4322. mm²	867.46 mm²	11719 mm²
Suppressed	0							
Used by Mesh Worksheet	No							

THIS PAGE INTENTIONALLY LEFT BLANK

APPENDIX C:
CFX on NPS Hamming HPC

Hamming is NPS's in-house super computer. It is able to run ANSYS across a large number of processors in parallel, greatly reducing the physical computation time. Nodes on Hamming have either 32 or 64 processors. If a simulation can be reasonably run with less than 64 processors, much computational overhead can be reduced by keeping the simulation on a single node. Otherwise resources (time) will be spent communicating between nodes rather than performing the computational analysis of the model. Below are details of operating CFX on Hamming.

To access and use the resources on Hamming, an account must be made and registered. The gouge sheet [14] details registering for a Hamming account and provides links for the Hamming overview page and the necessary programs. Running CFX on Hamming only requires the use of MobaXTERM. Once an account and password has been set for Hamming, open the MobaXTERM application while on the NPS network or VPN. On the upper left side of the window, click on "sessions." Start a new session and select "SSH" on the following prompt. When prompted for the host name, enter " USERNAME@hamming-sub1.uc.nps.edu" (ex: matthew.jones@hamming-sub1.uc.nps.edu) and press enter. A new session should launch in MobaXTERM and request the password for the associated account. Your password will not appear on the screen as you type.

Once a session is begun on Hamming, the CFX.def file for the project and a batch.sh file will need to be in the working directory (an example batch file is included and explained below). For running and storing data, make sure to be in the /data/username directory. Navigate to the directory in the file explorer to easily see what files are present and use the command "cd /data/username" to navigate the command window to the same directory. With the definition file and the batch file both in the same working directory, use the command "sbatch mybatchfile.sh" to start the CFX run. Once the run begins, the command "squeue -u username" can be used to see if the job is running and how long it has been running. As the model runs in batch mode, an out file (myfile.out) will be continually updated with the normal residual output of the CFX solver manager. This can be used to check the iteration

count and ensure residuals are at the expected level. After the simulation completes, the results and any intermediate back up files can be downloaded and processed in CFX post on the local machine.

Depicted below is an example batch execution file. The file requests 96 GB of memory to perform the calculation on 1 node with 64 processors. The output file name and job name are specified along with the user name. A physical wall time limit is specified at 155 hrs. After querying the host name, ANSYS is loaded and a list of host names is generated. For solving, the definition file is specified, the number of parallel processes and the parallel method is defined. Finally, the list of host names is specified for the parallel operation. More details about the script can be found in the guide by [15].

```
#!/bin/bash
#SBATCH --ntasks=1
#SBATCH --mem=96G
#SBATCH --nodes 1
#SBATCH --ntasks-per-node=1
#SBATCH --cpus-per-task=64
#SBATCH --output=MYFILE.out
#SBATCH --job-name=MYJOB
#SBATCH --mail-user=USERNAME
#SBATCH --mail-type=END
#SBATCH --time=155:00:00

echo " "
echo "hostname = 'hostname'"
echo "JOB_ID = $SLURM_JOBID"
echo " "
echo "--------------------"
echo "--------------------"
echo " "

. /etc/profile
module load app/ansys
export CFX5RSH=ssh

MYHOSTLIST=$(srun hostname | sort | \
                uniq -c | \
                awk '{print $2 "*" $1}' | \
                paste -sd, -)

echo $MYHOSTLIST

unset SLURM_GTIDS

cfx5solve -def MYFILE.def \
                -parallel \
                -start-method "Intel MPI Distributed Parallel" \
                -par-dist "$MYHOSTLIST" \
```

THIS PAGE INTENTIONALLY LEFT BLANK

List of References

[1] J. Green, "A manufacturing process to implement transonic compressor endwall treatments," Master's thesis, Department of Mechanical and Aerospace Engineering, Naval Postgraduate School, Monterey, CA, 2021.

[2] M. Hathaway, "Passive endwall treatments for enhancing stability," NASA, Tech. Rep., 2007.

[3] J. McNab, "Experimental testing and cfd modeling of an advanced transonic compressor for military applications," Master's thesis, Department of Mechanical and Aerospace Engineering, Naval Postgraduate School, Monterey, CA, 2011.

[4] H. Chen, S. Koley, Y. Li, and J. Katz, "Systematic experimental evaluations aimed at optimizing the geometry of axial caisng grooves in a compressor," *Journal of Turbomachinery*, vol. 141, 2019.

[5] M. Hembera, H. Kau, and E. Johann, "Simulation of casing treatments of a transonic compressor stage," *Journal of Turbomachinery*, vol. 139, 2017.

[6] G. Zhu and B. Yang, "Optimization of slots-groove coupled casing treatment for an axial transonic compressor," *Journal of Turbomachinery*, vol. 142, 2020.

[7] M. Rolfes, M. Lange, K. Vogeler, and R. Mailach, "Experimental and numerical investigation of a circumferential groove casing treatment in a low-speed axial research compressor at different tip clearances," *Journal of Turbomachinery*, vol. 139, 2017.

[8] S. Kumar, D. Bhanudasji Alone, S. Thimmaiah, L. Mudipalli, J. Kumar, R. Ganguli, S. Kandagal, and S. Jana, "Aerodynamic behavior of a transoic axial flw compressor stage with self-recirculating casing treatment," *Aerospace Science and Technology*, vol. 112, 2021.

[9] A. Grosvenor, G. Rixon, L. Sailer, M. Matheson, D. Gutzwiller, A. Demeulenaere, M. Gontier, and A. Strazisar, "High resolution rans nonlinear harmonic study of stage 67 tip injection physics," *Journal of Turbomachinery*, vol. 137, 2015.

[10] A. Londono, "Near-stall modal disturbances within a transonic compressor rotor," Master's thesis, Department of Mechanical and Aerospace Engineering, Naval Postgraduate School, Monterey, CA, 2011.

[11] B. Meinster, "Stall characteristic prediction in a single passage of a transonic axial compressor rotor," Master's thesis, Department of Mechanical and Aerospace Engineering, Naval Postgraduate School, Monterey, CA, 2021.

[12] DeSousa, "Development of advanced casing treatments for transonic compressors," Master's thesis, Department of Mechanical and Aerospace Engineering, Naval Postgraduate School, Monterey, CA, 2018.

[13] G. Descovich, "Experimental and computational investigation of steam-induced stall in a transonic compressor rotor for a military fan," Master's thesis, Department of Mechanical and Aerospace Engineering, Naval Postgraduate School, Monterey, CA, 2011.

[14] A. Thoeny, "Hamming gouge," 2020, https://nps01.sharepoint.com/:w:/s/RocketPropulsionLab-Students/ERXoW7ezKrpEuV6Vu4Ng-lgBlC6TbbXnV2nqOtPaP6Wt4g?e=Fu2bdP.

[15] *How To run ANSYS CFX on an HPC-Cluster*, HKHLR, 2018, https://www.hkhlr.de/sites/default/files/field$_download_file/HowTo-ANSYS_CFX.pdf$.

Initial Distribution List

1. Defense Technical Information Center
   Ft. Belvoir, Virginia

2. Dudley Knox Library
   Naval Postgraduate School
   Monterey, California